

# Is $G$ a Conversion Factor or a Fundamental Unit?<sup>¶</sup>

G. Fiorentini<sup>1</sup>, L. B. Okun<sup>2</sup>, and M. Vysotskii<sup>2</sup>

<sup>1</sup> INFN, Sezione di Ferrara, Ferrara, Italy

e-mail: fiorentini@fe.infn.it

<sup>2</sup> Institute of Theoretical and Experimental Physics, Moscow, 117218 Russia

e-mail: okun@heron.itep.ru; vysotsky@heron.itep.ru

Received September 16, 2002; in final form, September 23, 2002

By using fundamental units  $c$ ,  $\hbar$ ,  $G$  as conversion factors, one can easily transform the dimensions of all observables. In particular, one can make them all “geometrical,” or dimensionless. However, this has no impact on the fact that there are three fundamental units,  $G$  being one of them. Only experiment can tell us whether  $G$  is basically fundamental. © 2002 MAIK “Nauka/Interperiodica”.

PACS numbers: 06.20.Fn; 06.20.Jr

It is well known [1] that to each mass  $M$  there corresponds a characteristic length  $r_g$ , the so-called gravitational radius (a body with radius  $r = r_g$  forms a black hole):

$$r_g = 2GM/c^2,$$

where  $G$  is gravitational constant

$$G = 6.673(10) \times 10^{-11} \text{ m}^3/\text{kg s}^2,$$

while  $c$  is velocity of light. Thus, in all physical equations,  $M$  can be replaced by  $r_g$ , so that mass can be “exorcised” from definitions of all physical observables. As a result, everything can be measured in “geometrical” units of length  $L$  and time  $T$  instead of standard  $L, T, M$  units.

One can use  $M' = GM$  instead of  $M$  in order to reduce all measurements in physics to measurements of space and time intervals and exorcise  $G$  from all equations of physics, thus reducing the number of fundamental dimensional constants. We would like to make a few rather trivial remarks concerning this proposal.

First, it is obvious that, in defining  $M'$ , one can use  $GMg(L, T)$  instead of  $GM$ , where  $g$  is an arbitrary function of geometric units  $L, T$ , in particular, in the standard case of gravitational radius  $g = 2/c^2$ .

Second, as is well known (see, e.g., [2]),  $c, \hbar, G$  are fundamental units in the sense that  $c$  represents relativity,  $\hbar$  represents quantum mechanics, while Planck mass  $m_p = \sqrt{\hbar c/G}$  is connected with the space–time scales  $l_p = \hbar/m_p c$  and  $t_p = l_p/c$  at which gravity must become strong and of a quantum character. In contrast, units based on  $M'$  have no fundamental character.

Third, by using any of three fundamental units as a conversion factor, one does not reduce the number of fundamental units and dimensions. E.g. when using  $c$  as a unit of velocity, one obviously preserves it as a fundamental unit. At the same time, one can measure time in units of length or length in units of time. However, length remains length, while time remains time. Similar considerations are valid for mass  $M, G$  and gravitational radius  $r_g$  or any combination of the type  $GMg(L, T)$ .

Of course, if  $G$  turns out to be only an “effective constant,” as is the case in theories in which gravity is modified at submillimeter distances (see, e.g. [3]), then new physics will appear well below Planck mass, maybe even at a few TeV, thus changing the value of fundamental mass. In the case that  $G$  is only an effective constant, a new dimensionless parameter would appear in low-energy physics:  $m_{\text{pl}}^{\text{new}}/m_{\text{pl}}^{\text{old}}$ . Thus, the question posed in the title of this letter could be answered by further study of the nature of gravity. Another approach to fundamental units, including  $G$ , one can find in [4].

This work was partly supported by the Russian Foundation for Basic Research, project no. 00-15-96562.

## REFERENCES

1. L. D. Landau and E. M. Lifshitz, *Course of Theoretical Physics, Vol. 2: The Classical Theory of Fields* (Nauka, Moscow, 1988; Pergamon, Oxford, 1975).
2. M. Duff, L. Okun, and G. Veneziano, physics/0110060.
3. V. Rubakov, Usp. Fiz. Nauk **171**, 913 (2001) [Phys. Usp. **44**, 871 (2001)].
4. G. Volovik, Pis'ma Zh. Éksp. Teor. Fiz. **76**, 89 (2002) [JETP Lett. **76**, 77 (2002)].

<sup>¶</sup>This article was submitted by the authors in English.

# Observation of the Rotational Doppler Effect for Optical Beams with Helical Wave Front Using Spiral Zone Plate

I. V. Basistiy<sup>1</sup>, A. Ya. Bekshaev<sup>2</sup>, M. V. Vasnetsov<sup>1</sup>, V. V. Slyusar<sup>1</sup>, and M. S. Soskin<sup>1</sup>

<sup>1</sup> *Institute of Physics, National Academy of Sciences of Ukraine, Kiev, 03039 Ukraine*

<sup>2</sup> *Mechnikov National University, Odessa, 65026 Ukraine*

Received September 12, 2002; in final form, September 26, 2002

A rotating spiral zone plate was used to implement and measure the rotational Doppler effect for plane-polarized optical beams with helical wave front (optical vortices). The frequency shift was analyzed in terms of energy exchange between the beams and moving optical elements. © 2002 MAIK “Nauka/Interperiodica”.

PACS numbers: 42.25.Hz; 42.25.Ja

Optical beams with helical wave front possess a number of fundamental properties, studies of which allowed the revision of a broad class of phenomena in both optics and wave physics as a whole. The related wave-front singularities became the subject of a large body of research [1–4]. An important point is that such beams are macroscopic objects, whose behavior pictorially manifests some specific properties of quantum systems. In particular, these beams possess orbital angular momentum [5, 6], leading to specific phase and frequency transformations upon beam rotation.

We will consider these transformations by an example of stable Laguerre–Gaussian (LG) laser resonator modes, which traditionally serve as useful models for studying wave-front singularities [1–3, 5, 7]. If the beam axis is aligned with the  $z$  axis, the electric-field distribution in the  $LG_p^l$  mode can be represented as [8]

$$E_{p,l}(\mathbf{r}, z, t) \sim \left(\frac{r}{b}\right)^{|l|} L_p^{|l|}\left(\frac{r^2}{b^2}\right) \times \exp\left(-\frac{r^2}{2b^2} + ik\frac{r^2}{2R}\right) \exp[i(kz + l\phi - \omega t)], \quad (1)$$

where  $k$  and  $\omega$  are the light wave number and frequency, respectively;  $p$  and  $l$  are the radial and azimuthal mode indices;  $\mathbf{r}$  is the radius vector;  $r$  and  $\phi$  are the polar coordinates in the beam cross section; and  $L_p^{|l|}$  stands for the Laguerre polynomial. In Eq. (1),  $b$  is the  $e^{-1}$  intensity radius and  $R$  is the front curvature radius for the lowest mode (Gaussian beam,  $p = l = 0$ ). Our interest is mainly focused on the last exponential term in Eq. (1), because it accounts for the helical wave-front form. This term is responsible for the energy flux circulation in the beam, i.e., for the optical vortex (OV) [1–3], whose measure is determined by the orbital angular momentum equal to  $\hbar h$  per photon [3, 5] and by the rotational Doppler effect (RDE). The latter consists in the appearance of

the dependence of light frequency measured by a detector on the relative rotational motion of the beam and an observer [7, 9–11]. In Eq. (1), the beam rotation and translational motions correspond to the coordinate transformations

$$\phi \longrightarrow \phi - \Omega t, \quad z \longrightarrow z - vt \quad (2)$$

(positive direction of the angular  $\Omega$  and translational  $v$  velocities coincide with the direction of the  $z$  axis). As a result, the observed phase variation rate, i.e., the beam frequency in Eq. (1), becomes  $\omega = \omega + \Delta\omega$ , where

$$\Delta\omega = kv + l\Omega; \quad (3)$$

i.e., apart from the translational Doppler effect (the first term), the rotation-induced frequency shift may occur (the second term). This frequency shift can also be explained in terms of energy exchange between the beam electromagnetic field containing OV and optical elements [7, 12, 13].

The RDE was first observed for the beams with spin angular momentum caused by circular polarization [9, 12]. For the LG modes, it was predicted in [7, 10] and measured in [14, 15] using electromagnetic waves in the millimeter range.

In this work, the RDE is demonstrated for beams with orbital angular momentum in purely optical experiments, which have become possible due to the use of rotating spiral zone plates (SZP).

SZP is a record of the interference pattern for the coaxial LG beam and plane wave. About ten years ago, the corresponding synthesized holograms were intended for use for the transformation of beams with smooth front into vortical beams [16], but they did not find wide use, because different diffraction orders were not spatially separated in this case. As to the RDE, this shortcoming transforms into an advantage, because it is important for the interferometric observations of frequency shifts that the beam propagation directions do not change upon the rotation of optical element.

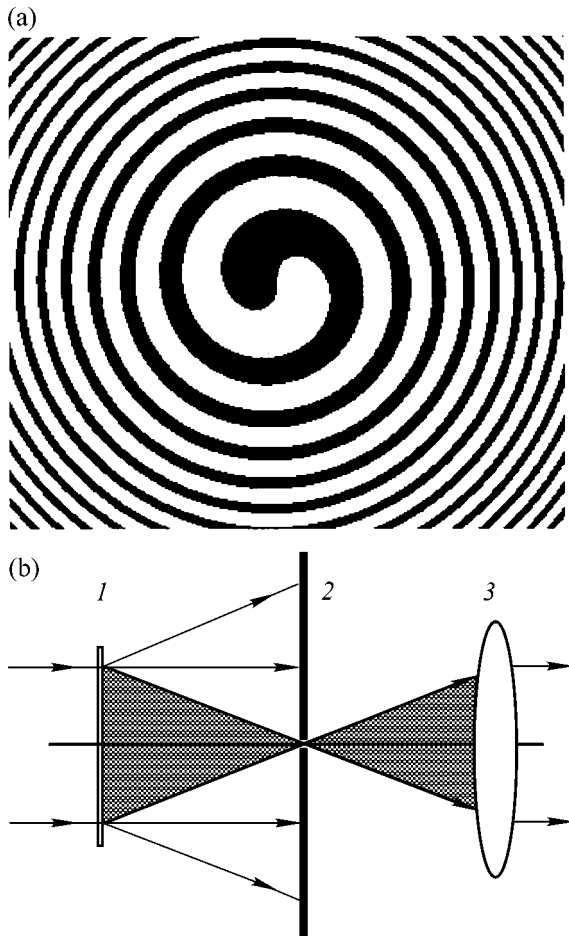


**Fig. 1.** (a) Central area of the spiral zone plate and (b) scheme of separation of the first-order diffracted beam: (1) SZP, (2) point aperture, and (3) collimating lens; the separated beam is gray-shaded.

The central SZP fragment is depicted in Fig. 1a. It represents a transparency with the spatially dependent transmission

$$\begin{aligned}
 T(\mathbf{r}) &\sim 1 + \operatorname{sgn} \left[ \cos \left( \frac{kr^2}{2f} + m\phi \right) \right] \\
 &= \sum_N \frac{2}{N\pi} \sin \left( \frac{N\pi}{2} \right) \exp \left[ iN \left( \frac{kr^2}{2f} + m\phi \right) \right],
 \end{aligned}
 \tag{4}$$

where  $m$  is the topological charge of the phase singularity built in the plate (in Fig. 2a  $|m| = 1$ ),  $f$  is the plate focal parameter, and  $N$  is an integer (diffraction order). When illuminating the SZP by the wave with plane front, converging (for  $N > 0$ ) and diverging (for  $N < 0$ ) spherical waves are formed (Fig. 1b), with the focal plane for the  $N$ -order wave being positioned at the distance  $f_N = f/N$  behind the plate.

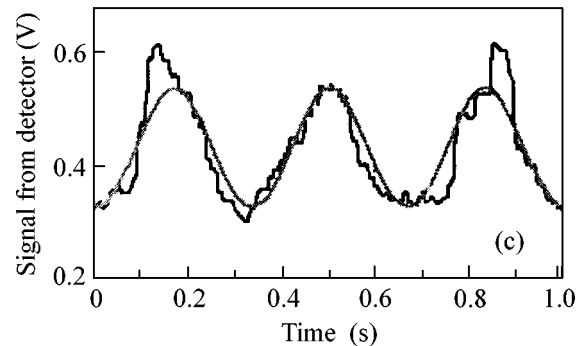
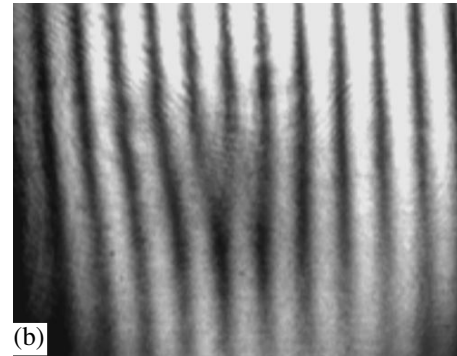
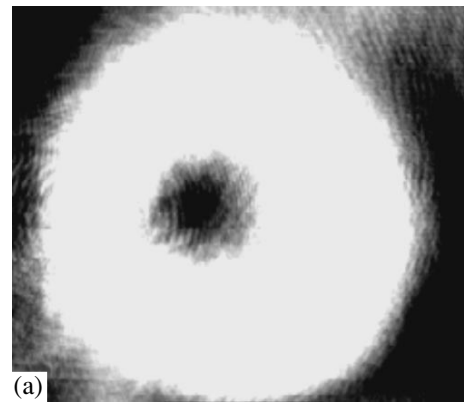


**Fig. 2.** (a) Transverse intensity distribution in the separated first-order diffracted beam, (b) its interference pattern with the reference beam, and (c) oscillogram of the detector signal upon the SZP rotation. Sinusoid corresponds to the fundamental beat frequency.

Immediately behind the plate, the light field of the diffracted  $N$ -order beam is described by the relationship

$$E_N(\mathbf{r}, t) = u(r) \exp(iNm\phi - i\omega t), \tag{5}$$

where  $u(r)$  is a function determined by the complex amplitude of the incident (initial) beam and by the focusing power of the SZP for this order. In contrast to the usual zone plate, this beam carries OV with topological charge  $l = mN$  which determines its orbital angular momentum. Note that, according to Eq. (4), only the odd orders can be observed.

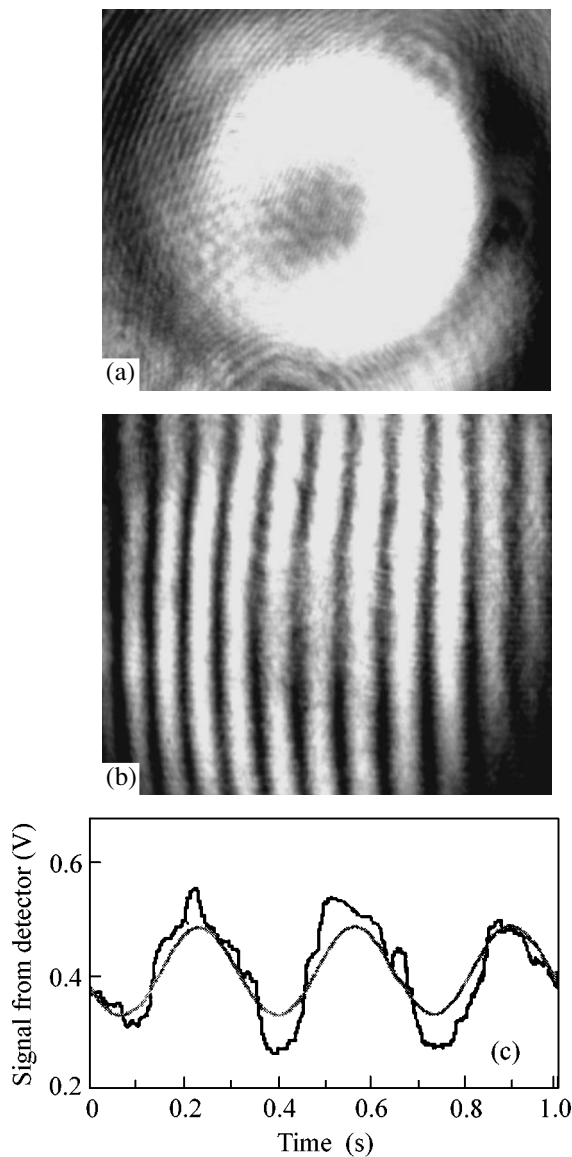


**Fig. 3.** Transformation of a beam with unit-charge OV into a vortex-free beam in the rotating SZP: (a) intensity distribution in the first-order diffracted beam, (b) its interference pattern with the reference beam, and (c) oscillogram of the detector signal upon the SZP rotation.

In the experimental setup, SZP was obtained by photographing the pattern calculated on a computer with a high-resolution printout. The slide was installed in the inner ring of a rotating device, which made it possible to rotate SZP by electric motor. The initial plane-polarized Gaussian beam from a He–Ne laser (wavelength  $0.63 \mu\text{m}$ ) was formed in such a way that its axis coincided with the rotation axis and the waist ( $b \approx 0.7 \text{ mm}$ ) was situated in the SZP plane. The transverse size ( $5 \text{ mm}$ ) of the image in the slide excluded the influence of aperture effects caused by edge diffraction.

The desired (first) diffraction order with unit-charge OV was separated using a point aperture placed in the SZP focal plane corresponding to  $N = 1$  (Fig. 1b); for the SZP used,  $f_1 = f = 7.5 \text{ cm}$ . The resulting beam was collimated by a lens, and its transverse intensity distribution displayed a dip near the axis, typical of phase singularity (Fig. 2a). To study this beam, it was led to the measuring arm of a Mach–Zehnder interferometer, in which the reference wave was produced by splitting off a portion of initial beam followed by its collimation. The alignment of the output beam splitter provided suitable scale of the interference pattern for the observation in the plane for analysis. The image of this pattern contains a fork typical of unit-charge OV (Fig. 2b), confirming the presence of OV in the diffracted beam. It also followed that the radiation passing through the point aperture did not reveal any noticeable presence of zero and other parasitic diffraction orders. The beam was slightly depolarized due to the birefringence in the film material.

Therefore, the device depicted in Fig. 1b can be regarded as a source of an optical beam with helical wave front. If SZP is rotated with a constant angular velocity  $\Omega$  about the system axis, all diffracted beams will also rotate. The SZP rotation is equivalent to coordinate transformation (2), as a result of which the  $N$ -order beam behind the rotating plate is described by the expression

$$E_N(\mathbf{r}, t, \Omega) = u(r) \exp(iNm\phi - iNm\Omega t - i\omega t) \\ = u(r) \exp[iNm\phi - (Nm\Omega + \omega)t] \quad (6)$$

instead of Eq. (5). This signifies that the observed beam frequency changes by  $\Delta\omega = Nm\Omega$ . Therein lies the manifestation of RDE in the system with rotating SZP (for the particular experimental situation with  $\Delta\omega = \Omega$ ).

Because of the frequency difference between the diffracted and reference beams, the system of interference fringes starts to move. This movement was recorded by a photodetector equipped with an aperture of size smaller than the period of the interference pattern. The oscillogram of the photodetector signal proportional to the light flux through the aperture is shown in Fig. 2c (after filtration of the line-modulated laser power). The period of the observed beats exactly corresponded to the angular velocity of SZP rotation ( $3 \text{ s}^{-1}$ ).

To eliminate possible systematic errors, the analogous experiment was carried out with the zero-order beam. The latter was obtained using lens with a focal length of  $1 \text{ m}$  placed immediately ahead of SZP; at distances larger than  $f_1$  behind the SZP, all diffracted beams diverged strongly, whereas the zero-order beam converged at the lens focus and, hence, can be separated using a diaphragm. In this case, nor the fork neither the fringe movement was observed in the interference pattern upon SZP rotation.

If a SZP with topological charge  $m = 2$  was used, then, in compliance with Eq. (6), the charge of OV in

the first-order diffracted beam was 2, and the beat frequency in the detector signal doubled upon the SZP rotation.

Also of interest is the situation where the initial beam contains the OV with a certain topological charge  $n$ , so that its complex amplitude is proportional to  $\exp(in\phi)$ . In this case, one has instead of Eq. (6)

$$E_N^n(\mathbf{r}, t, \Omega) = u_n(r) \exp[i(Nm + n)\phi - i(Nm\Omega + \omega)t],$$

and it then turns out that the frequency shift upon the rotation of a beam with  $l = Nm + n$  is equal to  $Nm\Omega$ ; i.e., the relation  $\Delta\omega = l\Omega$  given by the second term on the right-hand side of Eq. (3) is no longer valid. In particular, for  $n = -Nm$  the frequency shift can be observed even in a vortex-free beam. We examined this case (with  $N = m = -n = 1$ ) experimentally. Although the spatial intensity distribution in the diffracted beam has a dip in the center (Fig. 3a), the interference pattern in Fig. 3b shows no singularity, while the oscillogram of the detector signal (Fig. 3c) unambiguously indicates the presence of RDE.

The situation is understandable if the OV transformations in SZP are taken into account. The initial beam carries photons with orbital angular momentum  $n\hbar$  to the plate; behind the plate, the photon angular momentum in the  $N$ th order equals  $(Nm + n)\hbar$ . Hence, each photon acquires angular momentum  $Nm\hbar$ , so that a recoil torque is applied to the plate. In the course of rotation, the work against this torque changes the photon energy by  $\Delta\varepsilon = Nm\hbar\Omega$  [7, 13]. Hence it follows from the relation  $\Delta\varepsilon = \hbar\Delta\omega$  that  $\Delta\omega = Nm\Omega$ , irrespective of the OV charge in the diffracted beam.

Note in conclusion that the results obtained in this work are important for information coding through the control of the orbital angular momenta of optical beams [17].

## REFERENCES

1. *Horizons in World Physics*, Vol. 228: *Optical Vortices*, Ed. by M. Vasnetsov and K. Staliunas (Nova Science, Huntington, 1999).
2. M. S. Soskin and M. V. Vasnetsov, *Prog. Opt.* **42**, 219 (2001).
3. L. Allen, M. J. Padgett, and M. Babiker, *Prog. Opt.* **39**, 291 (1999).
4. M. V. Berry, *Nature* **403**, 21 (2000).
5. L. Allen, M. W. Beijersbergen, R. J. C. Spreeuw, and J. P. Woerdman, *Phys. Rev. A* **45**, 8185 (1992).
6. J. Leach, M. J. Padgett, S. M. Barnett, *et al.*, *Phys. Rev. Lett.* **88**, 257901 (2002).
7. G. Nienhuis, *Opt. Commun.* **132**, 8 (1996).
8. Yu. A. Anan'ev, *Laser Resonators and the Beam Divergence Problem* (Adam Hilger, Bristol, 1992).
9. B. A. Garetz, *J. Opt. Soc. Am.* **71**, 609 (1981).
10. L. Allen, M. Babiker, and W. L. Power, *Opt. Commun.* **112**, 141 (1994).
11. I. Bialynicki-Birula and Z. Bialynicka-Birula, *Phys. Rev. Lett.* **78**, 2539 (1997).
12. F. Bretenaker and A. Le Floch, *Phys. Rev. Lett.* **65**, 2316 (1990).
13. A. Ya. Bekshaev, *Opt. Spektrosk.* **88**, 993 (2000) [*Opt. Spectrosc.* **88**, 904 (2000)].
14. J. Courtial, K. Dholakia, D. A. Robertson, *et al.*, *Phys. Rev. Lett.* **80**, 3217 (1998).
15. J. Courtial, D. A. Robertson, K. Dholakia, *et al.*, *Phys. Rev. Lett.* **81**, 4828 (1998).
16. N. R. Heckenberg, R. McDuff, C. P. Smith, and A. G. White, *Opt. Lett.* **17**, 221 (1992).
17. G. Molina-Terriza, J. P. Torres, and L. Torner, *Phys. Rev. Lett.* **88**, 013601 (2002).

*Translated by V. Sakun*

## Time-Resolved X-ray Spectroscopy of Hot Spots in an X-pinch

S. A. Pikuz\*, D. B. Sinars\*\*, T. A. Shelkovenko\*, K. M. Chandler\*\*,  
D. A. Hammer\*\*, I. Yu. Skobelev\*\*\*, and G. V. Ivanenkov\*

\*Lebedev Physical Institute, Russian Academy of Sciences, Leninskii pr. 53, Moscow, 119991 Russia  
e-mail: ivanenkv@sci.lebedev.ru

\*\*Laboratory of Plasma Studies, 369 Upson Hall Cornell University, Ithaca NY, 14853 USA

\*\*\*Center of Spectral Data for Multicharge Ions, Research Institute of Physicotechnical Radio Engineering Measurements,  
Mendeleevo, Moscow region, 141570 Russia

Received September 6, 2002

The plasma parameters in hot spots of an X-pinch are determined by using time-resolved data from X-ray spectroscopy in experiments on the implosion of crossed Ti wires in the XP device with a current of 480 kA and pulse duration of 100 ns. The electron densities and temperatures calculated from these data are in the ranges  $(0.8\text{--}3) \times 10^{23} \text{ cm}^{-3}$  and 1–2.5 keV, respectively. An analysis performed shows that the plasma processes are highly nonequilibrium. © 2002 MAIK “Nauka/Interperiodica”.

PACS numbers: 52.80.Qj; 52.70.La; 52.25.Os

The measurements of the parameters of hot spots (HSs) in X-pinchs are still a rather difficult problem that requires modern, high-precision apparatus. Recent experiments [1–5] have shown that, near the point of maximum compression, the plasma parameters vary on picosecond temporal scales and micron spatial scales. Theoretical estimates and numerical simulations predict plasma densities higher than solid-state densities and temperatures in the keV range [2, 4, 5]. The only source of information about plasmas with such parameters is X-ray spectroscopy. It is clear, however, that methods based on recording time-integrated spectra (even with high spatial resolution) can only provide averaged or incorrect data. In this paper, the plasma parameters are determined from time-resolved spectral measurements by using a high-aperture, slitless scheme with an X-ray streak camera and a spherically bent focusing crystal (Fig. 1).

Experiments with 100-ns current pulses (with a current of up to 480 kA) were carried out in the XP device at Cornell University (USA). X-pinchs were produced by the implosion of two to eight crossed wires made of different metals [1, 4, 6]. The spectrum of X-ray plasma emission was resolved with the help of a spherically bent mica crystal with a radius of curvature of 150 or 186 mm. The emission was focused into a narrow strip on the photocathode of a streak camera (Fig. 1). The strip width ( $<30\text{--}50 \mu\text{m}$ ) was determined by the quality of the crystal and the size of the radiation source, whose image was demagnified by five to seven times. According to our previous measurements, the source diameter did not exceed several tens of microns, and the quality of the crystal guaranteed focusing into a 10- to 20- $\mu\text{m}$

strip. The electrostatic system of the streak camera blurred the strip image on the output screen to  $\approx 120 \mu\text{m}$ . The time resolution of the system was 7–10 ps, which was close to the maximum resolution provided by the employed Kentech streak camera (see [4] for details). The time-scanning image of the spectrum was recorded on a 60-mm Kodak TWAX400 film pressed against the fiber-optic faceplate of the camera. Photographs were digitized with an Agfa Arcus II scanner and then were corrected for the distortion introduced by the camera, the film sensitivity, and the scanner transfer characteristic. In this paper, we present the results from experiments with a seven-wire Ti array, the wire diameter being 17  $\mu\text{m}$ .

Figure 2 shows the time dependences of the plasma emission intensity in the wavelength ranges 2.615–2.624, 2.629–2.638, 2.642–2.651, 2.489–2.498, and 2.500–2.509 Å. These spectral ranges were chosen so as to trace the intensities of the following lines: (i) the  $\text{He}_{\alpha 1}$  resonance line of helium-like Ti XXI ions, (ii) the  $\text{He}_{\alpha 2}$  intercombination line of Ti XXI ions, (iii) the  $k$  and  $j$  satellites corresponding to the  $1s2p^{22}D\text{--}1s^22p^2P$  transitions of Ti XX ions, (iv) the  $\text{Ly}_{\alpha}$  resonant line of hydrogen-like Ti XXII ions, and (v) transitions in the continuum. It can be seen in the figure that there are three emission peaks in the time interval 0–600 ps. It is reasonable to attribute these peaks to three HSs that arise in the course of pinching. The first burst is the shortest ( $\approx 50$  ps). The duration of the second burst in the  $\text{Ly}_{\alpha}$  line is also  $\approx 50$  ps; however, for the  $\text{He}_{\alpha 1,2}$  lines, the emission time is significantly longer ( $\approx 80$  ps). The duration of the third burst in the  $\text{He}_{\alpha 1,2}$  lines is

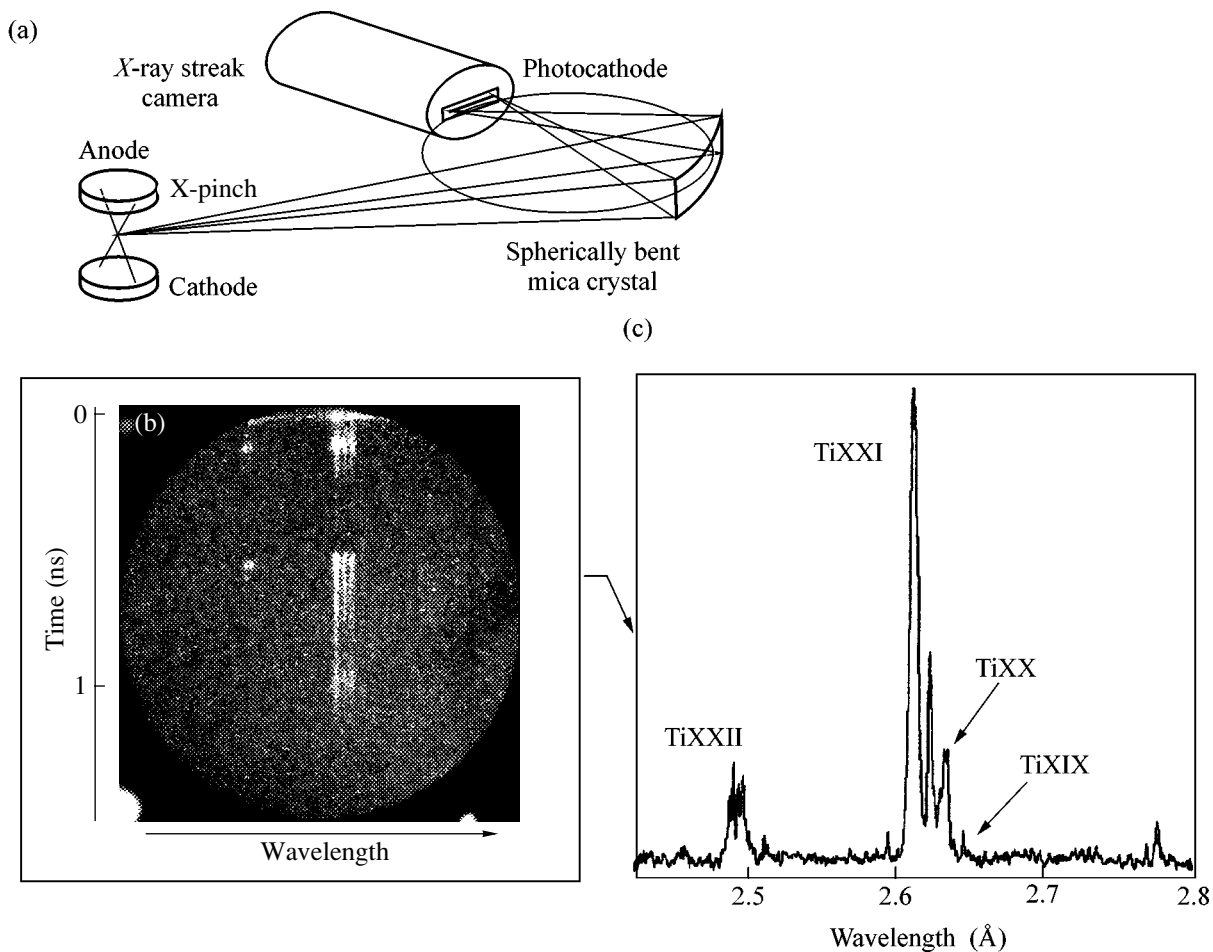


**Fig. 1.** Schematic of the experiment and the densitogram of the time-resolved emission spectrum of a Ti X-pinch.

$\approx 110$  ps, whereas the durations of the emission bursts in the  $Ly_{\alpha}$  line and in the  $k$  and  $j$  satellites is  $\approx 50$  ps as before.

The above difference between the durations of the emission bursts may be attributed to the specific features of the excitation of the resonance and satellite lines of hydrogen- and helium-like ions. The  $2p$  and  $1s2p$  levels of these ions can be populated from the  $1s$  and  $1s^2$  ground states by electron impact or by the triple or radiative recombination of stripped nuclei or hydrogen-like ions. The doubly excited  $1s^2p^2$  states are populated predominantly by dielectronic capture from the ground  $1s^2$  state of a helium-like ion. It is important that, in this mechanism for reducing the ion charge (unlike the other recombination mechanisms), energy is taken from free electrons, which requires that the plasma temperature be sufficiently high. Plasma cooling during the HS decay decreases the efficiency of electron-impact excitation and dielectronic capture, which are the main channels for the population of the ion levels when energy is transferred from free to bound electrons. In fact, the capture is a unique channel for the generation of the  $k$  and  $j$  satellites; thus, the emission

time of these lines determines the lifetime of a high-temperature plasma. In this way, we can estimate the HS lifetime, which appears to be  $\approx 50$  ps. In contrast,

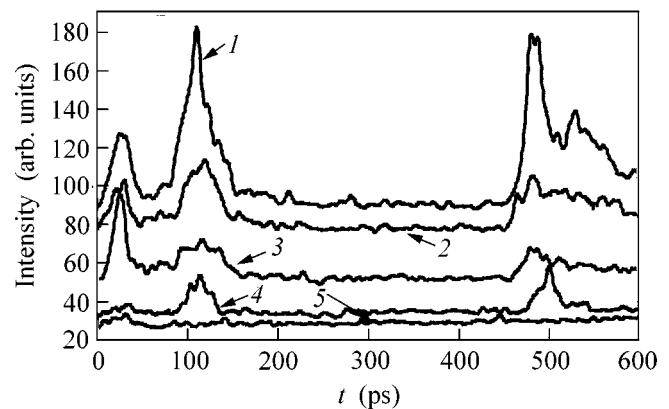


**Fig. 2.** Time dependences of the intensity of plasma emission from an X-pinch in the spectral ranges (1) 2.615–2.624, (2) 2.629–2.638, (3) 2.642–2.651, (4) 2.489–2.498, and (5) 2.500–2.509 Å.

**Table**

| Burst number | $t$ (ps) | $T_e$ (keV) | $N_e$ (cm $^{-3}$ ) |
|--------------|----------|-------------|---------------------|
| 1            | 32       | 1.25        | $3 \times 10^{23}$  |
| 2            | 88       | 1.70        | $10^{23}$           |
|              | 95       | 1.75        | $8 \times 10^{22}$  |
|              | 102      | 2.10        | $8 \times 10^{22}$  |
|              | 109      | 2.10        | $6 \times 10^{22}$  |
|              | 116      | 1.65        | $2 \times 10^{22}$  |
|              | 123      | 1.4         | $< 10^{22}$         |
| 3            | 130      | 1.15        | $< 10^{22}$         |
|              | 480      | 1.5         | $5 \times 10^{22}$  |
|              | 487      | 2           | $6 \times 10^{22}$  |
|              | 494      | 2.4         | $10^{23}$           |
|              | 501      | 2.5         | $10^{23}$           |
|              | 508      | 2.4         | $9 \times 10^{22}$  |

the resonance states of a cooling plasma can rather efficiently be populated via both triple and radiative recombination, because their probabilities increase with decreasing temperature. Hence, if there are a sufficient number of stripped nuclei (hydrogen-like ions) in a plasma, then the duration of  $Ly_\alpha$  ( $He_{\alpha 1,2}$ ) line emission will exceed the duration of the high-temperature phase. Seemingly, under our experimental conditions, there were no stripped Ti nuclei in the plasma, and an appreciable amount of hydrogen-like Ti XXII ions was produced only in the second and third HSs (Fig. 2, curve 4). For this reason, there was no recombination excitation of the  $Ly_\alpha$  line; hence, the emission time of this line was also interpreted as the HS lifetime. In the first HS, because of the lack of hydrogen-like Ti XXII ions, this excitation mechanism was also forbidden for

the  $He_{\alpha 1,2}$  lines. However, in the second and third HSs, the fraction of hydrogen-like Ti ions amounted to  $\approx 30\%$  and  $\approx 45\%$ , respectively, and recombination excitation prolonged the emission bursts in the  $He_{\alpha 1,2}$  lines by 30–60 ps (Fig. 2; curves 1, 2). Note that a similar effect in the spatial distribution of the emission intensity of helium-like Mg XI ions in an expanding laser plasma was previously observed in [7].

The X-pinch emission spectra shown in Fig. 1 allowed us to determine the time behavior of the HS plasma parameters. For this purpose, we used the conventional quasi-steady radiative–collisional kinetic model and calculated the emission spectrum of the helium-like Ti XXI ions with dielectronic satellites corresponding to transitions in lithium-like Ti XX ions. For a sufficiently hot plasma, the model spectrum depends only on the electron density  $N_e$  and temperature  $T_e$ , which can be determined by fitting the model spectra to observations. As was expected, the intensity ratio of  $He_{\alpha 1}$  and  $He_{\alpha 2}$  lines was most sensitive to the plasma density, whereas the ratio of the  $k$  and  $j$  satellites was most sensitive to the plasma temperature. The results obtained are presented in the table, and the quality of the model is demonstrated by Fig. 3, which shows the experimental spectrum measured at  $t = 494$  ps and the results of calculations for  $N_e = 10^{23}$  cm $^{-3}$  and  $T_e = 2400$  eV. It can be seen from the table that the plasma temperature in the first HS does not exceed 1250 eV, and the maximum electron density is  $3 \times 10^{23}$  cm $^{-3}$ . In the second HS, the plasma is heated to 2100 eV, and its density is several times lower ( $0.8 \times 10^{23}$  cm $^{-3}$ ). A maximum temperature of 2500 eV is achieved in the third HS at a density of  $10^{23}$  cm $^{-3}$ .

If the plasma were in a quasi-steady ionization state, the density ratio of hydrogen- and helium-like Ti ions would be  $\approx 0.07$  in the first HS,  $\approx 0.09$  in the second HS, and  $\approx 2$  in the third HS. For temperatures of  $\geq 1$  keV, the excitation rate of the  $2p^2P$  level by electron impact from the ground state is nearly equal to that of the  $1s2p^1P_1$  level [8]. In this case, the relative intensities of the  $Ly_\alpha$  and  $He_{\alpha 1}$  lines should also be close to each other. Nevertheless, as can be seen in Fig. 2, the intensity of the  $Ly_\alpha$  line is significantly lower than its steady-state value, and the plasma emission in the  $Ly_\alpha$  line is somewhat delayed with respect to the emission burst in the  $He_{\alpha 1,2}$  lines. As was shown in [5], this is because the quasi-steady kinetic model is inapplicable to describing the evolution of the ionization state of an X-pinch plasma. Indeed, an analysis of the ionization–recombination rates shows that a time of  $\approx 20$ – $50$  ps is required for hydrogen-like Ti XXII ions to reach their steady-state density at the plasma parameters given in the table; however, this time is comparable with the HS lifetime. In this case, the relative density of hydrogen-

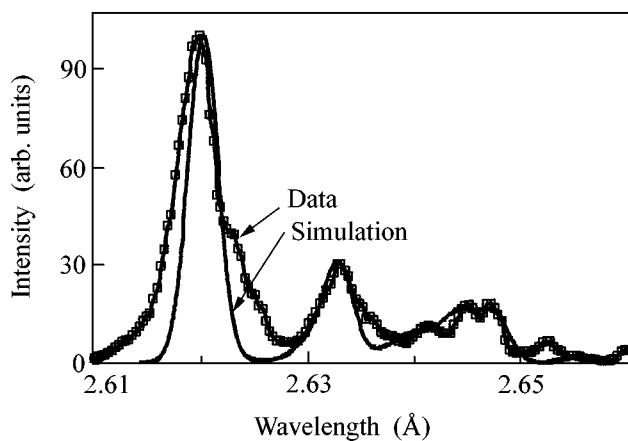


**Fig. 3.** Emission spectrum of an X-pinch plasma at  $t = 494$  ps and the results of calculations for  $N_e = 10^{23}$  cm $^{-3}$  and  $T_e = 2.3$  keV.

like ions should be determined from the time-dependent kinetic equation

$$\begin{aligned} dN_{\text{H}}/dt = & -N_{\text{H}}(W_{\text{H}\rightarrow\text{Z}^*} + W_{\text{H}\rightarrow\text{He}}) \\ & + N_{\text{He}}W_{\text{He}\rightarrow\text{H}} + N_{\text{Z}^*}W_{\text{Z}^*\rightarrow\text{H}}, \end{aligned}$$

where  $N_{\text{Z}^*}$ ,  $N_{\text{H}}$ , and  $N_{\text{He}}$  are the densities of the excited ions and hydrogen- and helium-like ions, respectively, and  $W_{a\rightarrow b}$  are the probabilities of the ionization and recombination processes. The solution to this equation was used to construct the time behavior of the intensity ratio  $I(\text{H})/I(\text{He})$  for the  $\text{Ly}_{\alpha}$  and  $\text{He}_{\alpha 1}$  lines in the second and third HSs. This ratio is presented in Fig. 4 along with the experimental data. It can be seen in Fig. 4 that the model adequately describes the observed dependences, which confirms that the plasma parameters are determined correctly.

What are the characteristic features of plasma dynamics in this state? A great body of information obtained in previous experiments [1–5] allows us to distinguish slow and fast hydrodynamic phases in the X-pinch compression. In both phases, the substance moves with the ion acoustic velocity  $c_s = (ZT_e/m_i)^{1/2}$ , but the characteristic time (the ratio of the radius  $a$  to  $c_s$ ) in the fast phase is shorter than the energy-exchange time between electrons and ions  $\tau_{ei} = m_i T_e^{3/2} / 2(\pi m_e)^{1/2} e^4 \Lambda Z^2 N_e$ . Hence, in the course of accelerated magnetic implosion, electrons have no time to transfer the excess heat to ions. The remainder is spent on other processes, including the ionization and excitation of ions; later, plasma compression is intensified by radiation. Therefore, the temperature-relaxation time in the transition from the first to the second phase is  $\tau_{ei} = a/c_s$ ; further, this time can be used as an upper estimate for the duration of the fast phase. In the experimental pictures, the transient phase is characterized by the existence of a constriction nearly 10  $\mu\text{m}$  in diameter. The plasma parameters at the periphery ( $N_e = 10^{21}$ – $10^{22} \text{ cm}^{-3}$  and  $T_e = 100$ – $200 \text{ eV}$ ) are still insufficiently high for the thermal excitation of lines in the observed spectral region; however, these parameters are close to those required for the condition  $a = c_s \tau_{ei}$  to be satisfied (where  $c_s = (4$ – $6) \times 10^6 \text{ cm/s}$  and  $\tau_{ei} = 40$ – $90 \text{ ps}$ ). Then, the constriction as a whole slowly evolves, and small-scale fast instability develops against this background evolution. The instability gives rise to next-order constrictions, in which, in turn, new narrower constrictions are formed, etc.; i.e., we are dealing with a cascade process [9]. We can assume that the continuum at the beginning of the X-ray burst in Fig. 1 refers just to the end of this cascade process. This is always associated with the minimum constriction diameter, whose measurement, however, is still beyond the capability of experimental techniques. In any case, it is  $< 1$ – $2 \mu\text{m}$  [5, 6] (in X-ray images, minimum diameters of 3–4  $\mu\text{m}$  can only be resolved). The radiation temperature is not too high: estimates by the foil technique give  $\leq 1 \text{ keV}$  for a

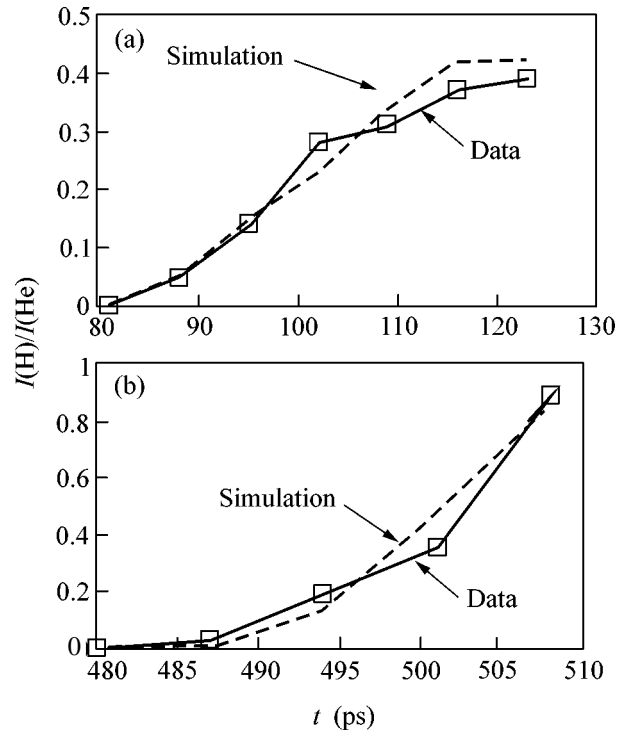


Fig. 4. Observed and calculated time dependences of the intensity ratio  $I(\text{H})/I(\text{He})$  of the  $\text{Ly}_{\alpha}$  and  $\text{He}_{\alpha 1}$  lines.

Ti X-pinch and 600–800 eV for heavier metals. In the spectrum of a Mo X-pinch, the lines of multicharged ions are absent during the first several picoseconds [5]. In the spectrum of a Ti X-pinch under study, the continuum arises in the first X-ray burst (Fig. 1); in this case, the continuum intensity is comparable with the line-emission intensity of multicharged Ti ions, and the total energy is substantially higher than the energy emitted in lines.

Using the plasma parameters determined in this study, we find that the thermalization time is  $\tau_{ei} \approx 3 \text{ ps}$  in the first HS and  $\approx 25 \text{ ps}$  in the other two HSs. Assuming  $c_s \approx 10^7 \text{ cm/s}$ , we estimate the corresponding HS dimensions at  $\approx 0.4$  and  $\approx 0.6 \mu\text{m}$ . Note that the radiative plasma compression comes in to play when the radius becomes comparable to the average Planck's photon mean free path. In this case, since the right-hand side of the inequality  $a < c_s \tau_{ei}$  is the ratio of the electron heat diffusivity to  $c_s$  and the distribution of  $T_e$  is uniform across the formed constriction throughout the entire rapid compression phase, radiation becomes the main cooling mechanism. This mainly concerns the first HS (because its plasma is compressed to a larger extent than is heated); however, the amount of hydrogen-like Ti ions in this HS is small as compared to the other two HSs. Therefore, we can only say about a tendency of radiative plasma compression in our experiment with a Ti X-pinch.

All the experimental data and theoretical estimates indicate that the physical phenomenon known in the integral measurements as a “hot spot” is actually associated with a sequence of rapidly changed plasma states. If we restrict ourselves to the phases in which X-ray emission is not too hard ( $<10$  keV), then two types of plasma can be distinguished. The parameters of the first type of HS with a short-lived, relatively cold and dense plasma are still poorly known and can only be estimated. With some degree of certainty, we can determine the upper bound of the lifetime, which turns out to be 10–15 ps. As was mentioned above, the temperature  $T_e$  does not exceed 1 keV and, according to energy estimates,  $N_e$  can exceed the solid-state density by one to two orders of magnitude. The second type of HS, which is the main subject of this study, is characterized by moderate parameters (the lifetime is 20–50 ps, the temperature is 1.2–2.5 keV, and the density is  $\approx 10^{23}$  cm $^{-3}$ ). The study of the formation of the first state and its transition to the second state calls for special experiments.

This work was supported by the grants of the US Department of Energy, nos. DE-FG03-98DP00217 and DE-FO2-98ER54496.

## REFERENCES

1. T. A. Shelkovenko, D. B. Sinars, S. A. Pikuz, and D. A. Hammer, *Phys. Plasmas* **8**, 1305 (2001).
2. S. A. Pikuz, T. A. Shelkovenko, D. B. Sinars, *et al.*, *J. Quant. Spectrosc. Radiat. Transf.* **72**, 581 (2001).
3. D. B. Sinars, S. A. Pikuz, T. A. Shelkovenko, *et al.*, *Rev. Sci. Instrum.* **73**, 2948 (2001).
4. T. A. Shelkovenko, S. A. Pikuz, D. B. Sinars, *et al.*, *Phys. Plasmas* **9**, 2165 (2002).
5. S. A. Pikuz, D. B. Sinars, T. A. Shelkovenko, *et al.*, *Phys. Rev. Lett.* **89**, 035003 (2002).
6. T. A. Shelkovenko, D. B. Sinars, S. A. Pikuz, *et al.*, *Rev. Sci. Instrum.* **72**, 667 (2001).
7. V. A. Boiko, B. A. Bryunetkin, B. N. Duvanov, *et al.*, *Pis'ma Zh. Tekh. Fiz.* **7**, 1430 (1981) [*Sov. Tech. Phys. Lett.* **7**, 611 (1981)].
8. L. A. Vainshtein, I. I. Sobelman, and E. A. Yukov, *Excitation of Atoms and Broadening of Spectral Lines* (Nauka, Moscow, 1978; Springer-Verlag, Berlin, 1981).
9. G. V. Ivanenkov, S. A. Pikuz, T. A. Shelkovenko, *et al.*, *Zh. Éksp. Teor. Fiz.* **118**, 539 (2000) [*JETP* **91**, 469 (2000)].

*Translated by N. Larionova*

# Theory of Exchange Coupling in Disordered Magnetic Multilayers<sup>¶</sup>

A. Yu. Zyuzin

Ioffe Physicotechnical Institute, Russian Academy of Sciences, St. Petersburg, 194021 Russia

Received September 11, 2002

We consider a mechanism of exchange coupling based on interaction between electrons in a nonmagnetic layer. Depending on the ratio of inverse time of diffusion of electrons between ferromagnetic layers and ferromagnetic splitting of conducting electrons, this mechanism describes the transition from ferromagnetic to noncollinear ordering of magnetizations of ferromagnetic layers. © 2002 MAIK “Nauka/Interperiodica”.

PACS numbers: 75.70.Cn; 75.30.Et

**1. Introduction and main results.** In the metallic ferromagnet–nonferromagnet–ferromagnet multilayers (see figure), magnetic structure oscillates between ferromagnetic and antiferromagnetic orientations of the ferromagnet magnetizations as a function of thickness of nonmagnetic metal  $L$  with a period on order of the Fermi wavelength [1–6]. The explanation of this phenomenon is based on the fact that the interlayer coupling is due to the Ruderman–Kittel interaction between electron spins in different ferromagnets.

Further investigations discovered structures with perpendicular orientations of the ferromagnetic magnetizations (see for rev. [7]). Often, the phenomenological coupling between the magnetizations of ferromagnetic layers in such structures can be represented as the sum of bilinear and biquadratic contributions

$$\Omega(\varphi) = J_1 \cos \varphi + J_2 \cos^2 \varphi. \quad (1)$$

Here,  $\varphi$  is the angle between the directions of magnetizations of ferromagnetic films. The bilinear constant  $J_1$  oscillates as a function of the interlayer distance  $L$ . In the case of the large positive biquadratic constant  $J_2$ , the minimum of  $\Omega(\varphi)$  corresponds to  $\varphi = \pi/2$ . As explained by Slonczewski, the large positive biquadratic coupling might be the result of spatial fluctuations of the bilinear coupling  $J_1$  due to the ferromagnet–nonferromagnet surface roughness [7].

In a disordered system, where  $L$  is larger than the electron mean free path  $l$ , RKKY interaction  $\langle J_1 \rangle$ , averaged over the realizations of scattering potential, exponentially decreases [8]. At the same time, fluctuations of local exchange become much larger than  $\langle J_1 \rangle$  [9], giving rise to biquadratic contribution  $J_2 \gg |\langle J_1 \rangle|$  [10].

Here, we propose a mechanism of coupling in the disordered multilayers based on interaction between electrons in the nonmagnetic layer. Spin fluctuations in

the system of interacting electrons give rise to the contribution to thermodynamic potential [11], which depends on magnetic field or, in our case, on the relative orientation of the magnetizations in ferromagnetic layers. Here, we show that, in the magnetic multilayer, this mechanism describes transition between the ferromagnetic and noncollinear ordering with increasing distance between ferromagnetic layers or increasing value of ferromagnetic splitting of conducting electrons.

We assume that the magnetic multilayer can be described by the Hamiltonian

$$H = H_0 + \epsilon_{\text{ex}} \int_F d\mathbf{r} \Psi_{\alpha}^{\dagger}(\mathbf{r}) \mathbf{n}(z) \sigma_{\alpha\beta} \Psi_{\beta}(\mathbf{r}) + H_{\text{int}}. \quad (2)$$

Here,  $H_0$  is the Hamiltonian of free electrons in random field. The second term describes the exchange field in

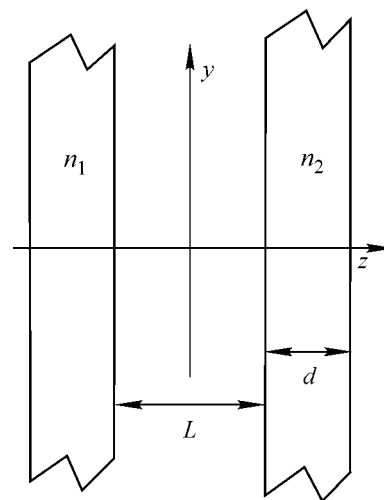


Figure.

<sup>¶</sup>This article was submitted by the author in English.

ferromagnetic layers.  $\epsilon_{\text{ex}}$  is ferromagnetic splitting of the conducting electrons;  $\mathbf{n}(z)$  is unit vector of the direction of magnetization of ferromagnetic layers;  $\mathbf{n}(z) = \mathbf{n}_1$  at  $z < -L/2$  and  $\mathbf{n}(z) = \mathbf{n}_2$  at  $z > L/2$ , as is shown in the figure;  $\Psi_{\alpha}^{+}(\mathbf{r})$  and  $\Psi_{\beta}(\mathbf{r})$  are creation and annihilation operators; and  $\sigma_{\alpha\beta}$  are Pauli matrixes. Integration in the second term is over the ferromagnetic layers. The last term  $H_{\text{int}}$  describes Coulomb interaction between electrons in the nonmagnetic layer. We assume that the interaction in the ferromagnetic layers is taken into account self-consistently in  $\epsilon_{\text{ex}}$ .

The details of calculation are given in the last part of the paper. Here, we present the main results. Characteristic energies in the problem are ferromagnetic splitting of conducting electrons  $\epsilon_{\text{ex}}$  and Thouless energy  $E_c \equiv D/L^2$ .  $D$  is the diffusion constant of conduction electrons. We assume that it is the same in nonmagnetic and ferromagnetic layers.

In the case of small thickness, when  $E_c > \epsilon_{\text{ex}}$ , the coupling between ferromagnetic layers has a bilinear form, and the coupling energy per unit area is

$$\Omega(\varphi) = -\frac{F}{8(4\pi L)^2 E_c} \epsilon_{\text{ex}}^2 \cos \varphi. \quad (3)$$

Here,  $F$  is a characteristic constant of interaction in the diffusion channel [11]. It is positive for the Coulomb repulsion between electrons. Let us note that, in this regime, coupling (3) does not depend on  $L$ . The minimum of (3) corresponds to ferromagnetic orientation of the magnetizations in multilayer  $\varphi = 0$ . Note that the result is obtained in the limit when  $L > l$  or  $\epsilon_{\text{ex}}$  is smaller than the inverse mean free time  $D/l^2$ .

At the larger distance  $L$ , when  $E_c < \epsilon_{\text{ex}}$ , the coupling has biquadratic form, and the coupling energy per unit area is

$$\Omega(\varphi) \approx \frac{F}{(4\pi L)^2} E_c \cos^2 \varphi. \quad (4)$$

This quantity decreases as  $L^{-4}$  with increasing distance. The minimum of coupling energy corresponds to the noncollinear state  $\varphi = \pi/2$ .

Both expressions are given for the case of infinite thickness of the ferromagnetic layers. Calculation shows that, in the case  $d > \sqrt{D/\epsilon_{\text{ex}}}$ , the coupling weakly depends on  $d$ .

Results (3) and (4) are valid at low temperature  $T$ , when  $L < \sqrt{D/T}$ . At larger temperature, coupling energy decreases exponentially as  $\exp(-\sqrt{(8\pi T/D)}L)$ .

Let us compare results (3) and (4) with biquadratic contribution due to the mesoscopic fluctuations of

RKKY interaction [10], which is  $J_2 \sim \frac{1}{L^2 Ad} \frac{E_c^2}{E_c}$  at  $E_c < \epsilon_{\text{ex}}$  and

$$J_2 \sim \frac{1}{L^2 Ad} \frac{\epsilon_{\text{ex}}^3}{E_c} \text{ at } E_c > \epsilon_{\text{ex}}.$$

Here,  $A$  is an intralayer ferromagnetic stiffness and thickness  $d > \sqrt{D/\epsilon_{\text{ex}}}$ .

The quantity  $J_2$  decreases with  $L$  much faster than (4). Also, for  $\epsilon_{\text{ex}}/Ad \ll 1$ ,  $F \approx 1$ , the coupling energy given by expressions (3) and (4) is larger than the biquadratic contribution due to the mesoscopic fluctuations of RKKY in the whole range of distance. In this case, with increasing distance  $L \gg l$ , the system undergoes the transition between the ferromagnetic and noncollinear  $\varphi = \pi/2$  ordering. Such transition was observed in [12].

**2. Results.** The correction to thermodynamic potential which depends on  $\epsilon_{\text{ex}} \mathbf{n}(z)$  is given by the expression [11]

$$\begin{aligned} \Omega(\varphi) = & \frac{F}{4} T \sum_{|\omega_n \tau| < 1: \alpha, \beta} |\omega_n| \int \frac{d^2 \mathbf{q}}{(2\pi)^2} \\ & \times \int_{|z| < L/2} dz D_{\beta\beta}^{\alpha\alpha}(z, z, \mathbf{q}, \omega_n). \end{aligned} \quad (5)$$

Here, constant  $F$  describes the screened Coulomb interaction in diffusion channel,  $\omega_n = 2\pi n T$  is Matsubara frequency,  $\tau$  is the electron mean free time. The diffusion ladder satisfies the equation

$$\begin{aligned} & \left( -D \frac{d^2}{dz^2} + Dq^2 + |\omega_n| \right) D_{\mu\eta}^{\alpha\beta} \\ & + i\epsilon_{\text{ex}} \mathbf{n}(z) (\sigma_{\alpha\gamma} D_{\mu\eta}^{\gamma\beta} - D_{\mu\gamma}^{\alpha\beta} \sigma_{\gamma\eta}) \text{sgn } \omega_n \\ & = \delta(z - z') \delta_{\alpha\beta} \delta_{\mu\eta}. \end{aligned} \quad (6)$$

It is convenient to present the solution of equation (6) at  $|z| < L/2$  in the form

$$\begin{aligned} D_{\mu\eta}^{\alpha\beta} = & A_{\mu\eta}^{\alpha\beta} \exp(-Qz) + U_{\alpha\gamma}^+ C_{\mu\gamma}^{\gamma\beta} U_{\gamma\eta} \exp(Qz) \\ & + \frac{\exp(-Q|z - z'|)}{2DQ} \delta_{\alpha\beta} \delta_{\mu\eta}. \end{aligned} \quad (7)$$

Here, we introduce  $Q = \sqrt{q^2 + |\omega_n|/D}$ ;  $U$  is the matrix of the relative rotation of the magnetizations of ferromagnetic layers. In the case when the direction of the magnetization in the ferromagnetic layer  $z < -L/2$  is directed along the  $z$  axes  $\mathbf{n}(z) = (0, 0, 1)$  and at  $z > L/2$  direction is  $\mathbf{n}(z) = (\sin \varphi, 0, \cos \varphi)$ , it is the matrix of the rotation along the  $y$  axes  $U = \exp(i\varphi \sigma_y/2)$ .

For simplicity, we consider the limit of the semi-infinite ferromagnetic layers. More detailed consider-

ation shows that at  $d > \sqrt{D/\epsilon_{\text{ex}}}$ , the results weakly depend on the thickness of the ferromagnetic layers. It is convenient to introduce the boundary conditions for the diffusion ladder at ferromagnet–nonferromagnet interfaces taking into account the fact that, according to equation (6), in the coordinate system where spins are directed along the magnetization, components of the ladder with antiparallel spins decrease as  $\exp(-Q_1|z|)$  and  $\exp(-Q_1^*|z|)$  at  $|z| > L/2$ , where  $Q_1 = \sqrt{q^2 + (\omega + i\epsilon_{\text{ex}})/D}$ . The components of the ladder with parallel spins decrease as  $\exp(-Q|z|)$  at  $|z| > L/2$ . At  $z = -L/2$ , where  $\mathbf{n}(z) = (0, 0, 1)$ , the boundary conditions are

$$\begin{aligned} & \left(\frac{d}{dz} - Q_1\right) P_{\alpha\gamma}^+ D_{\mu\gamma}^{\gamma\beta} P_{\gamma\eta}^- \\ & = \left(\frac{d}{dz} - Q_1^*\right) P_{\alpha\gamma}^- D_{\mu\gamma}^{\gamma\beta} P_{\gamma\eta}^+ = 0, \\ & \left(\frac{d}{dz} - Q\right) P_{\alpha\gamma}^\pm D_{\mu\gamma}^{\gamma\beta} P_{\gamma\eta}^\pm = 0. \end{aligned} \quad (8)$$

Here, we introduce projectors of the spins on  $z$  axes  $P_\pm = (1 \pm \sigma_z)/2$ .

The same kind of boundary conditions can be introduced for the rotated diffusion ladder  $U_{\alpha\gamma} D_{\mu\gamma}^{\gamma\beta} U_{\gamma\eta}^+$  at  $z = L/2$ . Solving the system of Eqs. (6), (8), we obtain

$$\begin{aligned} \Omega(\varphi) = & -\frac{F}{2} T \sum_{|\omega_n, \tau| < 1} |\omega_n| \int \frac{d^2 \mathbf{q}}{(2\pi)^2} \frac{L}{DQ} \\ & \times \frac{\left[ (|\Lambda|^2 - (\text{Re}\Lambda)^2) \cos \varphi + \left( |\Lambda|^4 - \frac{1}{2} (\text{Re}\Lambda)^2 \right) \cos^2 \varphi - \frac{1}{2} (\text{Re}\Lambda)^2 + \text{Re}\Lambda \left( 1 - \frac{1}{2} |\Lambda|^2 - \frac{1}{2} |\Lambda|^2 \cos^2 \varphi \right) \frac{\sinh QL}{QL} \right]}{[1 - (\text{Re}\Lambda)^2 + 2(|\Lambda|^2 - (\text{Re}\Lambda)^2) \cos \varphi + (|\Lambda|^4 - (\text{Re}\Lambda)^2) \cos^2 \varphi]}. \end{aligned} \quad (9)$$

Here,  $\Lambda = [(Q_1 - Q)/(Q_1 + Q)] \exp(-QL)$ . Expression (9) contains the divergent terms, which do not depend on  $\varphi$  and must be subtracted.

In the limit of large exchange splitting, when  $|Q_1| > Q$ , the parameter  $\Lambda = \exp(-QL)$  is real. In this case, the energy is a function of  $\cos^2 \varphi$ . Subtracting in expression (9) terms which do not depend on the angle, we obtain

$$\begin{aligned} \Omega(\varphi) = & \frac{F}{4} T \sum_{|\omega_n, \tau| < 1; \alpha, \beta} |\omega_n| \\ & \times \int \frac{d^2 \mathbf{q}}{(2\pi)^2} \frac{L \left( 1 - \Lambda \frac{\sinh QL}{QL} \right)}{DQ} \frac{\Lambda^2 \cos^2 \varphi}{(1 - \Lambda^2 \cos^2 \varphi)}. \end{aligned} \quad (10)$$

The main contribution in expression (10) is from the region where  $\Lambda < 1$ . The denominator therefore gives only a small correction. Neglecting it, we obtain the expression (4).

In the opposite limit of the small exchange splitting  $\text{Re}\Lambda \sim \epsilon_{\text{ex}}^2$ ,  $|\Lambda| \sim \epsilon_{\text{ex}}$  and, to the order  $\epsilon_{\text{ex}}^2$ , the coupling energy is proportional to  $\cos \varphi$

$$\Omega(\varphi) = -\frac{F}{2} T \sum_{|\omega_n, \tau| < 1; \alpha, \beta} |\omega_n| \int \frac{d^2 \mathbf{q}}{(2\pi)^2} \frac{L|\Lambda|^2}{DQ} \cos \varphi. \quad (11)$$

Calculating (11) at zero temperature, we obtain (3). The transition between the limits (10) and (11) occurs at  $\epsilon_{\text{ex}} \sim D/L^2$ .

This work was supported by the Russian Foundation for Basic Research, project no. 01-02-17794.

## REFERENCES

1. M. Baibich, J. M. Broto, A. Fert, *et al.*, Phys. Rev. Lett. **61**, 2472 (1988).
2. S. S. P. Parkin, N. More, and K. P. Roche, Phys. Rev. Lett. **64**, 2304 (1990); **66**, 2152 (1991).
3. P. Levy, S. Zang, and A. Fert, Phys. Rev. Lett. **65**, 1643 (1990).
4. Q. Yang, P. Holody, S.-F. Lee, *et al.*, Phys. Rev. Lett. **72**, 3274 (1994).
5. B. Heinrich and J. F. Cochran, Adv. Phys. **42**, 523 (1993).
6. Y. Yafet, J. Appl. Phys. **61**, 4058 (1997).
7. J. C. Slonczewski, J. Appl. Phys. **73**, 5957 (1993); J. Magn. Magn. Mater. **150**, 13 (1995).
8. P. de Gennes, J. Phys. Radium **23**, 230 (1962).
9. A. Yu. Zyuzin and B. Spivak, Pis'ma Zh. Éksp. Teor. Fiz. **43**, 185 (1986) [JETP Lett. **43**, 234 (1986)].
10. A. Yu. Zyuzin, B. Z. Spivak, I. Vagner, and P. Wyder, Phys. Rev. B **62**, 13899 (2000).
11. B. L. Altshuler, A. G. Aronov, and A. Yu. Zyuzin, Zh. Éksp. Teor. Fiz. **84**, 1525 (1983) [Sov. Phys. JETP **57**, 889 (1983)].
12. P. Fuchs, U. Ramsperger, A. Vaterlaus, and M. Landolt, Phys. Rev. B **55**, 12546 (1997).

# Polar Smectic Subphases: Phase Diagrams, Structures and X-ray Scattering<sup>¶</sup>

P. V. Dolganov<sup>1</sup>, V. M. Zhilin<sup>1</sup>, V. E. Dmitrienko<sup>2</sup>, and E. I. Kats<sup>3</sup>

<sup>1</sup> Institute of Solid State Physics, Russian Academy of Sciences, Chernogolovka, Moscow region, 142432 Russia

<sup>2</sup> Shubnikov Institute of Crystallography, Moscow, 119333 Russia

<sup>3</sup> Laue-Langevin Institute, F-38042 Grenoble, France; Landau Institute for Theoretical Physics, Russian Academy of Sciences, Moscow, 117334 Russia

Received September 16, 2002

We analyze a discrete phenomenological model accounting for phase transitions and structures of polar Smectic- $C^*$  liquid-crystalline phases. The model predicts a sequence of phases observed in experiment: antiferroelectric  $SmC_A^*$ –ferrielectric  $SmC_{F11}^*$ –antiferroelectric  $SmC_{F12}^*$  (three- and four-layer periodic, respectively)–incommensurate  $SmC_\alpha^*$ – $SmA$ . We find that, in the three-layer  $SmC_{F11}^*$  structure, both the phase and the module of the order parameter (tilt angle) differ in smectic layers. This modulation of the tilt angle (and therefore of the layer spacing  $d$ ) must lead to X-ray diffraction at the wave vectors  $Q_s = 2\pi s/d$  ( $s = n \pm 1/3$ ) even for the nonresonant scattering. © 2002 MAIK “Nauka/Interperiodica”.

PACS numbers: 61.30.Eb; 64.70.Md; 61.10.Eq

In recent years, the existence of a variety of dipolar Smectic  $C$  ( $SmC$ )-like phases in liquid crystals was established [1, 2]. Besides conventional ferroelectric  $SmC^*$  [3] and antiferroelectric  $SmC_A^*$  [1, 2] phases, at least three smectic subphases with polar ordering of layers were identified in liquid crystals [2], namely, the ferrielectric  $SmC_{F11}^*$ , antiferroelectric  $SmC_{F12}^*$ , and short-pitch incommensurate  $SmC_\alpha^*$  phases. Due to their unusual physical properties and structures, these subphases have attracted much attention of researchers. They have regained more attention after the pioneering work by Mach *et al.* [4] established that the subphases possess structures nontrivial for liquid crystals, which result from frustration.

In all types of  $SmC$  phases, the long molecular axes are tilted with respect to the layer normal  $z$  by an angle  $\theta$ . In the ferroelectric  $SmC^*$  phase, the azimuthal orientation of molecules, described by an angle  $\varphi$ , is practically the same in neighboring  $i$ th and  $i + 1$ th layers (synclinal ordering,  $\Delta\varphi = \varphi_{i+1} - \varphi_i \approx 0$ ). The direction of polarization is perpendicular to the tilt plane. In the antiferroelectric  $SmC_A^*$  phase, the directions of molecular tilt in adjacent layers are nearly opposite (anticlinal ordering,  $\Delta\varphi \approx \pi$ ). Orientational ordering in tilted smectic structures can be described by a two-dimensional vector  $\xi$ , which is the projection of the nematic director  $\mathbf{n}$  onto the layer plane. The angles  $\theta$  and  $\varphi$  may be referred to as the modulus and the phase of the two-component order parameter. Resonant X-ray scattering

measurements showed that the  $SmC_{F11}^*$  and  $SmC_{F12}^*$  phases possess periodic structures with a three-layer and a four-layer unit cell, respectively [4–6]. The short-pitch modulation of the  $SmC_\alpha^*$  phase, which, in different compounds, ranges from 5 to about 30 smectic layers, is incommensurate with the layer ordering. This almost unambiguously indicates that the interlayer structure represents a short-pitch helix. A complete and unifying description of azimuthal ordering in the  $SmC_{F11}^*$  and the  $SmC_{F12}^*$  phases is not yet available. In X-ray experiments, the appearance of resonant peaks at  $Q_z = Q_0(n + m/3)$  in the  $SmC_{F11}^*$  and  $Q_z = Q_0(n + m/4)$  in the  $SmC_{F12}^*$  ( $n$  and  $m$  are integers,  $Q_0 = 2\pi/d$ , where  $d$  is the layer spacing) and the polarization scattering character are associated with the nonplanar structure of these phases, i.e., with a change in phase of order parameter in adjacent layers. Molecular arrangement is represented by distorted planar structure [7–9] with the out-of-plane molecular distortion angle in the region from about  $5^\circ$  to  $28^\circ$ .

Several models have been proposed for the structures of the subphases [2, 10–14]. Recently, the most widely used was the so-called ANNNIXY model [14–20] (also called the “clock” model [18, 19]). In this Landau-like approach, smectic phases are modeled as a stack of layers with the two-component order parameter  $\xi$ , which is uniform within the plane ( $XY$ ) of each layer. Frustrating antiferroelectric (A) interaction (I) is introduced between the next-nearest neighbor (NNN) layers. The model predicts the formation of the short-

<sup>¶</sup>This article was submitted by the authors in English.

pitch ( $\text{Sm}C_\alpha^*$ ) phase, three-layer, and four-layer structures.

However, in spite of substantial progress in experimental and theoretical investigations, a fundamental understanding of the most striking features of the subphases is still lacking. X-ray data obtained up to the present time do not allow one to unambiguously describe the azimuthal molecular ordering. In particular, the conclusion about the orientation of the tilt planes in cells was made only on the basis of optical data [7–9]. The theory predicts a principal possibility for subphase formation but not their exact structure and sequence. At least in part this is due to the fact that most of the previous calculations were conducted under very simplifying assumptions (like  $\theta \equiv \text{const}$  in different layers).

We go one step further in this work and provide precise and detailed description of subphase structures and phase diagrams. In the framework of the ANNNIXY model, we obtained a temperature sequence of subphases which is actually observed in experiment. We find that, in the three-layer structure, not only the phase  $\varphi$  but also the module  $\theta$  of the order parameter is non-uniform in a unit cell. This leads in particular to a different layer thickness in a cell. We believe we are the first to suggest a different layer thickness. This issue, surprisingly, does not appear to have been examined in any generality before. Our conclusion about the variation of  $\theta$  and  $d$  in a unit cell is based on the minimization of the free energy in different layers over both the phase and the module of the order parameter. Nonuniformity of  $\theta$  and  $d$  in the three-layer structure should lead to nonresonant X-ray diffraction peaks which are related neither to the order parameter phase dependence on  $\mathbf{z}$  nor to the tensorial character of the structural factor, and this prediction is the main message of our publication.

The free energy of our version of the ANNNIXY model can be written as an expansion over the structure order parameter  $\xi_i$ . Taking into account nearest-neighbor (NN) and NNN interactions [16–18], we come to

$$F_0 = F_1 + F_2 + F_3, \quad (1)$$

where

$$F_1 = \sum_i \left[ \frac{1}{2} a_0 \xi_i^2 + \frac{1}{4} b_0 \xi_i^4 + \frac{1}{8} a_2 \xi_i \xi_{i+2} \right], \quad (2)$$

$$F_2 = b_1 \sum_i \xi_i^2 (\xi_{i-1} \xi_i + \xi_i \xi_{i+1}), \quad (3)$$

and

$$F_3 = \frac{1}{2} a_1 \sum_i \xi_i \xi_{i+1}. \quad (4)$$

In Eq. (2),  $a_0 = \alpha(T - T^*)$  and  $b_0$  are Landau coefficients describing the SmA to SmC transition in isolated layers, and  $F_2$  and  $F_3$  describe the coupling between the neighboring layers. The last term in Eq. (2) can lead to frustration of synclinic and anticlinic homogeneous ordering in the system, since at  $a_2 > 0$  it favors anticlinic orientation in the next-nearest layers, which is incompatible with the homogenous structures. Large  $a_2$  results in the formation of compromise-commensurate ( $\text{Sm}C_{F11}^*$  and  $\text{Sm}C_{F12}^*$ ) or incommensurate ( $\text{Sm}C_\alpha^*$ ) structures releasing frustrations.

In our calculations, we also introduced one new term in the free-energy expansion

$$F_4 = a_3 \sum_i [\xi_i \times \xi_{i+1}]^2, \quad (5)$$

providing a certain energetic barrier for azimuthal reorientation of molecules between synclinic and anticlinic structures.

Since the subphases are observed in compounds with chiral molecules, we should account for chiral interactions, which can be presented in the free energy by

$$F_5 = f \sum_i [\xi_i \times \xi_{i+1}]_z \quad (6)$$

(so-called Lifshits term).

Now we are in a position to determine all possible stable or metastable phases (and phase transitions between them) performing the free-energy (1)–(6) minimization with respect to the phase and to the module of the order parameter. A more detailed description of the minimization procedure will be given elsewhere [21].

Further, we will set  $b_0 = 1$ , thus measuring  $\alpha$  in units 1/K, keeping all other coefficients dimensionless. The value of  $\alpha$  was chosen to give  $\theta$  at  $T = 10$  K lower the phase transition from SmA to the tilted phase a typical for liquid crystals value about 0.35 rad ( $20^\circ$ ). The coefficient  $a_2$  was taken positive, as subphases appear in the presence of frustration, i.e., at  $a_2 > 0$ . The other terms in the free energy will be introduced successively to show more clearly which effects are caused by each of the terms.

The starting of our calculations is the first two terms in the free-energy expansion (1)–(6), i.e.,  $F = F_1 + F_2$ , which is the simplest form describing  $\text{Sm}C_\alpha^*$  and the SmC or the  $\text{Sm}C_A$  phases. In the following we shall also be interested in  $\text{Sm}C_{F11}^*$  and  $\text{Sm}C_{F12}^*$  subphases emerging above the antiferroelectric  $\text{Sm}C_A^*$  phase, thus the sign of  $b_1$  was taken positive. Figure 1 shows the phase diagram in coordinates  $T$  and  $b_1/a_2$ . The temperature was counted from the transition from SmA to the tilted phase (closed diamonds, straight line). The diagram was calculated for different values of frustration, i.e., parameter  $a_2$ . Closed squares in the figure correspond to

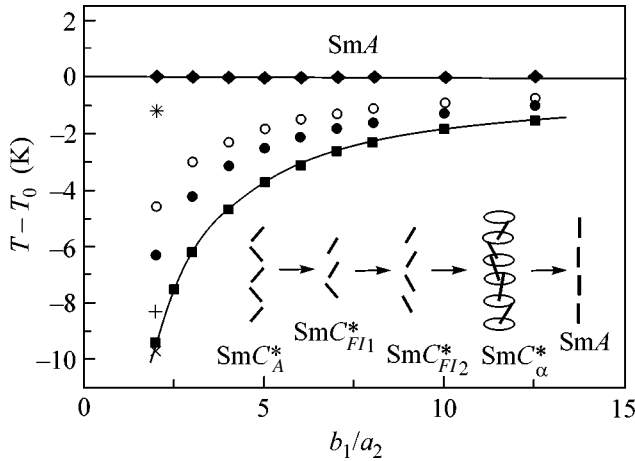


**Fig. 1.** Phase diagram plotted as  $T - T_0$  versus  $b_1/a_2$ .  $T_0$  is the transition temperature from SmA to tilted phases (closed diamonds, straight line). Closed squares represent the phase diagram for the free energy  $F = F_1 + F_2$ , closed and open circles, for  $F = F_1 + F_2 + F_4$ . Crosses ( $\times$ ,  $+$ ) and a star ( $*$ ) show the transition temperatures at  $b_1/a_2$  for  $F = F_1 + F_2 + F_3 + F_4$  (see text). The set of model parameters is  $\alpha = 0.01 \text{ K}^{-1}$ ,  $b_1 = 0.04$ ,  $a_1 = -0.006$ ,  $a_2 = 0.02$ ,  $a_3 = 0.02$ .

the diagram for the free energy  $F = F_1 + F_2$ . The region between the two lines is occupied by the  $\text{SmC}_{\alpha}^*$  phase. Thus, in this case, we get the following phase sequence  $\text{SmC}_A - \text{SmC}_{\alpha}^* - \text{SmA}$ . Increase of frustration leads to broadening of the  $\text{SmC}_{\alpha}^*$  phase temperature interval. Addition of  $F_4$  term to the free energy leads to suppression of the short-pitch helix and to formation of commensurate 3-layer and 4-layer periodic structures. Closed and open circles represent the phase diagram for the free energy  $F = F_1 + F_2 + F_4$ . The temperature sequence of phases is  $\text{SmC}_A - \text{SmC}_{FI1} - \text{SmC}_{FI2} - \text{SmA}$ . Transition temperatures  $\text{SmC}_A - \text{SmC}_{FI1}$  and  $\text{SmC}_{FI1} - \text{SmC}_{FI2}$  are represented in the diagram by closed and open circles.

Including the  $F_3$  term into the free energy (i.e., we are treating now the free energy  $F = F_1 + F_2 + F_3 + F_4$ ) leads to formation of short-pitch helix ordering near the SmA phase. For the ratio  $b_1/a_2 = 2$ , the phase-transition temperatures are denoted by crosses and a star ( $\times$ ,  $+$ ,  $*$ ). The phase sequence is  $\text{SmC}_A - \text{SmC}_{FI1} - \text{SmC}_{FI2} - \text{SmC}_{\alpha}^* - \text{SmA}$ . A schematic representation of structures is given in the lower part of Fig. 1. The temperature dependence of the cell parameter is presented in Fig. 2. The width of subphases and the value and temperature dependence of the  $\text{SmC}_{\alpha}^*$  pitch (increase or decrease with temperature) depend on the value of  $a_1$ . Moreover, in a certain region of parameters, SmC structure may appear in the temperature window between the  $\text{SmC}_{FI2}^*$  and SmA phases. Neglecting chiral contributions  $\text{SmC}_{FI1}^*$  and  $\text{SmC}_{FI2}^*$  structures would be planar. Lifshits term (6) leads to two effects: the molecular tilt

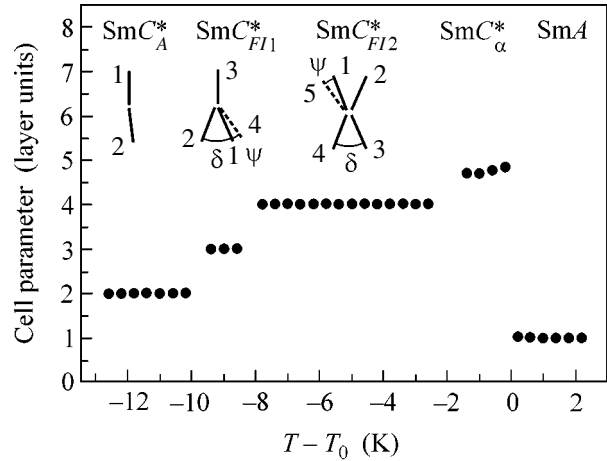


**Fig. 2.** Cell parameters versus temperature:  $\text{SmC}_A^*$ ,  $\text{SmC}_{FI1}^*$ ,  $\text{SmC}_{FI2}^*$ ,  $\text{SmC}_{\alpha}^*$  (incommensurate), SmA. A schematic representation of tilt orientations in different subphases (view along the  $z$  axis) is given in the upper part of the figure. Numbers (1, 2, 3, ...) denote subsequent layers. The set of model parameters is as in Fig. 1.

directions become nonplanar (distortion angle  $\delta$ ), and cells mutually rotate relative to each other (angle  $\psi$ , Fig. 2). This rotation of the cells around the  $z$  direction may also be regarded as a manifestation of a long-pitch helix structure or a small difference of cell parameters from 3 and 4 layer spacings. The magnitudes of  $\delta$  and  $\psi$  depend on the chirality coefficient. Upon introducing even a relatively small chirality, when the pitch of macroscopic helix is more than 100 layer spacings, the distortion angle may be fairly large (about  $35^\circ$  in the  $\text{SmC}_{FI1}^*$ ). This non-trivial behavior is related to a very peculiar “interference” phenomenon between frustration and chirality actions leading to an enhancement of the chiral contribution effect and inducing an opposite molecular rotation for adjacent synclinic and anticlinic pairs. On the phase diagram presented in Fig. 1 along the temperature path, three subphases appear in the exact sequence observed in a classical antiferroelectric liquid crystal MHPOBC in samples with high optical purity [22].

One more substantial result which emerges from our calculations is a difference in values of  $\theta_i$  in different layers of the 3-layer  $\text{SmC}_{FI1}^*$  subphase cell. We found that the order-parameter module  $\theta$  is larger in the layer which has anticlinic orientation with both nearest neighbors (the layer denoted as 3 in Figs. 2, 3). The difference  $\Delta\theta = \theta_3 - \theta_{1,2}$  is about 13–15% for the planar structure. Chirality (and the distortion induced by it) decreases this difference (for  $\delta \approx 35^\circ$ ,  $\Delta\theta$  may change from about 14% to 12%). Thus, in this 3-layer cell structure, the layers differ not only by the phase  $\varphi$  but also by the module  $\theta$  of the order parameter. It is worth noting that, in spite of the fact that this possibility stems

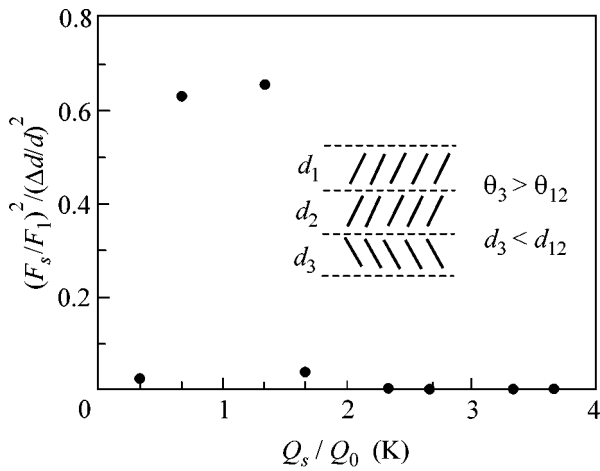


**Fig. 3.** Relative intensities of the satellite peaks calculated from Eq. (7). The insertion shows schematic representation of a three-layer cell of the  $\text{Sm}C_{F11}^*$  structure.  $\theta_i$  is the tilt angle,  $d_i$ , the thickness of the  $i$ th layer.

directly from the symmetry of the  $\text{Sm}C_{F11}^*$  unit cell, it was overlooked in previous studies. In any case, the difference in  $\theta_i$  should lead to the modulation of the layer thickness (Fig. 3). Using the relation  $d_i = d_0 \cos \theta_i$ , we found that, depending on the absolute value of  $\theta_i$ , the modulation of  $d_i$  along  $\mathbf{z}$  should result in one-third satellites to the main diffraction peaks even for non-resonant diffraction (i.e., far from any absorption edges).

In the model with sinusoidal electron density of smectic layers, the ratio of the satellite Fourier harmonic of electron density with  $Q_s = sQ_1$  ( $s = n \pm 1/3$ ) to the main harmonic with  $Q_1 = 2\pi/\bar{d}$  is found to be

$$\frac{F_s}{F_1} = -\frac{1}{9} \frac{\Delta d}{\bar{d}} \int_{-\pi}^{5\pi} \epsilon \sin x \cos(sx) dx, \quad (7)$$

where  $\bar{d} = (2d_{12} + d_3)/3$  is the average layer spacing,  $\Delta d = d_{12} - d_3$ ,  $\epsilon = 2x$  if  $-\pi < x < \pi$ , and  $\epsilon = -x + 3\pi$  if  $\pi < x < 5\pi$ . The calculated square of the ratio which characterizes the relative intensities of the satellite reflections is shown in Fig. 3 (notice the large value of two satellites of the main reflection). The observation of the one-third satellite peaks, not related to the tensorial character of the scattering structure factor, would be a direct signature of the modulation of  $d_i$ .

To conclude, we established that our phenomenological model (without invoking additional mechanisms) can reproduce the sequence of the subphases observed in experiment. Additionally, we found that molecular orientations in adjacent layers in the  $\text{Sm}C_{F11}^*$  and  $\text{Sm}C_{F12}^*$  structures essentially differ. While in the  $\text{Sm}C_{F12}^*$ , only the phase of the order parameter

changes, in the three-layer  $\text{Sm}C_{F11}^*$  subphase, both the phase and the module of the order parameter are varied from layer to layer. The latter must lead to non-resonant X-ray diffraction at multiples  $s = n \pm 1/3$  of the wave vector  $Q_1 = 2\pi/\bar{d}$ . We anticipate that the effects we found will be observable and that understanding of the underlying mechanisms will be essential to gain further insight into the nature of polar chiral smectic liquid crystals.

This study was supported by the Russian Foundation for Basic Research, project no. 01-02-16507.

## REFERENCES

1. A. D. L. Chandani, E. Gorecka, Y. Ouchi, *et al.*, Jpn. J. Appl. Phys., Part 2 **28**, L1265 (1989).
2. A. Fukuda, Y. Takanishi, T. Isozaki, *et al.*, J. Mater. Chem. **4**, 997 (1994).
3. R. B. Meyer, L. Liébert, L. Strzelecki, and P. Keller, J. Phys. Lett. **36**, L69 (1975).
4. P. Mach, R. Pindak, A.-M. Levelut, *et al.*, Phys. Rev. Lett. **81**, 1015 (1998).
5. P. Mach, R. Pindak, A.-M. Levelut, *et al.*, Phys. Rev. E **60**, 6793 (1999).
6. L. S. Hirst, S. J. Watson, H. F. Gleeson, *et al.*, Phys. Rev. E **65**, 041705 (2002).
7. P. M. Johnson, S. Pankrats, P. Mach, *et al.*, Phys. Rev. Lett. **83**, 4073 (1999).
8. D. Schlauf, Ch. Bahr, and H. T. Nguyen, Phys. Rev. E **60**, 6816 (1999).
9. D. A. Olson, S. Pankratz, P. M. Johnson, *et al.*, Phys. Rev. E **63**, 061711 (2001).
10. Y. Takanishi, K. Hiraoka, V. Agrawal, *et al.*, Jpn. J. Appl. Phys. **30**, 2023 (1991).
11. T. Isozaki, T. Fujikawa, H. Takezoe, *et al.*, Phys. Rev. B **48**, 13439 (1993).
12. S. A. Pikin, S. Hiller, and W. Haase, Mol. Cryst. Liq. Cryst. **262**, 425 (1995).
13. M. Gorkunov, S. Pikin, and W. Haase, Pis'ma Zh. Éksp. Teor. Fiz. **72**, 81 (2000) [JETP Lett. **72**, 57 (2000)].
14. M. Čepič and B. Žekš, Mol. Cryst. Liq. Cryst. Sci. Technol., Sect. A **263**, 61 (1995).
15. A. Roy and N. V. Madhusudana, Europhys. Lett. **36**, 221 (1996).
16. B. Rovšek, M. Čepič, and B. Žekš, Phys. Rev. E **54**, R3113 (1996).
17. A. Roy and N. V. Mathusudana, Europhys. Lett. **41**, 501 (1998).
18. B. Rovšek, M. Čepič, and B. Žekš, Phys. Rev. E **62**, 3758 (2000).
19. M. Čepič and B. Žekš, Phys. Rev. Lett. **87**, 085501 (2001).
20. D. A. Olson, X. F. Han, A. Cady, and C. C. Huang, Phys. Rev. E **66**, 021702 (2002).
21. P. V. Dolganov, V. M. Zhilin, V. K. Dolganov, and E. I. Kats, Phys. Rev. E (in press).
22. E. Gorecka, D. Pocięcha, M. Čepič, *et al.*, Phys. Rev. E **65**, 061703 (2002).

# Anisotropic Spin Diffusion in a Semiconductor Quantum Well<sup>¶</sup>

V. N. Gridnev

*Ioffe Physicotechnical Institute, Russian Academy of Sciences, St. Petersburg, 194021 Russia*

*e-mail: gridnev@mail.ioffe.ru*

Received September 16, 2002

We show that spin diffusion of an inhomogeneous spin-density distribution in an asymmetric zinc-blende semiconductor quantum well is anisotropic in coordinate space, if the D'yakonov–Perel' spin-relaxation mechanism is dominant. This anisotropy depends on the relation between the Dresselhaus and Rashba contributions to the spin splitting and reaches its maximum when both contributions are equal in magnitude. Under this condition, the temporal behavior of spin density strongly depends on the relation between the initial spatial extent of the spin packet and spin diffusion length. © 2002 MAIK “Nauka/Interperiodica”.

PACS numbers: 73.21.Fg; 75.40.Gb

The temporal and spatial evolution of an inhomogeneous spin polarization in semiconductor quantum well (QW) and heterostructures has attracted much attention in recent years in connection with the possible use of the spin degrees of freedom in spintronics [1]. It is known that, in  $A_3B_5$  semiconductors, even for the homogeneous spin polarization, there are correlations between the motion of electrons in the coordinate and spin spaces [2–4]. These correlations are a consequence of the linear (in 2D structures) dependence of the spin-orbit interaction (SOI) on the electron momentum  $\mathbf{k}$ . The SOI is also an essential ingredient of the D'yakonov–Perel' (DP) spin-relaxation mechanism [5], which is dominant in most  $A_3B_5$  bulk semiconductors and heterostructures.

It is well known that in a zinc-blende semiconductor QW, there are two contributions to the SOI. The first of them arises due to the bulk inversion asymmetry of the material ( $V_{BIA}$ ) and induces the Dresselhaus spin splitting [6, 7], while the second is caused by the structure inversion asymmetry of the QW itself ( $V_{SIA}$ ) and leads to the Rashba spin splitting [8].  $V_{BIA}$  is fixed by the choice of material of which the QW is made, but  $V_{SIA}$  can be modified by the application of a gate voltage.

In this paper, we point to a new phenomenon, which is due to the interference of  $V_{BIA}$  and  $V_{SIA}$ . First, we show that in the case when the DP spin-relaxation mechanism is dominant, the interference of  $V_{BIA}$  and  $V_{SIA}$  leads to an anisotropy (in the coordinate space) of the inhomogeneous spin distribution in the QW plane. Second, we show that the simultaneous presence of  $V_{BIA}$  and  $V_{SIA}$  leads to a non-exponential relaxation of the spin density. To this end, we solve the diffusion equa-

tion for the spin density  $\mathbf{M}(\mathbf{r}, t)$  assuming that the initial spin distribution is created by a short laser pulse, focused to a spot with a diameter much less than the spin diffusion length  $L_s$ . This condition can be satisfied in the case of an  $n$ -doped semiconductor in which the electron spin-relaxation times are relatively long and the spin diffusion rates are relatively high [9, 10].

We want to emphasize that, in the case of homogeneous spin polarization and in the absence of the magnetic field,  $V_{BIA}$  and  $V_{SIA}$  give additive contributions to the DP relaxation rate  $1/\tau_s$  of the spin polarization initially oriented perpendicularly to the QW [3]; that is,  $1/\tau_s$  is not sensitive to the relation between  $V_{BIA}$  and  $V_{SIA}$ . In the external magnetic field  $\mathbf{B}$ , the contributions of  $V_{BIA}$  and  $V_{SIA}$  to the spin relaxation become non-additive [11, 12], but the relaxation still remains exponential.

Note that spin diffusion in a semiconductor QW provided that the DP spin relaxation mechanism is dominant has been considered theoretically in [13]. However, only the  $V_{SIA}$  contribution to the SOI was taken into account in the calculation of the spin distribution, which is inevitably isotropic in the coordinate space in that case, if  $B = 0$ . The goal of our consideration is different. We want to demonstrate that the interplay between  $V_{BIA}$  and  $V_{SIA}$  leads to a dependence of the spin density  $\mathbf{M}(\mathbf{r}, t)$  on the direction of  $\mathbf{r}$  even in the absence of the external magnetic field.

The spin-orbit part of the electron Hamiltonian  $V_{so}$  has the form

$$V_{so} = V_{BIA} + V_{SIA} = \frac{\hbar}{2}\Omega(\mathbf{k})\sigma, \quad (1)$$

where  $\mathbf{k}$  is the electron wave vector in the QW plane,  $\sigma = \{\sigma_x, \sigma_y, \sigma_z\}$  are the Pauli matrices, and  $\Omega(\mathbf{k})$  can be

<sup>¶</sup>This article was submitted by the author in English.

regarded as a  $\mathbf{k}$ -dependent effective magnetic field. In the following, we will consider (001) grown QW. In this case, the anisotropy of the spin diffusion is more pronounced and, at the same time, allows the most simple theoretical consideration. For a sufficiently narrow QW, one can neglect cubic in  $\mathbf{k}$  terms in  $\Omega(\mathbf{k})$  [7]. The vector  $\Omega(\mathbf{k})$  lies in the QW plane and its components are given by

$$\Omega(\mathbf{k}) = [(\alpha_1 k_x + \alpha_2 k_y), -(\alpha_1 k_y + \alpha_2 k_x)], \quad (2)$$

where the coefficients  $\alpha_1$  and  $\alpha_2$  correspond to  $V_{BIA}$  and  $V_{SIA}$ , respectively.

The diffusion equation for the spin density  $\mathbf{M}(\mathbf{r}, t)$  has been presented in [13, 14]. Here we only discuss the applicability of the diffusion approximation to our problem. The diffusion approximation is applicable if  $\tau v_f/a$ ,  $\tau\Omega \ll 1$ , where  $\tau$  is the mean scattering time,  $a$  is the size of the spin packet, and  $v_f$  is the Fermi velocity. These inequalities mean that the motions in the coordinate and spin spaces, consequently, are diffusive. To give a more quantitative insight into the applicability of the diffusive approximation for a GaAs-based QW, we take a typical value of the Fermi wave vector  $k_f = 10^{-6} \text{ cm}^{-1}$ , which corresponds to the sheet electron density  $N = k_f^2/2\pi \approx 2 \times 10^{11} \text{ cm}^{-2}$ , and the Fermi velocity  $v_f = \hbar k_f/m \approx 10^6 \text{ cm/s}$ , where  $m = 0.067m_e$  is the electron effective mass. As was recently clarified in [15], when considering the DP spin-relaxation mechanism, the mean scattering time  $\tau$  must be calculated taking into account electron-electron collisions. For this reason, in the case of an  $n$ -doped semiconductor,  $\tau$  can be approximately estimated as an optical dephasing time, measured in time-resolved four-wave-mixing experiments [16] in the spectral range of the interband transitions. This time is on the order of 0.1 ps, and there is no essential difference between the times in 2D and 3D systems [17]. If we take the lower bound for the spot size  $a = 1 \mu\text{m}$  (the spot size can not be made smaller than the laser wavelength) and the upper bound for the spin splitting  $\hbar\Omega = 1 \text{ meV}$  [18], we obtain  $\tau v_f/a \sim 10^{-3}$  and  $\tau\Omega \sim 10^{-1}$ . Thus, the diffusion approximation can be applied to our problem without any essential restrictions.

In an  $n$ -doped semiconductor, the excess of photo-excited electrons and holes rapidly disappears due to the recombination of holes with background electrons. In other words, only the spin packet but not the charge packet is present in the semiconductor [19]. This allows one to neglect the coupling between charge and spin degrees of freedom. Then, for the degenerate electron gas, the diffusion equation takes the form [13]

$$\begin{aligned} \frac{\partial \mathbf{M}(\mathbf{r}, t)}{\partial t} - [D\nabla_{\mathbf{r}}^2 + \hat{\Gamma}] \mathbf{M}(\mathbf{r}, t) \\ - [\mathbf{b}(\nabla_{\mathbf{r}}) + \Omega_L] \times \mathbf{M}(\mathbf{r}, t) = \mathbf{I}(\mathbf{r}, t), \end{aligned} \quad (3)$$

where  $D = \tau v_f^2/2$  is the diffusion constant,  $\Omega_L = g\mu_B \mathbf{B}/\hbar$  is the electron spin resonance frequency in a magnetic field  $\mathbf{B}$ ,  $\hat{\Gamma}$  is the tensor of the DP spin relaxation rates, and  $\mathbf{I}(\mathbf{r}, t) = [0, 0, I_z(\mathbf{r}, t)]$  is a source of spin-polarized electrons. The operator  $\mathbf{b} = \tau k_f v_f \Omega(\nabla_{\mathbf{r}})$  mixes different components of the inhomogeneous spin polarization  $\mathbf{M}(\mathbf{r}, t)$ . In accordance with the typical experimental conditions, we assume that the magnetic field is parallel to the QW plane and  $\tau\Omega_L \ll 1$ .

Following [13], we perform the Fourier transform of the spin density  $\mathbf{M}(\mathbf{r}, t)$  in Eq. (3). The algebraic equation for  $\mathbf{M}(\mathbf{q}, \omega)$  takes the form

$$\begin{aligned} (-i\omega + Dq^2 + \hat{\Gamma}) \mathbf{M} \\ + [\mathbf{b}(\mathbf{q}) + \Omega_L] \times \mathbf{M} = \mathbf{I}(\mathbf{q}, \omega). \end{aligned} \quad (4)$$

Since rather short ( $\sim 100$  fs) laser pulses are used now in experimental investigations of the spin dynamics, it is justified to take the delta-function-type approximation for the time dependence of the source term  $\mathbf{I}(\mathbf{r}, t)$  in Eq. (3). However, the same is not always true about the spatial dependence of the source term, since the diameter  $a$  of the laser spot and the spin diffusion length  $L_s$  may be comparable in magnitude. Moreover, it is interesting to trace the evolution of the main features of the spin diffusion when the ratio  $a/L_s$  varies from  $\ll 1$  to  $\gg 1$ . For this reason, we take the Gaussian distribution for the initial spin density:

$$I_z(\mathbf{r}, t) = \frac{M_0}{\pi a^2} \exp\left(-\frac{r^2}{a^2}\right) \delta(t), \quad (5)$$

$$I_z(\mathbf{q}, \omega) = M_0 \exp\left(-\frac{a^2 q^2}{4}\right). \quad (6)$$

Before solving Eqs. (3) and (4), we discuss their symmetry properties. First of all, we note that these equations are not invariant under the spatial inversion; that is,  $\mathbf{M}(\mathbf{r}, \mathbf{B}, t) \neq \mathbf{M}(-\mathbf{r}, \mathbf{B}, t)$ . However, since the laser source term possesses the symmetry  $I_z(\mathbf{r}, t) = I_z(-\mathbf{r}, t)$ , the solution of Eq. (3) obeys the exact relation

$$M_z(\mathbf{r}, \mathbf{B}, t) = M_z(-\mathbf{r}, -\mathbf{B}, t). \quad (7)$$

This relation is a special feature of an inhomogeneous spin distribution which varies with time under the DP spin relaxation mechanism.

Next we note that the tensor  $\hat{\Gamma}$  and the vector  $\Omega_L$  do not depend on  $\mathbf{q}$  and are unable to create the anisotropy in the coordinate space if  $\mathbf{b}(\mathbf{q}) = 0$ . Hence, the only source of the anisotropy is the vector  $\mathbf{b}(\mathbf{q})$ , which enters Eq. (4) through the quantity  $\mathbf{h} = \mathbf{b}(\mathbf{q}) + \Omega_L$ . In turn, the vector  $\mathbf{h}$  forms two independent invariants, namely,  $\mathbf{h}^2$  and  $h_i h_j \Gamma_{ij}$ , which depend on the direction of  $\mathbf{q}$  and determine the anisotropy of  $M_z(\mathbf{r}, t)$ . In the considered case of the DP spin-relaxation mechanism, these invariants have common microscopic origin. If only one con-

tribution to the SOI is nonzero ( $\alpha_1\alpha_2 = 0$ ), these invariants are equivalent, since the tensor  $\hat{\Gamma}$  is isotropic in the QW plane [11]. In this case, the anisotropy of the spin diffusion is entirely due to the external magnetic field, since  $|\mathbf{b}(\mathbf{q})|$  does not depend on the direction of  $\mathbf{q}$ . This situation has been analyzed in [13].

Here we want to analyze the intrinsic anisotropy of the spin diffusion which is due to the simultaneous presence of  $V_{BIA}$  and  $V_{SIA}$  and exists in the absence of the external magnetic field. To make the following consideration more transparent, we transform the in-plane coordinate system  $xy$  to a new coordinate system  $x'y'$ , where the  $x'$  and  $y'$  axes are oriented along  $[110]$  and  $[1\bar{1}0]$  directions, respectively. From Eq. (2) we find the components of the vector  $\Omega(\mathbf{k})$  in the new coordinate system:

$$\Omega_{x'} = (\alpha_2 - \alpha_1)k_{y'}, \quad (8)$$

$$\Omega_{y'} = -(\alpha_2 + \alpha_1)k_{x'}. \quad (9)$$

If  $V_{BIA}$  or  $V_{SIA}$  equals zero ( $\alpha_1\alpha_2 = 0$ ), the spin splitting is isotropic and, as a consequence, the diffusion is isotropic too. This case has been analyzed in [13]. In the opposite case of strong anisotropy ( $\alpha_1 = \pm\alpha_2$ ), the vector  $\Omega(\mathbf{k})$  is oriented along the  $[1\bar{1}0]$  or  $[110]$  directions, respectively.

Only numerical solution of Eq. (3) is possible in case of arbitrary relation, between  $\alpha_1$  and  $\alpha_2$ . Since our prime interest is in the anisotropy of the spin distribution, we consider the ultimate case  $\alpha_1 = \alpha_2$  when  $\Omega(\mathbf{k}) \parallel [1\bar{1}0]$  and the anisotropy becomes as large as possible. Fortunately, in this case, Eq. (3) has a simple analytical solution.

To solve Eqs. (3) and (4), we also need to know the components of the tensor  $\hat{\Gamma}$ . As shown in [11], when both  $V_{BIA}$  and  $V_{SIA}$  are nonzero, the tensor  $\hat{\Gamma}$  has one normal to the QW plane eigenvector with corresponding relaxation rate  $1/\tau_s = \tau k_f^2 (\alpha_2^2 + \alpha_1^2)$  and two in-plane eigenvectors oriented along the directions  $[110]$  and  $[1\bar{1}0]$ , with the relaxation rates  $1/\tau_{\pm} = \tau k_f^2 (\alpha_1 \pm \alpha_2)^2/2$ , respectively. Consequently, the anisotropy of the spin relaxation in the QW plane depends on the relation between  $V_{BIA}$  and  $V_{SIA}$ . Note that the spin relaxation anisotropy manifests itself only if the spin density  $\mathbf{M}$  is not orthogonal to the QW plane. Hence, it is not obvious that this in-plane anisotropy of the spin relaxation must necessarily lead to the anisotropy of the spin diffusion if the initially created spin density  $\mathbf{M}(\mathbf{r}, t = 0)$  is orthogonal to the QW plane.

Since we are interested in the intrinsic anisotropy of the spin distribution rather than one due to the external magnetic field, we consider only the special case when the magnetic field  $\mathbf{B} \parallel [1\bar{1}0]$ , that is, directed along

$\Omega(\mathbf{k})$ . In this case  $M_{y'} = 0$ , since both  $\mathbf{B}$  and  $\Omega(\mathbf{k})$  are directed along  $y'$  and unable to create  $M_{y'}$  if the initial spin polarization is oriented along  $z$ . Solving Eq. (4) for  $\mathbf{M}_z(\mathbf{q}, \omega)$  and performing the inverse Fourier transform, we obtain

$$M_z(\mathbf{r}, t) = \int \frac{d\mathbf{q}}{(2\pi)^2} I_z(\mathbf{q}) (e^{-\lambda_1(\mathbf{q})t} + e^{-\lambda_2(\mathbf{q})t}) e^{i\mathbf{q}\mathbf{r}}, \quad (10)$$

where  $\lambda_{1,2} = i\omega_{1,2}$  are the eigenvalues of Eq. (4)

$$\lambda_{1,2}(\mathbf{q}) = Dq^2 + \frac{1}{\tau_s} \pm 2\frac{L_s}{\tau_s} q_{x'} \pm i\Omega_L, \quad (11)$$

where  $L_s = \sqrt{D\tau_s}$ , is the spin diffusion length. Inserting the expression (6) for  $I_z(\mathbf{q})$  into the integrand of Eq. (10) and performing the integration, we get

$$M_z(\mathbf{r}, t) = \frac{M_0}{F} \exp\left(-\frac{r^2}{F} - \frac{t a^2}{\tau_s F}\right) \times \cos\left(4\frac{L_s t}{\tau_s F} x' - \Omega_L t\right), \quad (12)$$

where  $F = 4Dt + a^2$ . From this equation, we notice that the spin-density distribution  $M_z(\mathbf{r}, t)$  is anisotropic. The isotropic exponential decrease of  $M_z(\mathbf{r}, t)$  with  $r^2$  is accompanied by the spatial oscillations of the spin density along the  $x'$  axis.

A distinctive feature of Eq. (12) is the very simple dependence of  $M_z(\mathbf{r}, t)$  on the magnetic field. The spin density oscillates (in addition to the diffusive relaxation) with the frequency  $\Omega_L$  at any point  $\mathbf{r}$  and there is no threshold value  $\Omega_L \sim 1/\tau_s$  (see, e.g., [13]) for the frequency of these oscillations. Of course, this peculiarity is a consequence of the special choice  $\mathbf{B} \parallel \Omega(\mathbf{k}) \parallel [1\bar{1}0]$  we take in our consideration. If these restrictions relax, the evolution of the spin density will become much more complicated. We will not go into details of the influence of the magnetic field on the anisotropy of the spin diffusion. It seems likely that the transverse magnetic field is not especially useful when studying the anisotropy of the inhomogeneous spin distribution, since this field itself is a source of the anisotropy. This topic requires an additional analysis and is outside the scope of this paper.

The general case, Eq. (12), of arbitrary relation between the spot size  $a$  and the spin diffusion length  $L_s$  is rather complicated. To give a more physical insight into the spin diffusion, let us consider two limiting cases of the small and large laser spot size  $a$  as compared with the spin diffusion length  $L_s$ . If  $a \gg L_s$  then  $F \approx a^2$  and Eq. (12) gives the well known [9] decaying oscillations of the homogeneous spin density

$$M_z(t) \approx \frac{M_0}{a^2} \exp\left(-\frac{t}{\tau_s}\right) \cos(\Omega_L t). \quad (13)$$

In order to understand better the opposite limit of strong inhomogeneity  $a \ll L_s$ , we formally set  $a = 0$  in Eq. (12). Then  $F = 4Dt$  and we get from Eq. (12)

$$M_z(\mathbf{r}, t) \approx \frac{M_0}{4Dt} \exp\left(-\frac{r^2}{4Dt}\right) \cos\left(\frac{x'}{L_s} - \Omega_L t\right). \quad (14)$$

The temporal behavior of the spin density, given by this equation, is distinctly different from that of the isotropic spin distribution [13] (in zero magnetic field), since the combination  $t/\tau_s$  does not enter Eq. (14) at all. Instead, *at every point*  $\mathbf{r}$  much slower diffusive relaxation occurs, in particular, at the center of the laser spot  $M_z(\infty 1/t)$ . To obtain the physically meaningful spin density  $M_z(\mathbf{r}, t)$ , we must substitute in Eq. (12) small but finite  $a \approx \lambda$ , where  $\lambda$  is the laser wavelength. A more careful analysis of Eq. (12) shows that the exponential decrease with time of the spin density at  $\mathbf{r} = 0$  still persists at small times  $t \lesssim \tau_s(a/L_s) \ll \tau_s$ , and only then the spin density decreases as  $1/t$ . Thus, Eq. (14) is valid at all but small times  $t \ll \tau_s$ .

The spin relaxation time  $\tau_s$  enters Eq. (14) only through the spin diffusion length  $L_s$ , which determines in this case the scale of the anisotropy variation. It is seen from this equation that the pronounced anisotropy of the spin distribution appears at the distances  $r \gtrsim L_s$ , from the laser spot.

The evolution of the inhomogeneous spin density is a result of the spin precession in the angular space and the spin diffusion in the coordinate space. When the anisotropy of the spin splitting is strong, the interplay between the gradient of the spin density and the spin precession (see the term with the operator  $\mathbf{b}$  in Eq. (3)) leads to the unusual temporal behavior of the spin density given by Eq. (14). It is instructive to see the temporal evolution of the *total* spin polarization of the QW. Integrating Eq. (14) over the QW plane, we obtain immediately

$$\int M_z(\mathbf{r}, t) d\mathbf{r} \sim M_0 \exp\left(-\frac{t}{\tau_s}\right) \cos(\Omega_L t). \quad (15)$$

Thus, the total spin polarization undergoes exponentially decaying oscillations as in the homogeneous case irrespective of the relationship between  $a$  and  $L_s$ . This clearly demonstrates that the unusual temporal behavior of Eq. (14) is a consequence of the spatial redistribution of the spin density, which, in turn, arises due to the anisotropy of the spin diffusion.

In conclusion, we have shown that in the (001) grown zinc-blende semiconductor QW, the anisotropy of the spin splitting, resulting from the simultaneous presence of the bulk and structure inversion asymmetries, leads to the anisotropic in the QW plane spin diffusion. This anisotropy manifests itself most strongly if the Dresselhaus and Rashba spin splittings are comparable in magnitude and if the initial size of the spin packet is much less as compared to the spin diffusion

length. Though our calculations refer to the special case of equal Dresselhaus and Rashba spin splittings, they point to the trend of how the spin distribution changes when the anisotropy of the spin splitting appears. To observe the predicted behavior of the spin density given by Eq. (14), it is advantageous to use an experimental technique similar to that in [20], where the time-resolved Faraday rotation in an  $n$ -doped GaAs/AlGaAs QW was measured while applying a bias to the gate electrode. Among other things, the gate voltage can be used to modify the Rashba spin splitting, thereby creating the interference between  $V_{BIA}$  and  $V_{SIA}$ . We believe that experimental observations of the anisotropic spin diffusion can give an additional information on the relation between  $V_{BIA}$  and  $V_{SIA}$ . In addition, we have shown that the interference affects not only the anisotropy of the spin-density distribution but also the temporal evolution of the spin density at  $\mathbf{r} = 0$ , measured at the overlapping pump and probe laser spots. Hence, the decay of the spin density with time (in time resolved experiments) can deviate from a purely exponential form when the spin-relaxation rate is slow and, as a consequence, the spin diffusion length is large. This should be kept in mind when extracting the spin-relaxation times from experimental data. We would like to draw attention to the symmetry relation given by Eq. (7), which is also accessible to experimental verification. This relation is not connected with the interference of  $V_{BIA}$  and  $V_{SIA}$  but is an inherent characteristic of the DP spin-relaxation mechanism. Hence, it can help in the discrimination between different spin-relaxation mechanisms. As the symmetry relation Eq. (7) is characteristic for DP spin relaxation, the violation of this relation would imply that DP spin relaxation is not dominant.

This work was supported by the Russian Foundation for Basic Research and by programs of the Russian Ministry of Science.

## REFERENCES

1. Special Issue on Semiconductor Spintronics, *Semicond. Sci. Technol.* **17**, 275 (2002).
2. E. L. Ivchenko, Yu. B. Lyanda-Geller, and G. E. Pikus, *Zh. Éksp. Teor. Fiz.* **98**, 989 (1990) [*Sov. Phys. JETP* **71**, 550 (1990)]; A. G. Aronov, Yu. B. Lyanda-Geller, and G. E. Pikus, *Zh. Éksp. Teor. Fiz.* **100**, 973 (1991) [*Sov. Phys. JETP* **73**, 537 (1991)].
3. W. Knap, C. Skierbiszewski, A. Zduniak, *et al.*, *Phys. Rev. B* **53**, 3912 (1996).
4. S. Datta and B. Das, *Appl. Phys. Lett.* **56**, 665 (1990).
5. M. I. D'yakonov and V. I. Perel, *Zh. Éksp. Teor. Fiz.* **60**, 1954 (1971) [*Sov. Phys. JETP* **33**, 1053 (1971)]; *Fiz. Tverd. Tela (Leningrad)* **13**, 3581 (1971) [*Sov. Phys. Solid State* **13**, 3023 (1972)].
6. G. Dresselhaus, *Phys. Rev.* **100**, 580 (1955).
7. M. I. D'yakonov and Y. Yu. Kachorovskii, *Fiz. Tekh. Poluprovodn. (Leningrad)* **20**, 178 (1986) [*Sov. Phys. Semicond.* **20**, 110 (1986)].

8. Yu. L. Bychkov and E. I. Rashba, *J. Phys. C* **17**, 6093 (1984).
9. D. D. Awschalom and J. M. Kikkawa, *Phys. Today* **52**, 33 (1999).
10. J. M. Kikkawa and D. D. Awschalom, *Phys. Rev. Lett.* **80**, 4313 (1998).
11. N. S. Averkiev and L. E. Golub, *Phys. Rev. B* **60**, 15582 (1999).
12. N. S. Averkiev, L. E. Golub, and M. Willander, *Fiz. Tekh. Poluprovodn. (St. Petersburg)* **36**, 97 (2002) [*Semiconductors* **36**, 91 (2002)].
13. V. A. Froltsov, *Phys. Rev. B* **64**, 45311 (2001).
14. A. G. Mal'shukov and K. A. Chao, *Phys. Rev. B* **61**, 2413 (2000).
15. M. M. Glazov and E. L. Ivchenko, *Pis'ma Zh. Éksp. Teor. Fiz.* **75**, 476 (2002) [*JETP Lett.* **75**, 403 (2002)].
16. H. Haug and S. W. Koch, *Quantum Theory of the Optical and Electronic Properties of Semiconductors* (World Scientific, Singapore, 1995, 3rd ed.).
17. B. Mieck, H. Haug, W. A. Hügel, *et al.*, *Phys. Rev. B* **62**, 2686 (2000).
18. B. Jusserand, D. Richards, G. Allan, *et al.*, *Phys. Rev. B* **51**, 4707 (1995).
19. M. E. Flatté and J. M. Byers, *Phys. Rev. Lett.* **84**, 4220 (2000).
20. J. S. Sandhu, A. P. Heberle, J. J. Baumberg, and J. R. A. Cleaver, *Phys. Rev. Lett.* **86**, 2150 (2001).

# Experimental Study of a Normal-Metal Hot Electron Bolometer with Capacitive Coupling

M. Tarasov<sup>1,3</sup>, M. Fominskii<sup>1,3</sup>, A. Kalabukhov<sup>2,3</sup>, and L. Kuzmin<sup>2,3</sup>

<sup>1</sup> Institute of Radio Engineering and Electronics, Russian Academy of Sciences, ul. Mokhovaya 18, Moscow, 103907 Russia

<sup>2</sup> Moscow State University, Vorob'evy gory, Moscow, 119899 Russia

<sup>3</sup> Chalmers Technological University, S41296 Göteborg, Sweden

Received September 19, 2002

Normal-metal hot-electron bolometer with capacitive coupling (CCNHEB) is a further development of the concept of a normal-metal hot-electron bolometer with Andreev mirrors (ANHEB). It was proposed to eliminate the frequency and energy restrictions inherent in ANHEB, in which Andreev mirrors act efficiently only with relatively long absorbers and at energies below the superconducting gap. An important advantage of the CCNHEB is its simple topology, in which the same tunnel junctions provide thermal decoupling, noise protection, temperature measurement, and it can be used for electron cooling. The temperature response of the bolometer was measured at temperatures down to 260 mK. The observed response  $dV/dT = 1.7$  mV/K corresponds to the sensitivity  $S = 0.4 \times 10^9$  V/W. The measured noise at the amplifier output with this sample was found to be  $V_{na} = 4$  nV/Hz<sup>1/2</sup>, which corresponds to a noise-equivalent power of  $10^{-17}$  W/Hz<sup>1/2</sup>. To measure optical response, black-body radiation was used as a source of signal inside the cryostat. The source was a thin NiCr film sputtered on a thin sapphire substrate and suspended by nylon threads. Optical measurements proved to be in good agreement with the dc measurements. © 2002 MAIK "Nauka/Interperiodica".

PACS numbers: 07.57.Kp

## 1. Topology of the samples and their fabrication.

The concept of a normal-metal hot-electron bolometer with capacitive coupling (CCNHEB) was suggested in [1]. The key idea of the design is that the capacitive decoupling replaces Andreev mirrors, which are used for the thermal insulation of an absorber from electrodes in a normal-metal hot-electron bolometer with Andreev mirrors (ANHEB). This allows one to avoid the frequency restriction inherent in the Andreev mirrors, which arises if electrons are superheated above the energy gap. Matching of the absorber impedance at the signal frequency is accomplished through the same capacitors that provide a high potential barrier for hot electrons. For a planar complementary antenna on the silicon substrate, the impedance can be estimated by the formula  $Z_{ant} = 377[2(1 + \epsilon)]^{1/2} = 80 \Omega$ . The bolometer impedance is the sum of capacitive, inductive, and resistive components connected in series:

$$Z_{bol} = \frac{2}{i\omega C} + i\omega L + R. \quad (1)$$

For the planar antenna with real impedance, the inductance of the absorber stripe can be counterbalanced by the tunnel junction capacitance. For an absorber length of 10  $\mu\text{m}$ ,  $Z_L = 20 \Omega$  at 300 GHz, the required capacitive impedance is 30 fF, which can easily be obtained with tunnel junctions of size  $1 \times 0.5 \mu\text{m}^2$ . As a result, an additional band-pass filter forms, which additionally reduces the undesirable action of the thermal back-

ground radiation. Simultaneously, the same tunnel junctions act as temperature sensors and provide electron cooling, similar to the Peltier effect in semiconductors.

Samples were prepared on silicon substrates of size  $7 \times 7$  mm with 16 contact pads. Each chip included six CCNHEB structures, of which one was integrated with a log-periodic antenna, four integrated with double dipole antennas for central frequencies of 300 and 600 GHz, and one test structure with two additional tunnel junctions was designed for measuring temperature along the absorber stripe (cf. microphotograph in Fig. 1). The contact pads and antennas were fabricated by UV lithography and sequential thermal evaporation of 10-nm Cr, 40-nm Au, and 10-nm Pd layers. The structure of bolometer was formed in a single vacuum cycle by direct electron-beam lithography and shaded evaporation at different angles through a double mask made from PMMA and COPOLYMER photoresists. In so doing, 60 nm Al was evaporated, oxidized for 2 min in oxygen at a pressure of  $10^{-1}$  mbar, after which a double-layer Cr/Al film was evaporated at a different angle. The normal metal film in the bolometer was 8  $\mu\text{m}$  long, 0.2  $\mu\text{m}$  wide, and 80 nm in thickness. The resistance of the bolometers with double-layer films consisting of 50 nm Cr and 10 nm Al was about 100  $\Omega$ , which was close to the optimal resistance of both log-periodic and double dipole antennas. The results of measuring with a sample containing 50% chromium and 50% aluminum are also presented for comparison. The capaci-

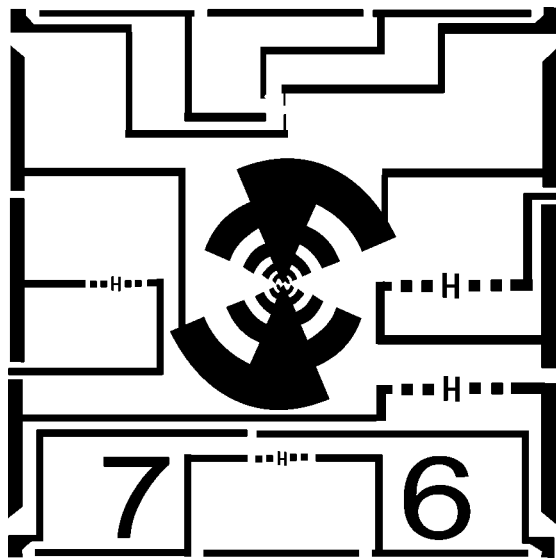


**Fig. 1.** Microphotograph of a bolometer chip with 16 contact pads and six CCHNEB structures. Log-periodic antenna is at the center; two double dipole antennas for the central frequency 300 GHz are on the right and two antennas for 600 GHz are on the left and at the bottom.

tance of tunnel junctions was about 3 fF, so that, for two capacitors connected in series, 100  $\Omega$  of bolometer, and intrinsic inductance, the resonance frequency was about 250 GHz.

**2. Experimental results.** The samples were placed on a flat surface of a hyperhemispheric sapphire lens that was mounted on the He3 evaporator of a closed-cycle absorptive cryo cooler (see [2]). The cryo cooler was mounted on the cold plate of a helium cryostat (Infrared Labs [3]) with optical window. Liquid helium vapor was pumped until a temperature of 1.7 K was reached. The minimal temperature in the system was

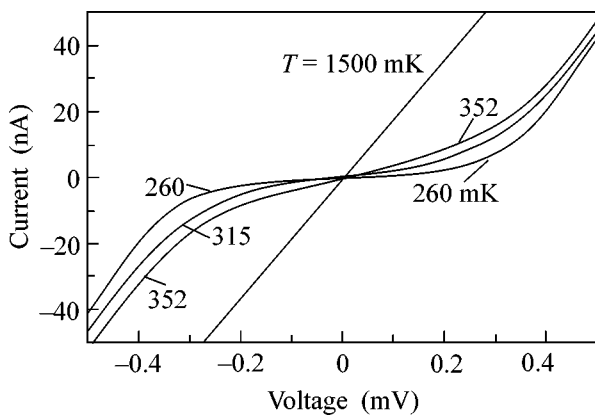


**Fig. 2.** Current–voltage characteristics of bolometer, as measured at temperatures from 260 mK to 1.5 K.

260 mK. Figure 2 presents the IV curves for one of the samples. These dependences can be used to obtain the temperature dependence of voltage and the sensitivity  $dV/dT$  at different temperatures and dc currents (Fig. 3).

To determine the bolometer sensitivity and noise for a real microwave signal, a black-body radiation source with modulated temperature (Haller-Beeman Assoc. Inc.; see [4] for detail) was used as a signal source. The source was a thin NiCr film sputtered on a thin sapphire substrate suspended by thin nylon threads. On passing current through the film, it is heated and starts to radiate. The source was mounted on the cold plate of a cryostat at the base temperature of 1.7 K, and its output horn was directed toward the lens with CCHNEB placed at a distance of several centimeters from the source. After applying a power of several milliwatt from the power supply, a radiation with equivalent temperature of up to 100 K arises. The source is capable of producing modulated signals over a wide frequency range. The dependences of the bolometer response on the bias voltage, as measured in the temperature variation regime (Fig. 4, curve DVT) and for the built-in radiation source (curve DV 249 mV), demonstrate a reasonable agreement with the theoretical estimates.

To estimate the NEP, low-frequency noise was measured at the bolometer output. The frequency dependence was measured for the voltage fluctuation spectral density, and the noise dependence on bias voltage was measured at several frequencies. In the sample with 50 nm chromium and 10 nm aluminum, the noise of bolometer and amplifier at the operating point with maximal response was 4 nV/Hz<sup>1/2</sup>. The dependence of noise spectral density on bias voltage in the white-noise region is shown in Fig. 5 for the sample with 30 nm chromium and 30 nm aluminum. It follows from these measurements that the noise spectral density in amplifier can be put equal to 3 nV/Hz<sup>1/2</sup>, which corresponds to the specifications of an OP27 operational ampli-

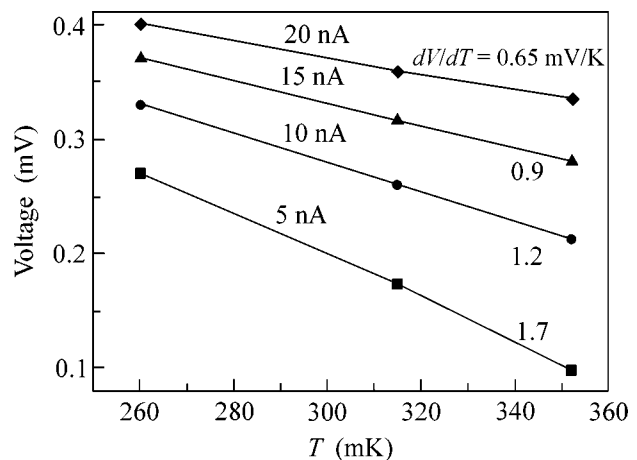


**Fig. 3.** Temperature dependences of the voltage on bolometer for various bias currents.

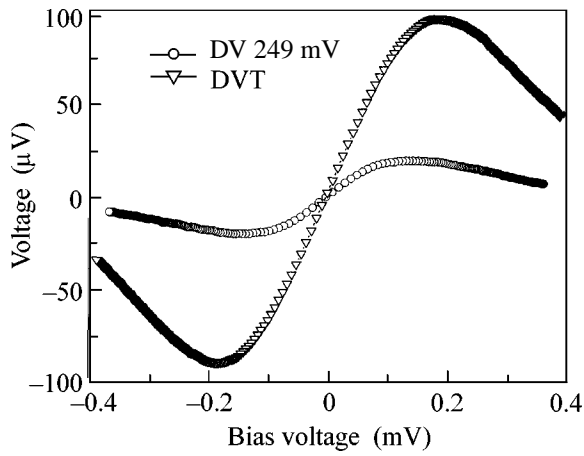


**Fig. 4.** CCHNEB voltage response (curve DVT) to a change in temperature and (curve DV 249 mV) to the black-body radiation.

fier—bolometer with an amplifier at the operation point of 200  $\mu\text{V}$  at a level of 6.5  $\text{nV}/\text{Hz}^{1/2}$  for 3 kHz and higher, and 8.5  $\text{nV}/\text{Hz}^{1/2}$  for 1 kHz.

High response for the samples with double-layer absorber films is different from the value predicted by a simple theory for SIN (superconductor–insulator–normal metal) gauge and may be due to the influence of electron cooling.

**3. Discussion of results and estimate of the CCHNEB sensitivity.** The theoretical values of response for the SIN junction can be obtained using the simple analytic expression

$$I(V, T) = \frac{k}{eR} \sqrt{11TT_c} \exp\left(-\frac{1.76T_c}{T}\right) \sinh\left(\frac{eV}{kT}\right), \quad (2)$$

which gives a good agreement with experimental data for the SIN junction with a purely chromium absorber. This expression can be used to determine maximal temperature response for the SIN junction at various ambient temperatures. For our base temperature of 270 mK, a single junction should have a response of about 0.5 mV/K; to increase it twofold (to 1 mV/K), electron temperature should be 163 mK. The experimentally observed high values of response can be explained by the combined action of two mechanisms: electron cooling and increase of the junction nonlinearity due to the proximity effect, so that it should be considered as an SINS structure, which approaches the SIS\* (superconductor–insulator–superconductor with reduced gap) structure in the zero-temperature limit.

The noise in a structure consisting of two tunnel junctions connected in series can be calculated using

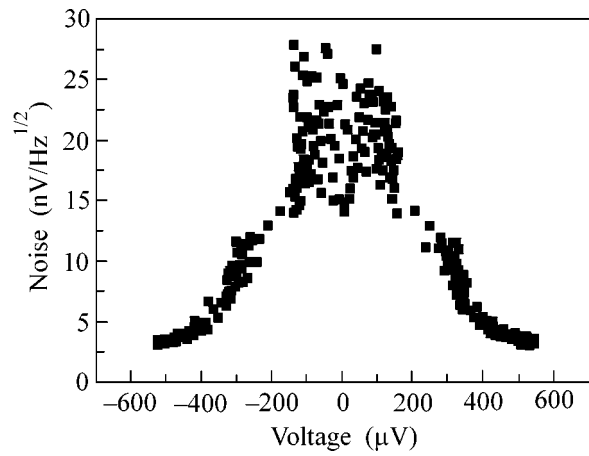


**Fig. 5.** Dependence of the noise in the range 1–10 kHz on the bias voltage on a bolometer with 30 nm chromium and 30 nm aluminum. At biases higher than 500  $\mu\text{V}$ , noise is restricted by the amplifier.

the following simple expression for the current fluctuation spectral density in a single junction:

$$S_I(V) = \frac{2eV}{R} \coth\left(\frac{eV}{2kT}\right). \quad (3)$$

To obtain voltage fluctuations, one should multiply this expression by the dynamic resistance of junctions. It can be found from Eq. (2). The calculated dependences of the dynamic resistance and noise on the bias voltage proved to be close to the measured dependences.

In our first experiments [5], the values of the limiting CCHNEB parameters ( $\text{NEP} = 2.5 \times 10^{-17} \text{ W}/\text{Hz}^{1/2}$ ) were far from the theoretical estimates, because we used non-optimal samples leading to a high noise level in the subsequent signal amplifier. In this work, the slope  $dV/dT = 1.7 \text{ mV}/\text{K}$  was obtained for the MF46p6-16 sample at 260 mK. When estimating the voltage response  $S = dV/dP = (1/G)dV/dT$ , we used the values for the heat conduction  $G = dP/dT = 3\Sigma vT^4$ , characteristic constant of material  $\Sigma = 2.5 \times 10^9 \text{ W m}^{-3} \text{ K}^{-5}$  (measured in a separate experiment with ANHEB samples calibrated against the dissipated power of a dc power supply in a copper film; for the samples with double-layer absorber films, an additional detailed study is needed for the temperature dependence of the characteristic constant of material), and sample volume  $n = 8 \times 10^{-20} \text{ m}^3$ , which gives  $G = 5 \times 2.5 \times 10^9 \times 8 \times 10^{-20} (0.256)^4 = 4.3 \times 10^{-12} \text{ W}/\text{K}$  and  $S = 1.7 \times 10^3 / (4.3 \times 10^{-12}) = 0.4 \times 10^9 \text{ V}/\text{W}$ . For the output noise of bolometer and amplifier,  $V_{na} = 4 \text{ nV}/\text{Hz}^{1/2}$ , the NEP is  $V_{na}/S = 6 \times 10^{-18} \text{ W}/\text{Hz}^{1/2}$ . An example of the measured NEP is presented in Fig. 6. In the absorber film consisting of normal and superconducting layers, all hot electrons are concentrated in the normal metal film because of the Andreev reflection. This reduces effectively the volume

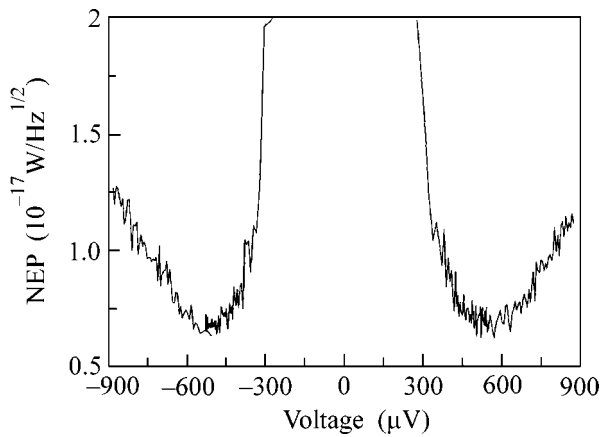


**Fig. 6.** Noise-equivalent power measured for the sample with 30 nm Cr and 30 nm Al in the absorber film.

and, correspondingly, enhances the volt-watt sensitivity. The gain is caused by the effective decrease in the volume of normal metal, the proximity effect, the Andreev reflection, and the electron cooling. An important advantage of a high response is that the requirements to the subsequent amplifier become less stringent.

The electrical NEP presented above should be compared with the optical NEP measured using black-body radiation. For the MF46p6-16 sample with a log-periodic antenna, the radiation linewidth was found to be  $5^\circ$  in the  $E$  plane and  $30^\circ$  in the  $H$  plane. A decrease in the source radiation temperature was  $\eta = (3/46)(3/7.7) = 1/40$ . Moreover, one should take into account the reflection loss at the vacuum/insulator interface, the impedance mismatch, the degree of blackness of the black-body source, the mismatch in the direction of antenna major lobe, and the side lobe loss, which altogether add

no less than 10 dB additional loss. As a result, the radiation weakens more than 400 fold. The received radiation power  $\Delta P = \eta k \Delta T \Delta f = 10^{-13}$  W and a response slope of  $0.4 \times 10^9$  V/W should provide a value of 40  $\mu$ V for the voltage response. The value of 20  $\mu$ V measured for the voltage response to the black-body radiation is in a good agreement with the measured value.

**4. Conclusions.** Normal-metal hot-electron bolometer with capacitive thermal insulation integrated with planar submillimeter wave antennas have been designed, fabricated, and experimentally investigated. The electrical sensitivity was as high as 1.7 mV/K, the response  $S = 0.4 \times 10^9$  V/W, and the noise-equivalent power was  $10^{-17}$  W/Hz $^{1/2}$ . The measured response to the black-body radiation is in good agreement with the noise-equivalent electrical power measured at various temperatures. The results obtained give evidence for the efficient operation of the bolometer with capacitive thermal insulation.

This work was supported by the STINT, KVA, VR, and INTAS (grant nos. 01-686, 00-384).

#### REFERENCES

1. L. Kuzmin, *Physica B (Amsterdam)* **284-288**, 2129 (2000).
2. L. Duband and B. Collaudin, *Cryogenics* **39**, 659 (1999).
3. Infrared Labs, <http://www.irlabs.com/catalog/cdewarindex.html>.
4. Haller-Beeman Assoc. Inc, <http://www.haller-beeman.com>.
5. B. Choi, L. Kuzmin, D. Chouvaev, and M. Tarasov, in *Proceedings of 4th International Workshop from Andreev Reflection to the International Space Station, Bjorkliden, Kiruna, Sweden, 2000*, p. 289.

*Translated by V. Sakun*

# Acoustic Magnetoplasma Excitations in Double Electron Layers

S. V. Tovstonog, I. V. Kukushkin, L. V. Kulik, and V. E. Kirpichev

*Institute of Solid State Physics, Russian Academy of Sciences, Chernogolovka, Moscow region, 142432 Russia*

*e-mail: tovstons@issp.ac.ru*

Received September 20, 2002

The inelastic light scattering technique is used to study the spectra of intraband excitations of the quasi-two-dimensional electron system in GaAs/AlGaAs double quantum wells. A new collective mode, namely, the acoustic plasmon, is discovered and investigated. The dispersion law of the acoustic mode and its dependence on the electron density are measured. It is shown that, in a perpendicular magnetic field, a hybridization of the acoustic plasmon with the cyclotron mode takes place. The properties of the hybrid acoustic magnetoplasma collective excitations are studied. © 2002 MAIK “Nauka/Interperiodica”.

PACS numbers: 73.21.Fg; 73.20.Mf; 78.66.Fd

The development of semiconductor heterostructure technology has made it possible to fabricate samples with parallel 2D electron channels located close to each other. An example of such structures are the double quantum wells (DQWs), in which two interacting electron–electron or electron–hole layers are separated by a barrier of width  $d$ . It has been predicted that the inter-layer electron–electron interaction strongly affects the electron energy spectrum in the integer and fractional quantum Hall effect [1, 2], gives rise to fractions with even denominators [3], and increases the stability of the Wigner crystal state [4]. Accordingly, the collective excitation spectrum of a DQW is modified as compared to the collective excitation spectrum of a single quantum well (SQW).

The collective excitation spectrum of a DQW contains two plasma modes associated with the in-phase (an optical plasmon, OP, with the square-root dispersion law) and antiphase (an acoustic plasmon, AP, with a linear dispersion law) oscillations of charge density in the DQW layers. The properties of the AP and OP were studied in many theoretical publications [5–7]. For example, the Coulomb interaction determines the dispersion of the AP mode [8], and both types of excitations, AP and OP, are essential for the interpretation of the Coulomb drag effects in double-layer structures [9]. It is expected that, unlike the plasma oscillations of a 2D electron gas in a single quantum well, the low-lying AP is more sensitive to the Landau damping [8, 9], i.e., to the energy transfer from the plasmon (the coherent mode) to a single-particle excitation (SPE). In addition, in such a structure, the acoustic plasmon may be involved in the mechanism of high-temperature superconductivity [10].

The inelastic light scattering spectroscopy (ILS) is a powerful instrument for studying the energy spectra of

low-dimensional systems. In contrast to the transport measurements, which imply averaging over all wave vectors [11], the ILS technique provides the determination of the plasmon energy in a DQW as a function of the wave vector. However, since the practical implementation of this technique involves certain difficulties, the number of experiments devoted to studying the APs in two-component semiconductor systems is fairly small [12, 13].

This paper reports on the ILS study of the intraband excitation mode, namely, the acoustic plasmon, in double electron systems with a spatial charge separation. In addition, the behavior of this mode was investigated in an external magnetic field oriented normally to the well plane, the magnetic field giving rise to a hybrid acoustic magnetoplasmon collective excitation. The purpose of the study was to identify the AP line in the collective excitation spectrum of the electron system, to measure the dispersion of this excitation, and to reveal the influence of such parameters as the electron density in the wells, the distance between the quantum wells, and the magnetic field.

**Experimental.** The experiments were performed on three high-quality samples grown by molecular–beam epitaxy (MBE) so that each sample represented two GaAs quantum wells separated by an  $\text{Al}_{0.3}\text{Ga}_{0.7}\text{As}$  barrier. The barrier width was different in different samples, and the wells were symmetrically doped with a Si  $\delta$ -layer. Structure (A) is a DQW (see the upper inset in Fig. 2) with the 260 and 300 Å wide wells and a 50 Å wide barrier (260/50/300). Structures (B) and (C) are DQWs with the parameters 250/180/250 and 200/25/200, respectively. The electron mobility exceeded  $10^6$  cm<sup>2</sup>/V s in all structures. The photoexcitation of the system was performed by a tunable Ti/Sp laser, which had the photon energy within 1.545–

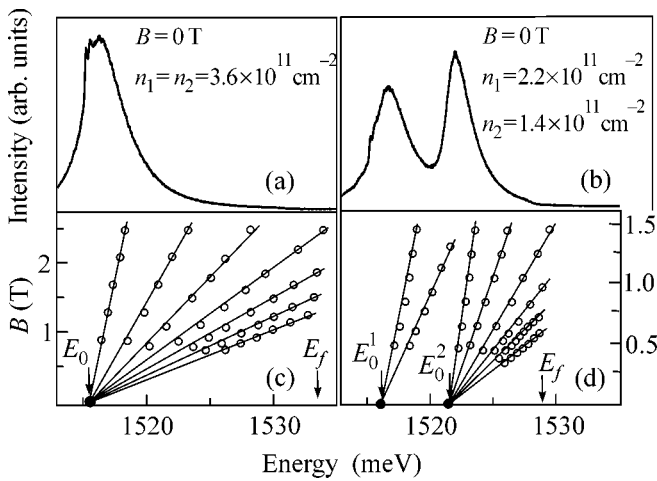


**Fig. 1.** Photoluminescence spectra measured for the 200/25/200 DQW in zero magnetic field with (a) equal and (b) unequal electron concentrations in the two wells. Plots (c) and (d) represent the “fans” of Landau levels for cases (a) and (b), respectively. The arrows indicate the Fermi energy and the position of the bottom of the ground subband of dimensional quantization  $E_0$ ; in case (a),  $E_0^1 = E_0^2 = E_0$  and, in case (b),  $E_0^1 \neq E_0^2$ .

1.570 eV and the characteristic power density  $W = 0.1$ – $1$  W/cm<sup>2</sup>, and by a He–Ne laser with a photon energy of 1.958 eV ( $W = 0$ – $0.01$  W/cm<sup>2</sup>). The high quality of the samples was indirectly confirmed by the fact that the widths of the spectral lines obtained from the inelastic light scattering spectra and from the photoluminescence spectra reached 0.15 meV. The spectral instrument was a T64000 triple monochromator, which, in combination with a CCD camera, provided a spectral resolution of 0.02 meV. The measurements were carried out at temperatures within 1.5–4.2 K, in magnetic fields from 0 to 10 T, in the Faraday geometry. Part of the polarization measurements were performed in an optical cryostat. For the measurements, a two-waveguide scheme was used [14]. One waveguide served for photoexcitation, and the other, for the detection of the ILS and photoluminescence signals. In recording the ILS spectra, the positions of the waveguides with respect to the sample surface determined the quasi-momentum transferred to the system. The concentration of 2D electrons ( $n$ ) in each of the two wells was measured by the standard method, from the luminescence spectra in a perpendicular magnetic field [15]. It was found that, in the case of the intrawell illumination (without He–Ne), the electron concentrations in the two wells coincided and the total concentration was equal to 6.2, 3.8, and  $7.2 \times 10^{11}$  cm<sup>-2</sup> for samples (A), (B), and (C), respectively. In addition, it was found that, in sample (C), the 2D electron concentration could be controlled by varying the conditions of continuous photoexcitation. Namely, the sample illumination with light whose photon energy exceeded the width of the

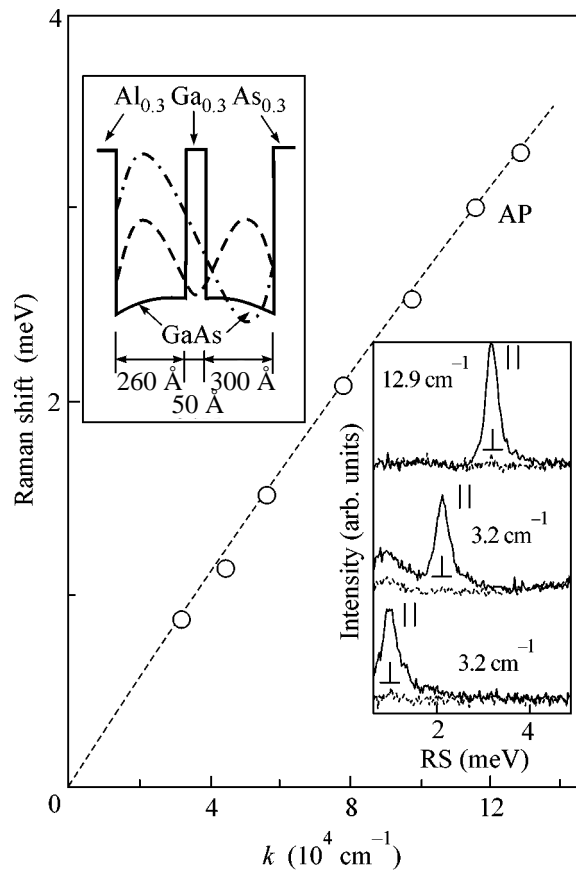


**Fig. 2.** AP dispersion measured for the 260/50/300 DQW with a carrier concentration of  $3.1 \times 10^{11}$  cm<sup>-2</sup> in each well: the empty circles represent the experiment and the dashed line illustrates the theory. The upper inset is a schematic representation of the DQW. The lower inset shows the inelastic light scattering spectra measured with two polarization configurations for different quasi-momenta  $k$  in zero magnetic field.

AlGaAs band gap (the barrier-type photoexcitation) reduced the quasi-equilibrium concentration of 2D electrons in the channel the stronger the greater the light power density was. The mechanism of this effect is similar to that discovered and investigated previously for single heterojunctions [16]. The interval of the concentration variation in the 2D channel was mainly determined by the doping impurity concentration in the barrier (in our case, it was the Si  $\delta$ -layer). The source of the control illumination was the He–Ne laser whose power density on the sample was varied from 0 to 0.01 W/cm<sup>2</sup>, and the corresponding variation of the total carrier concentration in sample (C) was between 7.2 and  $2.3 \times 10^{11}$  cm<sup>-2</sup>. The concentration variations were different in the two channels of the DQW (owing to the finite depth of light penetration). However, as was mentioned above, we could measure these concentrations independently. It should also be noted that, for all three samples, a stationary photoexcitation by the pumping Ti/Sp laser, whose photon energy was less

than the AlGaAs band gap width but greater than the GaAs band gap width, did not noticeably affect the electron concentration in the whole range of power densities used in the experiment.

Figure 1 shows the spectra of the recombination radiation of 2D electrons and photoexcited holes. The spectra were measured for the 200/25/200 DQW at the temperature  $T = 4.2$  K in zero magnetic field. The photoexcitation was performed by the Ti/Sp laser alone (Fig. 1a) and by the Ti/Sp and He–Ne lasers simultaneously (Fig. 1b). The first case corresponds to equal concentrations in the two wells, and the second case, to different concentrations (their values are indicated in the plot). Figures 1c and 1d present the “fans” of Landau levels obtained for these two cases as a result of processing a series of photoluminescence spectra in a perpendicular magnetic field. It should be noted that the photoluminescence and ILS spectra were recorded sequentially in the same experimental setup, without changing any external parameters. This guaranteed the one-to-one correspondence between the collective excitation energies of the 2D electron system, which were measured from the ILS spectra, and the 2D electron concentrations obtained from the photoluminescence spectra.

The lower inset in Fig. 2 presents the spectra of inelastic scattering of light that were measured for the 260/50/300 DQW. In the spectral range shown in this inset, one can see a dominant line denoted as AP in Fig. 2. To separate the ILS signal and the signal of hot luminescence (from the quantum well or from the GaAs substrate of the sample), which may occur in this spectral range, the ILS spectra were recorded for a series of different values of the pumping photon energy. In these records, the spectral position of the hot luminescence lines should remain unchanged while the position of the ILS lines should vary with varying pumping photon energy (the Raman shift  $RS = \text{const}$ ). This property together with the dependence of the position of the line on the quasi-momentum transferred to the 2D system (this dependence must be absent for the hot luminescence lines but is evident in the inset) allows a unique identification of the AP line observed in the spectrum as the line of inelastic light scattering by the excitation of the 2D electron system. To determine the nature of the AP line, we performed polarization measurements to reveal its degree of polarization. Between the sample and the waveguides, we placed two linear polarizers, so that they could be either crossed or parallel. According to the selection rules, the mode that can be observed in the ILS spectrum with parallel polarizers and cannot be seen with crossed polarizers represents a charge excitation of the system; in the opposite case, the mode corresponds to the spin excitation [17]. In the lower inset of Fig. 2, the spectra measured with parallel polarizers are shown by the solid lines and the spectra measured with crossed polarizers, by the dashed lines. As one can see, the line under investigation is present only in the spectrum obtained

with parallel polarizers and is completely absent in the crossed polarizer configuration. Thus, we can conclude that this line is associated with the charge excitation of the electron system. The empty circles in Fig. 2 present the dependence of the Raman shift of the AP line on the quasi-momentum transferred to the system in the process of the inelastic scattering of light. One can see that this dependence is close to linear. An acoustic plasmon in the DQW is characterized by a linear dispersion law in the region of small quasi-momenta  $k \ll 1/d$  [18]. In zero magnetic field, its energy as a function of carrier concentration, quasi-momentum, and distance between the wells is described by the expression

$$\omega_{AP}^2 = \frac{e^2 k}{2\epsilon\epsilon_0 m^*} (n_1 + n_2) \times \left[ \frac{1}{2} - \frac{1}{2} \sqrt{1 - \frac{4n_1 n_2}{(n_1 + n_2)^2} (1 - e^{-2kd})} \right], \quad (1)$$

where  $e$  is the electron charge,  $k$  is the quasi-momentum in the quantum well plane,  $m^* = 0.067m_0$  is the effective mass of 2D electrons,  $\epsilon$  is the dielectric constant of the medium,  $n_1$  and  $n_2$  are the charge densities in the first and second wells, and  $d$  is the effective distance between the layers. In the case of small quasi-momenta, when  $n_1 = n_2$ , this formula takes the form  $\omega_{AP}^2 = (e^2 k^2 dn_1)/(2\epsilon\epsilon_0 m^*) \sim k^2$ . From Eq. (1) with the parameters  $d = 330$  Å (the distance between the centers of the wells) and  $n_1 = n_2 = 3.1 \times 10^{11}$  cm<sup>-2</sup> (the concentrations determined from magnetoluminescence measurements), we can calculate the theoretical dependence of the AP energy on the quasi-momentum for the 260/50/300 DQW. The result of this calculation is shown in Fig. 2 by the dashed line.

As was mentioned above, for the 200/25/200 DQW sample, it was possible to vary the carrier concentration in both wells by a weak illumination from the He–Ne laser. This allowed us to measure the dependence of the energy of the AP mode under investigation on the total carrier concentration in the two layers and to compare it with the theoretical calculation by Eq. (1). The inset in Fig. 3 presents the ILS spectra measured in the parallel polarizer configuration at  $k = 1.17 \times 10^5$  cm<sup>-1</sup>. Case (a) corresponds to the minimal carrier concentration, and case (c), to the maximal one. From this plot, one can see that an increase in the electron concentration shifts the line toward higher energies. The experimental points and the dependence of the energy on  $\sqrt{n}$  ( $n = n_1 + n_2$  is the total 2D electron concentration in two layers) calculated by Eq. (1) are shown in Fig. 3. The dashed line represents the theoretical curve calculated for equal carrier concentrations in the two wells ( $n_1 = n_2$ ), and the solid line shows the curve calculated for the concentration values that were obtained from magnetoluminescence measurements ( $n_1 \neq n_2$ ). The close agreement of the experimental dependences of the AP

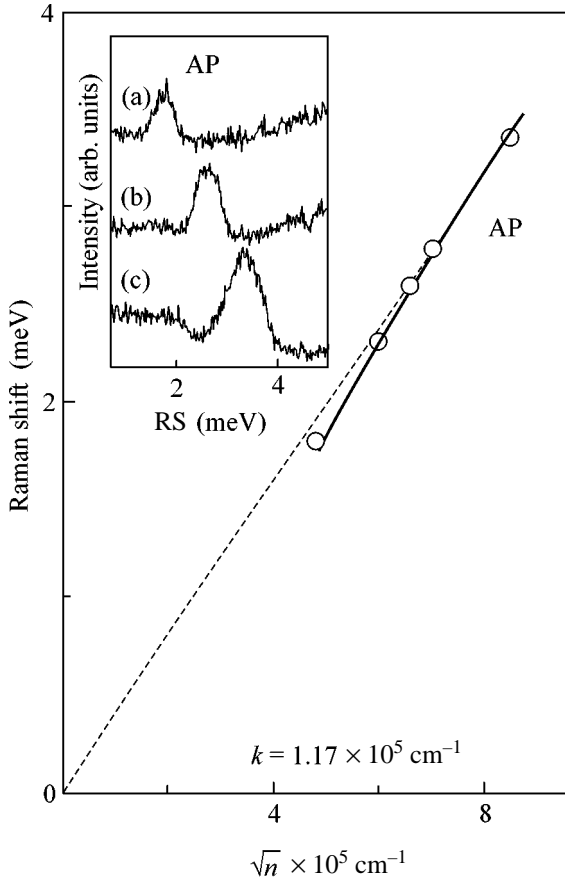


**Fig. 3.** Dependence of the AP energy on  $\sqrt{n}$ , where  $n$  is the total electron concentration in two wells. The dependence is measured for the 200/25/200 DQW at a fixed quasi-momentum value  $k = 1.17 \times 10^5 \text{ cm}^{-1}$ . The theoretical curves are shown by the dashed line (for  $n_1 = n_2$ ) and by the solid line (for  $n_1$  and  $n_2$  obtained from the experiment). The inset presents the inelastic light scattering spectra for (a)  $n_1 = 7 \times 10^{10} \text{ cm}^{-2}$  and  $n_2 = 1.6 \times 10^{11} \text{ cm}^{-2}$ ; (b)  $n_1 = 1.8 \times 10^{11} \text{ cm}^{-2}$  and  $n_2 = 2.5 \times 10^{11} \text{ cm}^{-2}$ ; and (c)  $n_1 = n_2 = 3.6 \times 10^{11} \text{ cm}^{-2}$ .

energy on  $k$  and on  $\sqrt{n}$  with the theory allows us to conclude that the AP line observed in the experiment corresponds to the inelastic light scattering by an acoustic plasmon in the two-layer electron system. An optical plasmon in such a system in the small quasi-momentum region must have a square-root dispersion law. A line with the corresponding properties was also observed by us in the ILS spectra. This line occurs in another spectral range (a Raman shift of about 6–10 meV), and its study is the subject of another paper [19].

The next step in the determination of the properties of the acoustic plasmon was the study of the behavior of the AP mode in the external magnetic field oriented normally to the well plane. In these conditions, the collective excitation spectrum of the system should be noticeably modified. In particular, the AP mode should

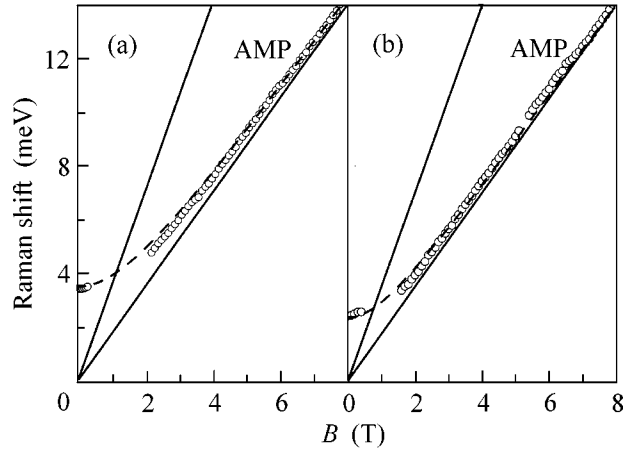


**Fig. 4.** Dependence of the energy of the hybridized acoustic magnetoplasma mode on the perpendicular magnetic field (empty circles) measured for the 200/25/200 DQW at  $k = 1.17 \times 10^{11} \text{ cm}^{-2}$ : (a)  $n_1 = n_2 = 3.6 \times 10^{11} \text{ cm}^{-2}$ ; (b)  $n_1 = 1.4 \times 10^{11} \text{ cm}^{-2}$  and  $n_2 = 2.2 \times 10^{11} \text{ cm}^{-2}$ . The solid lines show the dependences of the cyclotron electron energy  $E = N\hbar\omega_c$  on magnetic field for  $N = 1, 2$ , and the dashed lines show the results of the calculation by Eq. (2).

be transformed into a hybridized acoustic–magnetoplasma (AMP) mode as a result of the interaction of the AP mode with the cyclotron mode. As is shown in [19], in a perpendicular magnetic field, the energy of such a mode in a DQW with different types of carriers ( $m_1 \neq m_2$  and  $n_1 \neq n_2$ ) is described by the following expression obtained in the framework of classical electrodynamics:

$$\omega_{AP}^2 = \frac{\omega_{p1}^2 + \omega_{p2}^2 + \omega_{c1}^2 + \omega_{c2}^2}{2} - \sqrt{\left(\frac{\omega_{p1}^2 + \omega_{p2}^2 + \omega_{c1}^2 + \omega_{c2}^2}{2}\right)^2 + \omega_{p1}^2 \omega_{p2}^2 e^{-2kd}}, \quad (2)$$

where  $\omega_{p1}^2 = (e^2 n_1 k) / (2\epsilon\epsilon_0 m_1)$  and  $\omega_{p2}^2 = (e^2 n_2 k) / (2\epsilon\epsilon_0 m_2)$  are the energies of 2D plasmons with the electron concentrations  $n_1$  and  $n_2$  in the individual layers in zero magnetic field, and  $\omega_{c1}$  and  $\omega_{c2}$  are the cyclotron frequencies. Since, in the case under study, both wells contain carriers of the same type, namely, electrons ( $m_1 = m_2 = m^*$ ), we have  $\omega_{c1} = \omega_{c2} = eB/m^*$ .

We measured series of ILS spectra in a perpendicular magnetic field for all three samples and for different values of the quasi-momentum transferred to the system. For sample (C), we also measured the spectra for different concentrations of 2D electrons. The empty circles in Fig. 4 show the dependences of the energy of the AMP mode on magnetic field that were obtained from the ILS spectra for sample (C) in the case of equal carrier concentrations in the two wells ( $n_1 = n_2$ , the symmetric case, Fig. 4a) and in the case of unequal concen-

trations ( $n_1 \neq n_2$ , the asymmetric case, Fig. 4b). The values of these concentrations and the value of the transferred quasi-momentum are specified in the figure caption. The solid lines represent the dependences of the cyclotron electron energy  $E = N\hbar\omega_c$  (for  $N = 1, 2$ ) on magnetic field. From Fig. 4a, one can see that the energy of the acoustic magnetoplasmon ( $E_{AMP}$ ) at small fields  $B$  is equal to the AP energy at  $B = 0$ . As the magnetic field grows,  $E_{AMP}$  increases and, at large values of  $B$ , reaches the cyclotron energy ( $\hbar\omega_c$ ). In the second case ( $n_1 \neq n_2$ , Fig. 4b), in zero magnetic field,  $E_{AMP}$  is shifted to lower energies, and with increasing  $B$ , increases and tends to  $\hbar\omega_c$ , as in the case of  $n_1 = n_2$ . The dashed lines in Figs. 4a and 4b show the results of numerical calculations for the dependence of the energy of the AMP mode on magnetic field by Eq. (2) with the use of the parameter values taken from our experiment. The only fitting parameter was the effective distance between the layers  $d$ . The closest agreement was obtained for  $d = 25 \text{ \AA}$ , which exactly coincides with the distance between the well centers in the 200/25/200 DQW.

Thus, using the inelastic light scattering technique, we measured the dispersion law for the acoustic plasmon in double quantum wells and determined the modification of this spectrum with varying electron concentrations in the wells. In addition, we investigated the hybridization of the cyclotron and plasma modes in a perpendicular magnetic field and established that the magnetic-field dependence of the AMP energy is adequately described by expression (2) obtained in the framework of classical electrodynamics.

This work was supported by the Russian Foundation for Basic Research and by the Program "Physics of Solid-State Nanostructures."

## REFERENCES

1. K. von Klitzing, G. Dorda, and M. Pepper, *Phys. Rev. Lett.* **45**, 494 (1980).

2. D. C. Tsui, H. L. Stormer, and A. C. Gossard, *Phys. Rev. Lett.* **48**, 1559 (1982).
3. Y. W. Suen, H. C. Manoharan, X. Ying, *et al.*, *Phys. Rev. Lett.* **72**, 3405 (1994).
4. H. C. A. Oji, A. H. MacDonald, and S. M. Girvin, *Phys. Rev. Lett.* **58**, 824 (1987).
5. R. Z. Vitlina and A. V. Chaplik, *Zh. Éksp. Teor. Fiz.* **81**, 1011 (1981) [*Sov. Phys. JETP* **54**, 536 (1981)].
6. S. Das Sarma and A. Madhukar, *Phys. Rev. B* **23**, 805 (1981).
7. G. E. Santoro and G. F. Giuliani, *Phys. Rev. B* **37**, 937 (1988).
8. L. Liu, L. Swierkowski, D. Neilson, and J. Szymanski, *Phys. Rev. B* **53**, 7923 (1996).
9. K. Flensberg and B. Y.-K. Hu, *Phys. Rev. B* **52**, 14761 (1995).
10. P. M. Platzman and T. Lenosky, *Phys. Rev. B* **52**, 10327 (1995).
11. N. P. R. Hill, J. T. Nicholls, E. H. Linfield, *et al.*, *Phys. Rev. Lett.* **78**, 2204 (1997).
12. A. S. Bhatti *et al.*, in *Proceedings of the 23rd International Conference on the Physics of Semiconductors*, Ed. by M. Scheffler and R. Zimmermann (World Scientific, Singapore, 1996), p. 1899.
13. D. S. Kainth, D. Richards, H. P. Hughes, *et al.*, *Phys. Rev. B* **57**, R2065 (1998).
14. E. D. Isaacs and D. Heiman, *Rev. Sci. Instrum.* **58**, 1672 (1987).
15. I. Kukushkin and V. B. Timofeev, *Adv. Phys.* **45**, 147 (1996).
16. I. Kukushkin, K. von Klitzing, K. Ploog, *et al.*, *Phys. Rev. B* **40**, 4179 (1989).
17. A. Pinczuk, S. Schmitt-Rink, G. Danan, *et al.*, *Phys. Rev. Lett.* **63**, 1633 (1989); G. Abstreiter, R. Merlin, and A. Pinczuk, *IEEE J. Quantum Electron.* **22**, 1771 (1986).
18. D. S. Kainth, D. Richards, A. S. Bhatti, *et al.*, *Phys. Rev. B* **59**, 2095 (1999).
19. S. V. Tovstonog, L. V. Kulik, I. V. Kukushkin, *et al.*, *Phys. Rev. B* (2002) (in press).

*Translated by E. Golyamina*

# Charged Many-Particle Complexes: Properties of an Indirect Trion

D. V. Kulakovskii\* and Yu. E. Lozovik\*\*

\* *Institute of Solid State Physics, Russian Academy of Sciences, Chernogolovka, Moscow region, 142432 Russia*  
e-mail: kulakovd@issp.ac.ru

\*\* *Institute of Spectroscopy, Russian Academy of Sciences, Troitsk, Moscow region, 142092 Russia*  
e-mail: lozovik@isan.troitsk.ru

Received September 23, 2002

A system of spatially separated interacting excitons and electrons is considered. The formation of a spatially indirect trion in this system is investigated. The asymptotic behavior of the binding energy of this charged many-particle complex is determined in the limits of large and small layer separations. The variation of the binding energy due to screening by the 2D electron gas is calculated. The bound state of the spatially separated exciton and electron is shown to disappear from the collective excitation spectrum at a certain threshold concentration of 2D electrons. © 2002 MAIK “Nauka/Interperiodica”.

PACS numbers: 73.20.Mf; 71.10.Ca

Charged quasiparticles in a semiconductor, i.e., electrons and holes, can form different bound complexes, neutral or charged, which also represent elementary excitations in the semiconductor [1–6]. In recent years, the interest in these problems has quickened in connection with the studies of charged collective excitations in a two-dimensional (2D) electron gas. For example, a negatively charged complex of three quasiparticles called a trion ( $X^-$ ) in a single quantum well (QW) has been the object of many theoretical and experimental studies [6–13]. The problems concerned with such objects are more complicated than in the case of two-particle neutral complexes—excitons. This occurs because of the lack of the possibility to completely separate the motion of the center of mass from the relative motion in the Schrödinger equation. Therefore, a special formalism was developed for solving three-particle problems [6–11], which made it possible to some extent to elucidate the properties of charged complexes. The appearance of high-quality structures with double quantum wells gave rise to a new set of problems related to the properties of complexes of spatially separated particles: a spatially indirect exciton, a trion, etc. Indirect trions had already been studied earlier [14, 15]. It has been shown that, at sufficiently low temperatures and small layer separations, the formation of a bound state of an exciton with an electron is possible. However, the presence of an electron (or hole) channel in the structure leads to screening of the Coulomb interaction. In this connection, the present paper investigates the binding energy and the behavior of a bound trion complex in the presence of the 2D electron gas.

To study the formation of a spatially indirect trion, we follow the formalism used earlier for describing a spatially direct trion and employ the methods of evaluating the electron–exciton polarization interaction at large distances. We consider a system of two layers separated by a distance  $D$  along the  $z$  axis. One layer contains a two-dimensional exciton with a characteristic size  $a_B = \epsilon \hbar^2 / 2\mu e^2$ , and the other contains the electron gas. Ignoring the tunneling, we investigate the behavior of this system of spatially separated electron and exciton for the case of a small layer separation ( $D \ll a_B$ ) and for a large one ( $D \gg a_B$ ). We calculate the binding energy of the trion as a function of  $D$  and consider the disappearance of the bound state as a result of the screening by the 2D electron gas.

First, we consider the case of a large layer separation  $D \gg a_B$  (the upper inset in Fig. 1a). In the adiabatic approximation, when the binding energy of a direct exciton is much greater than the energy of the interaction of this exciton with an electron from the other layer, the Hamiltonian of this system can be represented in the form

$$\hat{H} = -\frac{\hbar^2}{2m_e}\Delta - \frac{\hbar^2}{2M_{\text{ex}}}\Delta + U(r_1, r_2, D) + E(X), \quad (1)$$

where  $E(X)$  is the energy of the relative motion of the exciton;

$$U(r_1, r_2, D) = -\frac{\gamma}{((r_1 - r_2)^2 + D^2)^2}, \quad \gamma = \frac{\alpha e^2}{2\epsilon} \quad (2)$$

is the polarization interaction of an isolated electron with an isolated exciton when the exciton radius is much smaller than the distance  $D$  between the layers; and  $\alpha$  is the polarizability of a two-dimensional exciton in the ground state:  $\alpha = 21a_B^3/16$  (see, e.g., [16]). Hence, the parameter  $\gamma$  involved in the expression for the effective interaction energy in the electron–exciton system is expressed as

$$\gamma = \frac{21e^2a_B^3}{32\epsilon}.$$

Here,  $\epsilon$  is the dielectric constant of the medium;  $M_{\text{ex}} = (m_e + m_h)$  is the total exciton mass; and  $m_e = 0.067m_0$  and  $m_h = 0.26m_0$  are the effective electron mass and the effective hole mass in the plane.<sup>1</sup>

Changing to the coordinates of the relative motion and of the trion center of mass, we represent the Hamiltonian in the form

$$\hat{H} = -\frac{\hbar^2}{2M_{\text{tr}}}\Delta - \frac{\hbar^2}{2\mu_{\text{tr}}}\Delta - \frac{\gamma}{(r^2 + D^2)^2} + E(X), \quad (3)$$

where  $M_{\text{tr}} = M_{\text{ex}} + m_e$  and  $\mu_{\text{tr}} = M_{\text{ex}}m_e/(M_{\text{ex}} + m_e)$ . The binding energy of the trion ( $X^-$ ) is determined from the Schrödinger equation

$$\hat{H}_{\text{rel}}\Psi(r, D) = E_B(X^-)\Psi(r, D), \quad (4)$$

where  $\hat{H}_{\text{rel}} = -\frac{\hbar^2}{2\mu_{\text{tr}}}\Delta - \frac{\gamma}{(r^2 + D^2)^2}$  is the Hamiltonian of the relative motion of the trion.

We first consider the asymptotic behavior of the solution for large values of  $D$  ( $D \rightarrow \infty$ ). For this purpose, we represent the exciton–electron interaction as a sum of two components:

$$U(r, D) = -\frac{\gamma}{[r^2 + D^2]^2} \cong -\frac{\gamma}{D^4} + \frac{2\gamma r^2}{D^6}. \quad (5)$$

Now, the problem is reduced to an oscillatory solution. As a result, we obtain

$$E_n = -\frac{\gamma}{D^4} + \hbar\omega(n+1), \quad (6)$$

where  $\omega = \frac{2}{D^2} \sqrt{\frac{\gamma}{\mu D^2}}$ . The complete solution to problem (4) requires a numerical calculation. Therefore, for

<sup>1</sup>In this paper, we use the values of all parameters for GaAs/AlGaAs-based QW,  $a_B = 63.8 \text{ \AA}$  and  $\epsilon = 12.86$ .

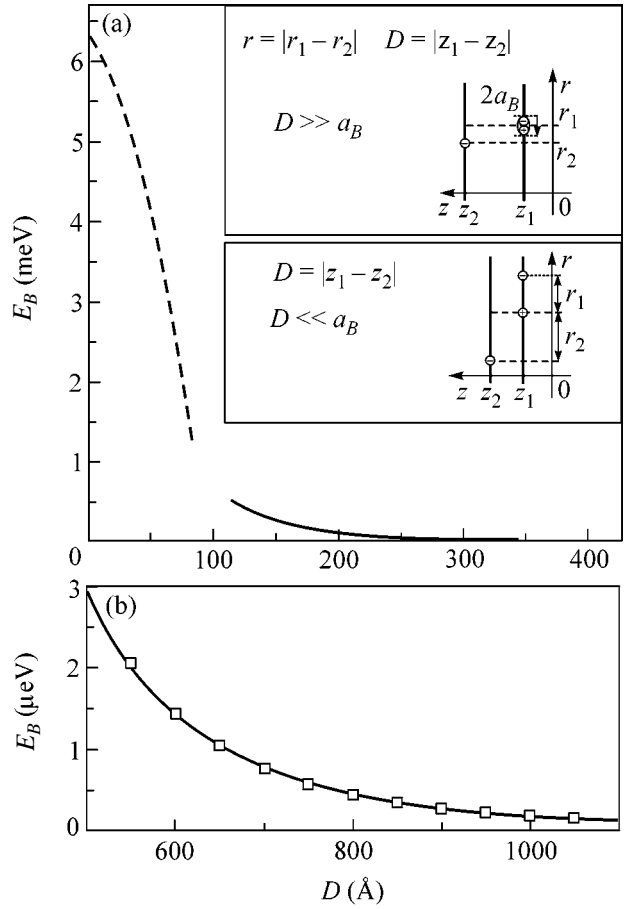


**Fig. 1.** (a) Binding energy  $E_B$  of a trion formed by the spatially separated electron and exciton in a GaAs/AlGaAs-based double-layer system as a function of the layer separation. The solid line refers to the case  $D \gg a_B$ , and the dashed line, to  $D \ll a_B$ . The upper and lower insets schematically represent the system in the cases  $D \gg a_B$  and  $D \ll a_B$ , respectively. (b) The dependence of the trion binding energy on the layer separation for large  $D \gg a_B \rightarrow E_B = \gamma/D^4$ . The dependence is obtained by the numerical calculation (the solid line) and analytically by Eq. (6) (the empty squares).

this differential equation, we use the finite-difference scheme

$$\Psi_{i+1} = \frac{1}{1 + \frac{\Delta r}{r_i}} \left\{ \Psi_i \left( 2 + \frac{\Delta r}{r_i} - (\Delta r)^2 f_i \right) - \Psi_{i-1} \right\}, \quad (7)$$

$$f_i = \frac{2\mu_{\text{tr}}\gamma}{\hbar^2 a_B^2 (r_i^2 + d^2)^2} + \frac{2\mu_{\text{tr}}a_B^2}{\hbar^2} E_B(X^-),$$

$$r_i = \frac{r_i}{a_B}, \quad d = \frac{D}{a_B},$$

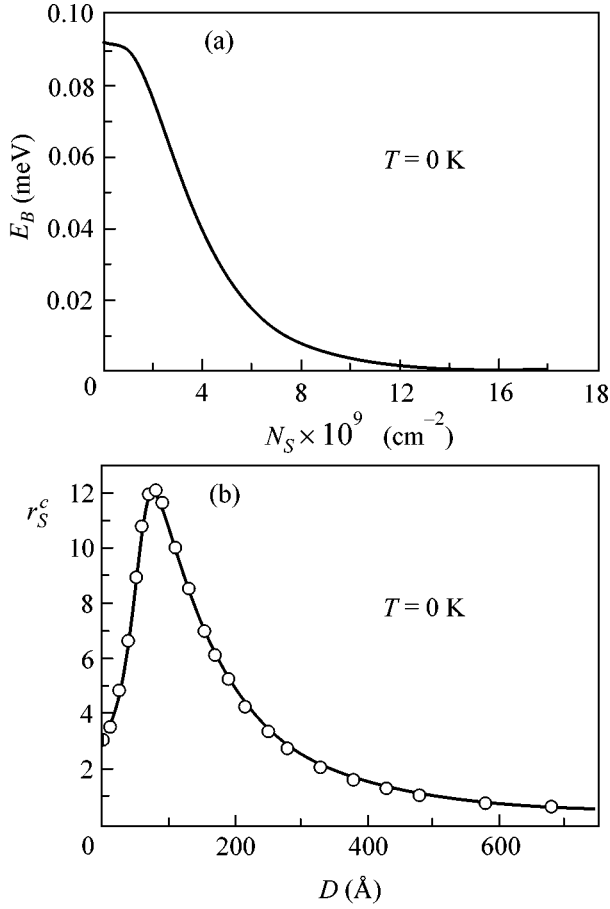


**Fig. 2.** (a) Trion binding energy  $E_B(X^-)$  as a function of the concentration  $N_s$  of the 2D electron gas for the layer separation  $D = 200 \text{ Å}$ . (b) The critical parameter  $r_s^c = 1/a_B \sqrt{2\pi N_s}$ , at which the bound state of the spatially separated exciton and electron (the trion  $X^-$ ) disappears from the spectrum, as a function of the layer separation  $D$ . The screening effects are taken into account in the random phase approximation.

with the initial and boundary conditions (since  $\left. \frac{\partial \Psi}{\partial r} \right|_{r=0} \equiv \frac{\Psi_1 - \Psi_0}{\Delta r} = 0$ , we have  $\Psi_1 = \Psi_0 = 1$ )

$$\Psi_0 = 1, \quad \Psi_1 = 1, \quad \Psi_N = 0. \quad (8)$$

The result of the numerical calculation of the trion binding energy as a function of the layer separation is shown in Fig. 1a (the solid line). The asymptotic behavior of the  $X^-$  binding energy obtained from Eq. (6) is shown in Fig. 1b (the empty squares). One can see that this result agrees well with that obtained from the numerical solution of Eq. (7) (the solid line in Fig. 1b) and confirms that the asymptotic behavior of this dependence has the form of  $1/D^4$  for  $D \rightarrow \infty$ . Using

the known relation  $\langle \partial \hat{H} / \partial \lambda \rangle = \partial E / \partial \lambda$ , where  $\lambda$  is a parameter, we arrive at the inequalities  $\partial E_B(X^-) / \partial D < 0$  and  $\partial^2 E_B(X^-) / \partial D^2 > 0$  for  $D \gg a_B$ . This means that the trion binding energy is a decreasing concave function of  $D$ , which is clearly demonstrated in Fig. 1.

In a many-particle system of excitons and electrons, the bare interaction  $U(r, D)$  should be replaced by the effective one  $U_{\text{eff}}(r, D)$  (the screened interaction). For a two-component system of interacting particles, the effective interaction in the momentum representation has the form

$$U_{\text{eff}}(q, D) = \frac{U(q, D)}{1 + \Pi_1 V_1 + \Pi_2 V_2 + \Pi_1 \Pi_2 (V_1 V_2 - U(q, D)^2)}. \quad (9)$$

Here,  $V_i$  is the energy of interaction between the particles of the  $i$ th kind,  $U(q, D) = -\gamma(\pi q/D) K_1(qD)$  is the Fourier transform of the interaction between an electron and an exciton ( $K_1(z)$  is the Macdonald function of the first kind), and  $\Pi_i$  is the polarization operator for the particles of the  $i$ th kind ( $i = 1, 2$ ). In our case,  $i = 1$  corresponds to excitons and  $i = 2$ , to electrons. When the exciton density is low, i.e.,  $N_1 a_B^2 \ll 1$ , the contribution of electrons to the effective interaction predominates, which allows us to take into account only this interaction in Eq. (9):

$$U_{\text{eff}}(q, D) = \frac{U(q, D)}{1 + \Pi_2 V_2}, \quad (10)$$

where  $\Pi_2 = -(m_e/\pi \hbar^2) [1 - \Theta(q - 2k_F) \sqrt{1 - (2k_F)^2/q^2}]$  is the polarization operator in the random phase approximation at  $T = 0$  [17, 18] ( $k_F = \sqrt{2\pi N_s}$  is the Fermi wave vector) and  $V_2 = 2\pi e^2/\epsilon q$ . Once the expression for the screened potential is determined, we return to Eq. (7). The result of its solution for the screened electron–exciton interaction (10) is the dependence of the trion binding energy on the concentration of the 2D electron gas for the layer separation  $D = 200 \text{ Å}$  (Fig. 2a). One can clearly see that  $E_B(X^-)$  varies in a threshold manner and, for the concentrations of the 2D electron gas  $N_s \sim 10^{10} \text{ cm}^{-2}$ , the bound state of the spatially separated electron and exciton disappears from the spectrum.<sup>2</sup>

<sup>2</sup> Note that the calculation performed for a specific  $D$  does not restrict the generality of the result. For any  $D$  satisfying the condition  $D \gg a_B$ , the results will be similar to those reported here with the only difference that, as the layer separation increases, the 2D electron concentration at which the trion collapses also increases because of the decrease in the efficiency of the screening of this bound state by the electron gas (see, e.g., [19]).

Now, let us consider the case  $D \ll a_B$  (see the lower inset in Fig. 1b). The interaction in the system has the form

$$U(r_1, r_2, \varphi, D) = -\frac{e^2}{\epsilon r_1} - \frac{e^2}{\epsilon \sqrt{r_2^2 + D^2}} + \frac{e^2}{\epsilon \sqrt{r_1^2 + r_2^2 + D^2 - 2r_1 \sqrt{r_2^2 + D^2} \cos \varphi}}, \quad (11)$$

where the first two terms determine the interaction of electrons with the hole and the last term determines the interaction of electrons with each other. We consider this system by analogy with an  $H^-$  atom, in the Born–Oppenheimer approximation. As the zero approximation, we use the Hamiltonian of two noninteracting excitons:

$$\hat{H}_0 = -\frac{\hbar^2}{2\mu} \Delta_{r_1} - \frac{e^2}{\epsilon r_1} - \frac{\hbar^2}{2\mu} \Delta_{r_2} - \frac{e^2}{\epsilon \sqrt{r_2^2 + D^2}}. \quad (12)$$

The solution for a direct exciton is a hydrogen-like spectrum and the corresponding wave functions. Hence, for the ground state (1S), we have

$$\Psi_{1S}(r_1) = \frac{1}{\sqrt{\pi a_B^3}} e^{(-r_1/a_B)}, \quad E_{1S} = -\frac{2\mu e^4}{\hbar^2 \epsilon^2}. \quad (13)$$

We transform the interaction in an indirect exciton by using the small parameter  $D/a_B$ :

$$\begin{aligned} \frac{e^2}{\epsilon \sqrt{r_2^2 + D^2}} &= -\frac{e^2}{\epsilon r_2 \sqrt{1 + \left(\frac{D}{r_2}\right)^2}} \\ &\cong -\frac{e^2}{\epsilon r_2} \left[1 - \frac{D^2}{2r_2^2}\right] = -\frac{e^2}{\epsilon r_2} + \frac{e^2 D^2}{2\epsilon r_2^3}. \end{aligned} \quad (14)$$

Thus, in this case, we can apply perturbation theory. In the zero approximation, we have a hydrogen-like spectrum, as in the case of Eq. (11). To calculate the corrections to the 1S state, it is necessary to perform the procedure of writing the adequate functions of the zero approximation, because all states starting from  $n=2$  are degenerate with respect to the total orbital moment [20]. For the states 2S and 2P, we obtain the following adequate functions of the zero approximation:

$$\Psi_a = c_1^+ \Psi_{2S} + c_2^+ \Psi_{2P}, \quad (15)$$

$$\Psi_b = c_1^- \Psi_{2S} + c_2^- \Psi_{2P} \quad (16)$$

with the energy eigenvalues

$$E_{a(b)} = E_{2S} + \frac{1}{2} [W_{2S,2S} + W_{2P,2P} \pm \Delta W], \quad (17)$$

where

$$c_1 = \left\{ \frac{W_{2S,2P}}{2|W_{2S,2P}|} \left[ 1 \pm \frac{W_{2S,2S} - W_{2P,2P}}{\Delta W} \right] \right\}^{1/2}, \quad (18)$$

$$c_2 = \pm \left\{ \frac{W_{2P,2S}}{2|W_{2S,2P}|} \left[ 1 \mp \frac{W_{2S,2S} - W_{2P,2P}}{\Delta W} \right] \right\}^{1/2}, \quad (19)$$

$$\Delta W = \sqrt{(W_{2S,2S} - W_{2P,2P})^2 + 4|W_{2S,2P}|^2}, \quad (20)$$

$$W_{ij} = \frac{2\pi e^2 D^2}{2\epsilon} \int \Psi_i(r) \frac{1}{r^3} \Psi_j(r) r dr, \quad (21)$$

and, specifically,

$$W_{1S,1S} = \frac{e^2 D^2}{\epsilon} \times \frac{[a_B - 2a \text{Ei}(1, 2a/a_B) e^{(2a/a_B)}] e^{(-2a/a_B)}}{aa_B^4},$$

$$W_{2S,2S} = \frac{e^2 D^2}{8\epsilon} \times \frac{[a_B - 2a \text{Ei}(1, 2a/a_B) e^{(a/a_B)} + a/4] e^{(-a/a_B)}}{aa_B^4},$$

$$W_{2S,2P} = \frac{e^2 D^2}{8\sqrt{12}\epsilon} \times \frac{[\text{Ei}(1, 2a/a_B) e^{(a/a_B)} - 1/2] e^{(-a/a_B)}}{a_B^4},$$

$$W_{2P,2P} = \frac{e^2 D^2 e^{(-a/a_B)}}{96\epsilon a_B^4}.$$

Here,  $a \approx 1.37D$  is the radius beyond which our approximation is effective, this radius being obtained from the comparison of the perturbation  $e^2 D^2 / 2\epsilon r^3$  with the initial potential  $[-e^2 / \epsilon \sqrt{r^2 + D^2}]$ , and  $\text{Ei}(m, x) = \int_1^\infty \frac{e^{-xt}}{t^m} dt$

is the exponential integral [21]. As an example, we present the values of the above matrix elements for the layer separation  $D = 20 \text{ \AA}$ :  $W_{1S,1S} = 11.54 \mu\text{eV}$ ,  $W_{2S,2S} = 1.24 \mu\text{eV}$ ,  $W_{2S,2P} = 0.32 \mu\text{eV}$ , and  $W_{2P,2P} = 0.18 \mu\text{eV}$ . Restricting our consideration to the corrections from the nearest two levels  $\Psi_a$  and  $\Psi_b$ , which in the given conditions is a fair approximation,<sup>3</sup> we obtain the fol-

<sup>3</sup> Such a consideration is possible, because the higher states appear with the weighting factors satisfying the condition  $W_{1S,a}/\Delta E_{1S,a} \gg W_{1S,n}/\Delta E_{1S,n}$  for  $n \geq 3$  and, hence, introduce corrections of a higher order of smallness.

lowing expressions for the wave function and energy of the indirect exciton:

$$\tilde{\Psi} = \Psi_{1S} + \frac{W_{1S,a}}{\Delta E_{1S,a}} \Psi_a + \frac{W_{1S,b}}{\Delta E_{1S,b}} \Psi_b, \quad (22)$$

$$\tilde{E} = E_{1S} + W_{1S,1S}. \quad (23)$$

Here,  $\Delta E_{1S,a(b)} = E_{a(b)} - E_{1S}$  [see Eqs. (11), (15), (18), and (19)]. Thus, for a spatially indirect trion, as the zero-approximation function belonging to the energy  $E_{1S} + \tilde{E}$ , we take

$$\Psi_{\text{tr}}^{(0)}(r_1, r_2) = \Psi_{1S}(r_1) \tilde{\Psi}(r_2). \quad (24)$$

To the first order of the perturbation theory, the energy level of a perturbed system is determined by the formula

$$E(X^-) = E_{1S} + \tilde{E} + \langle \Psi_{\text{tr}}^{(0)} | U_{e-e} | \Psi_{\text{tr}}^{(0)} \rangle, \quad (25)$$

where

$$\langle \Psi_{\text{tr}}^{(0)} | U_{e-e} | \Psi_{\text{tr}}^{(0)} \rangle = \frac{2\pi e^2}{\epsilon} \times \int \frac{|\Psi_{1S}(r_1)|^2 |\tilde{\Psi}(r_2)|^2 r_1 r_2 dr_1 dr_2 d\varphi}{\sqrt{r_1^2 + r_2^2 + D^2 - 2r_1 r_2 \cos(\varphi)}}.$$

As a result, for the trion binding energy at  $D \ll a_B$ , we obtain the expression

$$E_B(X^-) = \frac{2\mu e^4}{\hbar^2 \epsilon^2} - W_{1S,1S} - \langle \Psi_{\text{tr}}^{(0)} | U_{e-e} | \Psi_{\text{tr}}^{(0)} \rangle,$$

which yields the dependence shown in Fig. 1a (the dashed line). When  $D \rightarrow 0$ , the value of  $E_B(X^-)$  tends to the binding energy of a two-dimensional trion [22, 23]. In the region  $60 \text{ \AA} \geq D \geq 120 \text{ \AA}$ , sewing together with the solution obtained for  $D \gg a_B$  requires numerical modeling with the initial potential given by Eq. (11). This calculation is rather cumbersome and of no interest in the framework of this paper. Therefore, it may be described in another publication.

The last issue that will be considered in this paper is the screening of the electron–hole and electron–electron interactions in a many-particle electron system for small values of the layer separation. Since in this region we considered the system as two weakly interacting excitons, the renormalization of potentials primarily refers to the exciton-forming interactions. Thus, the object of our interest is the screening of a direct exciton by the 2D electron gas located in the other layer, as well as the screening of a spatially indirect exciton. Both these problems were considered in [24] where the dependences of the dimensionless critical parameters  $r_s^c$  on the layer separation were determined. Combining the results obtained for different values of  $D$ , we can construct a unified picture (Fig. 2b) for the critical

parameter  $r_s^c$ , which corresponds to the disappearance of the bound state of the spatially separated exciton and electron from the spectrum of collective excitations. In Fig. 2b, one can see a decrease followed by an increase in the threshold concentration of the 2D electron gas. This behavior, as in [24], is related to the competition between two mechanisms. Namely, an increase in the layer separation is accompanied by a decrease in the initial electron–hole interaction and by a simultaneous decrease in the efficiency of the screening of the hole by spatially separated electrons.

Thus, in this paper, we solved the problem on the bound state of the spatially separated exciton and electron, i.e., a trion  $X^-$ . We studied the behavior of this system in two limiting cases:  $D \gg a_B$  and  $D \ll a_B$ . In the first case, the problem was solved by analogy with the bound state of  $H^-$  in the Born–Oppenheimer approximation. In the second case, we considered the exciton–electron interaction as the interaction of an electron with a dipole, which is a fair approximation when the exciton size is much smaller than the exciton–electron distance. We determined the trion binding energy for different layer separations. We also considered the screening of the bound state under investigation by the 2D electron gas. As a result, we constructed the dependence of the critical parameter  $r_s^c$ , which corresponds to the disappearance of the bound state of the spatially separated exciton and electron from the collective excitation spectrum, on the layer separation  $D$ . Summarizing the results of this study, we anticipate that, at low temperatures ( $T < E_B(X^-)$ ), this bound state can be studied experimentally. For example, in transport measurements, the presence of a spatially indirect trion will lead to a decrease in the mobility of the electron subsystem, because the mass of the trion center of mass in the plane is much greater than the mass of a free electron.

This work was supported by the Russian Foundation for Basic Research and the INTAS.

## REFERENCES

1. R. S. Knox, *Theory of Excitons* (Academic, New York, 1963), Solid State Physics, Supplement 5.
2. R. J. Elliott, *Polarons and Excitons* (Edinburgh–London, 1963); Phys. Rev. **124**, 340 (1961).
3. R. J. Elliott and R. Loudon, J. Phys. Chem. Solids **8**, 382 (1959).
4. L. P. Gor'kov and I. E. Dzyaloshinskiĭ, Zh. Éksp. Teor. Fiz. **52**, 717 (1967) [Sov. Phys. JETP **26**, 449 (1968)].
5. M. A. Lampert, Phys. Rev. Lett. **1**, 450 (1958).
6. J. J. Palacios, D. Yoshioka, and A. H. MacDonald, Phys. Rev. B **54**, R2296 (1996).
7. A. B. Dzyubenko and A. Yu. Sivachenko, Phys. Rev. Lett. **84**, 4429 (2000).
8. A. B. Dzyubenko, Phys. Rev. B **65**, 38318 (2002).
9. O. Homburg, K. Sebal, P. Michler, *et al.*, Phys. Rev. B **62**, 7413 (2000).

10. C. Riva, F. M. Peeters, and K. Varga, *Phys. Rev. B* **61**, 13873 (2000).
11. A. Esser, E. Runge, R. Zimmermann, and W. Langbein, *Phys. Status Solidi B* **221**, 281 (2000).
12. B. Stébé, G. Munsch, L. Stauffer, *et al.*, *Phys. Rev. B* **56**, 12454 (1997).
13. V. P. Kochereshko, G. V. Astakhov, *et al.*, *Phys. Status Solidi B* **220**, 345 (2000).
14. V. S. Babichenko and M. N. Kiselev, *J. Phys. Soc.* **2**, 311 (1992).
15. V. S. Babichenko and M. N. Kiselev, *Pis'ma Zh. Éksp. Teor. Fiz.* **57**, 174 (1993) [*JETP Lett.* **57**, 179 (1993)].
16. Yu. E. Lozovik and M. V. Nikitkov, *Zh. Éksp. Teor. Fiz.* **112**, 1791 (1997) [*JETP* **85**, 979 (1997)].
17. F. Stern, *Phys. Rev. Lett.* **18**, 546 (1967).
18. Lian Zheng and A. H. MacDonald, *Phys. Rev. B* **49**, 5522 (1994).
19. D. V. Kulakovskii, S. I. Gubarev, and Yu. E. Lozovik, *Zh. Éksp. Teor. Fiz.* **121** (4), 915 (2002) [*JETP* **94**, 785 (2002)].
20. L. D. Landau and E. M. Lifshitz, *Course of Theoretical Physics*, Vol. 3: *Quantum Mechanics: Non-Relativistic Theory* (Nauka, Moscow, 1989, 4th ed.; Pergamon, New York, 1977, 3rd ed.).
21. I. S. Gradshteyn and I. M. Ryzhik, *Table of Integrals, Series, and Products* (Nauka, Moscow, 1971; Academic, New York, 1980).
22. A. I. Bobrysheva, M. V. Grodetskii, and V. T. Zyukov, *J. Phys. C* **16**, 5723 (1983).
23. A. Thilagam, *Phys. Rev. B* **55**, 7804 (1997).
24. D. V. Kulakovskii and Yu. E. Lozovik, *Zh. Éksp. Teor. Fiz.* (in press) [*JETP* (in press)].

*Translated by E. Golyamina*

# Fullerene C<sub>60</sub> Formation in Partially Ionized Carbon Vapor

G. N. Churilov, A. S. Fedorov, and P. V. Novikov

Kirenskii Institute of Physics, Siberian Division, Russian Academy of Sciences,  
Akademgorodok, Krasnoyarsk, 660036 Russia

e-mail: churilov@iph.krasn.ru

Received July 24, 2002; in final form, September 23, 2002

The assembling rate of a fullerene C<sub>60</sub> molecule has been theoretically studied as a function of electron concentration and temperature in partially ionized carbon vapor. For C<sub>60</sub> formation via one or two intermediate stages of cluster collisions, it has been shown that there is a region of plasma parameters (the temperature and electron concentration) in which fullerene C<sub>60</sub> is formed more efficiently. The C<sub>60</sub> formation rate versus temperature and electron concentration relationships have been found to correlate with the trends in the collision cross-section of carbon clusters as functions of these parameters. © 2002 MAIK “Nauka/Interperiodica”.

PACS numbers: 52.27.Lw; 52.20.Hv; 36.40.Gk

Numerous studies are known to concern fullerene formation upon condensation of carbon vapor, but the mechanism of formation is not fully clear [1]. Fullerene formation is, as a rule, considered in electroneutral carbon vapor and not in carbon-containing plasma. Therefore, the role of the carbon-cluster charge in cluster joining was ignored, although it is known from experiments that charged particles affect fullerene formation [2]. Alekseev and Dyuzhev [3] considered the effect of carbon-cluster charge on carbon-structure formation. They inferred that plasma parameters affect the spatial cluster-charge distribution in the plasma jet and the conditions for plasma discharge. However, the effect of the cluster charge on the fullerene formation rate has not been touched in that study.

Our purpose in this work was to quantify the effect of the carbon-cluster charge on the formation rate of fullerene C<sub>60</sub> as a function of the electron concentration and temperature of carbon–helium plasma. We have shown that the charge on carbon clusters (which substantially changes the collision cross-section of clusters and, in association, the fullerene formation rate) should be included into the consideration of fullerene formation. The cluster charge is a function of electron concentration  $n_e$  and temperature  $T$  in plasma. The  $n_e$  and  $T$  parameters were believed to be independent of each other in the calculations of the carbon subsystem. Although the plasma parameters should be calculated self-consistently, doping the plasma with small amounts of electron donors (acceptors) is an efficient means for changing the electron concentration at a given temperature; thus these parameters become in fact independent of each other. Particular routes of C<sub>60</sub> assembling and C<sub>60</sub> isomerization to yield fullerene were beyond the scope of this study; these points have been considered elsewhere.

One of the basic postulates that are employed in most studies dealing with fullerene formation in plasma arc is that the plasma is considered as occurring in the state of local thermodynamic equilibrium. If this is the case, Saha's equations are applicable to determine cluster-charge distribution in partially ionized carbon vapor for different values of electron concentration  $n_e$  and temperature  $T$ . The calculations were applied to the carbon–helium plasma under atmospheric pressure (with 10<sup>2</sup> Pa partial carbon pressure) for the temperature range 1500–5000 K; the range of fullerene formation temperatures falls within this range [4]. We ignored a reduction in the fullerene formation rate at lower temperatures caused by decreases in the carbon evaporation rate and the cluster-isomerization rate. Taking this factor into account would have reduced the relationship for the fullerene appearance rate at lower temperatures of  $T < 2000$  K (Figs. 2, 3).

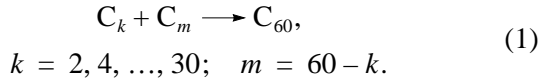
We assumed that the fullerene C<sub>60</sub> yield is proportional to the formation rate of fullerene molecules. This assumption might be proven by the fact that fullerene molecules are stable and have high bond energies, and their transformation to other clusters (having another mass) is inessential compared to their formation. To find the cluster-collision frequency, the scattering cross-sections derived from classical collision theory were used. Classical theory is useful for finding the scattering cross-sections due to the fact that carbon clusters have large masses compared to the electron mass. The ionization potentials and electron affinities of carbon clusters were found from *ab initio* quantum-chemical calculations.

A null activation barrier to the joining reaction of any clusters was assumed in the calculations; that is, the collision of any two clusters C<sub>*k*</sub> and C<sub>*m*</sub> resulted in the appearance of cluster C<sub>*k+m*</sub>. This assumption is based

on the common chemical character of colliding clusters, which leads to small variations in the activation barrier. Another base is the fact that, upon averaging the colliding clusters with respect to their shape and mutual position, the barriers of joining reactions should tend to a constant value. Any fixed barrier to joining for all clusters cannot change the results of the calculation apart from introducing a common normalizing factor. For simplicity, this factor was ignored.

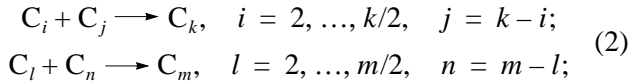
Only reactions between clusters containing an even number of atoms were included into the calculations; in experiments [5], the mass-spectrometric analysis of carbon clusters during fullerene formation showed that even-atom clusters in plasma are several orders of magnitude more abundant than odd-atom clusters.

We considered the final process of C<sub>60</sub> assembling in one and two reaction stages. In the one-stage process, reactions between all possible pairs of carbon clusters that result in molecule C<sub>60</sub> were considered. Clearly, the sum of the masses of colliding clusters is equal to the mass of molecule C<sub>60</sub>:

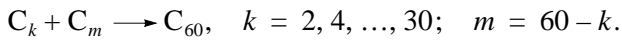


In the two-stage process, in addition to all reactions of C<sub>60</sub> formation from clusters C<sub>k</sub> and C<sub>m</sub>, all reactions that yield these clusters C<sub>k</sub> and C<sub>m</sub> were considered.

For stage 1:



For stage 2:



Introduction of the cluster-size distribution function was an important point of the calculations. Several distribution functions were used. The basic distribution used corresponded to the cluster-mass distribution from [6]. The other two distributions were chosen from [7]. For all of the distributions used, the C<sub>60</sub> formation rate versus electron concentration and versus temperature relationships were the same. Therefore, the data derived are applicable to an experiment in which the cluster distribution function is not steady-state.

The focus of our approach is the calculation, from gas theory [9], of the rate  $R_{km}(q_k, q_m)$  of the collision (that results in joining) of two clusters C<sub>k</sub> and C<sub>m</sub> bearing charges  $q_k$  and  $q_m$ , respectively:

$$R_{km}(q_k, q_m) = n_m(q_m)n_k(q_k)v_{km}\sigma_{km}(q_k, q_m). \quad (3)$$

Here,  $n_m(q_m)$  and  $n_k(q_k)$  are the concentrations of clusters C<sub>k</sub> and C<sub>m</sub> that bear charges  $q_k$  and  $q_m$ ,  $v_{km} = \sqrt{8k_B T / \pi m_{km}}$  is the mean rate of the relative movement of these clusters,  $m_{km} = m_k m_m / (m_k + m_m)$  is the normal-

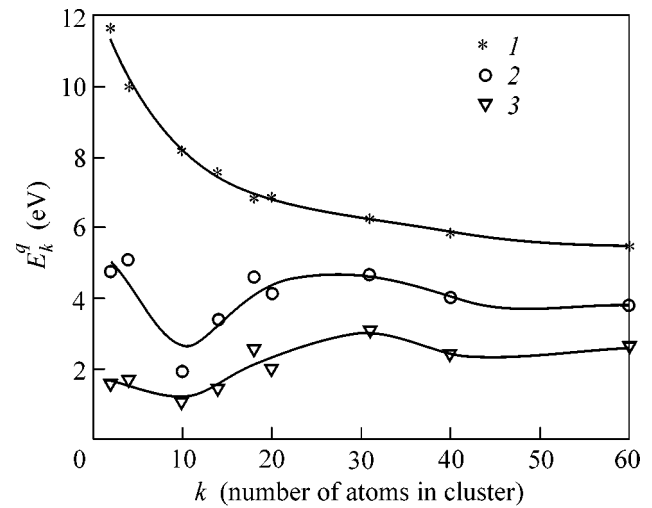


**Fig. 1.** Plots of (1) the ionization potential  $E_k^0$ , (2) electron affinity  $-E_k^{-1}$ , and (3) electron affinity of the anion  $-E_k^{-2}$  for the carbon clusters used in the calculations.

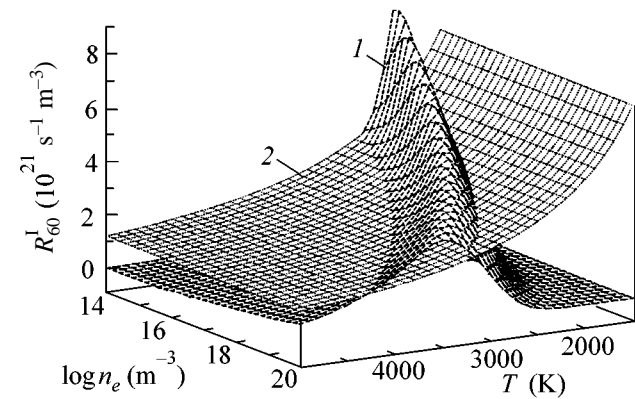


**Fig. 2.** Plots of (1) the fullerene C<sub>60</sub> formation rate in one stage and (2) C<sub>60</sub> formation rate in one stage from neutral clusters.

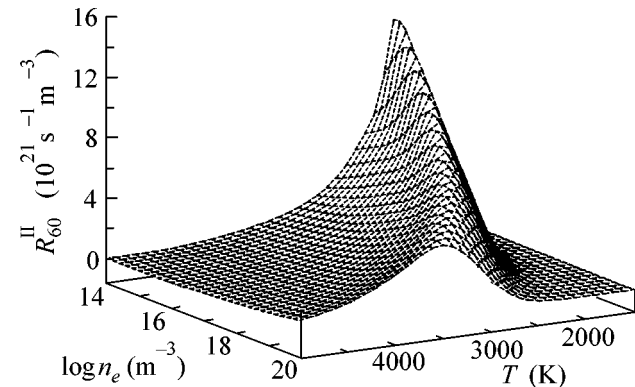


**Fig. 3.** Fullerene C<sub>60</sub> formation rate in the two-stage process.

ized mass of the clusters, and  $\sigma_{km}(q_k, q_m)$  is the collision cross-section of these particles.

From classical collision theory, the effective collision cross-section of charged particles [10] is defined as

$$\sigma_{km}(q_k, q_m) = \sigma_{km}^0 \left( 1 - \frac{q_k q_m e^2}{r_{km} \epsilon_{kin}} \right). \quad (4)$$

Here,  $\sigma_{km}^0 = \pi r_{km}^2$  is the collision cross-section of neutral clusters  $C_k$  and  $C_m$ ,  $r_{km} = r_k + r_m$  is the impact distance between two clusters, and  $q_k q_m e^2 / r_{km} \epsilon_{kin}$  is the ratio of the electrostatic and mean kinetic energies  $\epsilon_{kin} = 3/2 k_B T$  of the relative cluster movement.

The effective radius  $r_k$  of cluster  $C_k$  was always set equal to  $r_k = 1/2(d_x d_y d_z)^{1/3}$ , a value equal to one-half cube root of the product of the three maximal dimensions  $d_x$ ,  $d_y$ , and  $d_z$  of the cluster. This distance was calculated for the basis set of clusters of different sizes and shapes:  $C_2$  and  $C_4$  are chains,  $C_{10}$  is a ring,  $C_{14}$  and  $C_{18}$  are planar clusters composed of hexagons,  $C_{20}$  is a cup shaped as a coranulene molecule,  $C_{32}$  is a cup composed of pentagons and hexagons,  $C_{40}$  is a cup, fullerene, and fullerene with a heptagon, and  $C_{60}$  is a fullerene and a fullerene with a heptagon [7, 11]. The clusters containing heptagons were included into the calculation because of the important role they play in fullerene formation [8]. For the other clusters  $C_k$  with  $k = 2, \dots, 60$ , radius  $r_k$  was calculated using interpolation of the  $r_k$  of the basis set.

From the relationship above, it is clear that for charges of opposite signs ( $q_1 q_2 < 0$ ), there exists additional attraction between clusters:  $\sigma_{12} > \sigma_0$ , but for similar charges ( $q_1 q_2 > 0$ ) the collision cross-section is smaller:  $\sigma_{12} < \sigma_0$ . When the Coulombic repulsion of two clusters surpasses the kinetic energy of both clusters ( $q_k q_m e^2 / r_{km} \epsilon_{kin} > 1$ ), no collision occurs; in this case,  $\sigma_{12} = 0$ .

It is worth noting that, in view of the high C–C bond energy ( $E_{C-C} = 6.24$  eV), the cluster-dissociation frequency  $\nu_{diss}$  is insignificant with respect to the cluster-joining frequency  $\nu_{join}$ . The cluster-joining frequency in our calculations is estimated at  $\nu_{join} = 10^5$  s<sup>-1</sup>. The dissociation frequency can be estimated from  $\nu_{diss} = \nu_{vib} f(T) \exp(-E/k_B T)$  [12], where  $\nu_{vib}$  is the characteristic vibrational frequency of the cluster (equal to  $10^{11}$  to  $10^{12}$  s<sup>-1</sup>),  $E = N E_{C-C}$  is the activation barrier to cluster dissociation ( $N$  is the number of dissociating bonds), and  $f(T)$  for molecules is  $10^2$ – $10^3$ . For example, given two C–C bonds dissociate, the cluster dissociation frequency is  $\nu_{diss} \approx 10^{-2}$  s<sup>-1</sup>. In view of the above data, cluster dissociation was ignored in the calculations.

The full rate of cluster  $C_{k+m}$  formation from clusters  $C_k$  and  $C_m$  was determined as the sum of the reaction

rates between these clusters with all possible charges:

$$R_{km} = \sum_{q_m = -2}^{+1} \sum_{q_k = -2}^{+1} R_{km}(q_m, q_k). \quad (5)$$

Charges of  $q_i = \{-2, -1, 0, 1\}$  were used for all of the clusters considered; the calculations showed that, for all clusters from the basis set, the affinity for the third electron was negative and the second ionization potential was too high. For example, for ring cluster  $C_{10}$ , coranulene-type cluster  $C_{20}$ , and fullerene  $C_{60}$ , the second ionization potential was 19.85, 19.60, and 17.06 eV, respectively. Therefore, the existence probability of clusters with charges higher than +1 or lower than -2 in plasma discharge is negligible.

Charge distributions  $p_k(q)$  for each cluster  $C_k$ , which show the existence probability of cluster  $C_k$  with charge  $q$ , were defined from Saha's equations

$$\frac{p_k(q+1)n_e}{p_k(q)} = 2a(T) \frac{Z_k^{q+1}}{Z_k^q} \exp\left(-\frac{E_k^q}{k_B T}\right), \quad (6)$$

Here  $a(T) = (m_e k T / 2\pi \hbar^2)^{3/2}$ ,  $n_e$  is the plasma electron concentration,  $E_i^q$  is the ionization potential of cluster  $C_{k+m}^q$ ,

$$Z_k^q(T) = \sum_{n=1}^{n_{max}} g_n \exp\{-(\epsilon_n - \epsilon_1)/k_B T\}$$

is the electron partition function for cluster  $C_k$  with charge  $q$  at temperature  $T$ , and  $g_n$  is the degeneration multiplicity of the electron level  $\epsilon_n$  of cluster  $C_k$ .

Imposing the normalization condition  $p_k(-2) + p_k(-1) + p_k(0) + p_k(+1) = 1$ , the equilibrium concentrations of clusters  $C_k$  with different charges are

$$n_k(q) = n_k p_k(q), \quad q = -2, -1, 0, +1. \quad (7)$$

The mean charge on cluster  $C_k$  in the plasma with electron concentration  $n_e$  and temperature  $T$  was defined from

$$\langle q_k \rangle = \frac{1}{n_k} \sum_{q=-2}^{+1} q n_k(q) = \sum_{q=-2}^{+1} q p_k(q). \quad (8)$$

With this, the overall formation rate  $R_{km}$  (5) of cluster  $C_{k+m}$  upon joining of two other clusters  $C_k$  and  $C_m$  can be expressed as the product of two values, one being a function of cluster charges and the other being not:  $R_{km} = R_{km}^0 P_{km}$ , where  $R_{km}^0 = n_m n_k \nu_{km} \sigma_{km}^0$  is the reaction rate in the case where all clusters are electroneutral, and

$$P_{km} = \sum_{q_m = -2}^{+1} \sum_{q_k = -2}^{+1} p_m(q_m) p_k(q_k) \left( 1 - \frac{q_k q_m e^2}{r_{km} \epsilon} \right). \quad (9)$$

The existing unknown values of ionization potentials  $E_k^0$ , electron affinity  $-E_k^{-1}$ , and electron affinity of the anion  $-E_k^{-2}$  for each cluster  $C_k$  from  $C_2$  to  $C_{58}$  were calculated using interpolation of energies  $E_k^q$  for the basis set of clusters (Fig. 1). Energies  $E_k^q$  for clusters  $C_{40}$  and  $C_{60}$  from the basis set were found by averaging over their isomers.

The VASP program package [13, 14] was used to calculate energies  $E_k^q$ . In this *ab initio* package, in terms of density functional theory (DFT), the plane-wave expansion of wavefunctions and Vanderbilt's pseudopotential [15] for each atom are used, which abruptly speeds up the calculation of the full energy of the system.

From the equations above, one can calculate the assembling rate of a fullerene  $C_{60}$  molecule. The rate of the one-stage process (1) of fullerene  $C_{60}$  formation was found by summation of rates (5) over all  $k$  and  $m$ :

$$R_{60}^I = \sum_{k=2}^{30} R_{k,60-k}. \quad (10)$$

The one-stage assembling rate of  $C_{60}$  at different electron densities and temperatures is imaged by surface 1 in Fig. 2. Surface 2 in the same figure refers to a one-stage process with charges ignored. A fundamental difference is seen to exist between the assembling rates from neutral and charged clusters.

The two-stage assembling rate (process (2)) is mapped in Fig. 3. In mapping, additional concentrations of various clusters  $C_k$  accumulated during the period of time  $\tau = 10^{-5}$  s (chosen to be equal to the mean collision time of carbon clusters with one another) were taken into account:

$$\Delta n_k = \sum_{i+j=k} R_{ij}\tau.$$

Then, in the first order of  $\Delta n_m$  and with  $\Delta n_m \Delta n_k$  terms ignored, the overall two-stage  $C_{60}$  assembling rate is calculated as

$$R_{60}^{II} = R_{60}^I + \sum_{m+k=60} (\Delta n_m n_k + n_m \Delta n_k) v_{km} \sigma_{km}^0 P_{km}. \quad (11)$$

From the similarity of relationships for the assembling rates in one stage (Fig. 2, surface 1) and two stages (Fig. 3), we believe that a similar relationship holds for many (more than two) joining stages. Therefore, the general relationship between the  $C_{60}$  assembling rate and the plasma parameters is expected to be similar to Figs. 2 and 3.

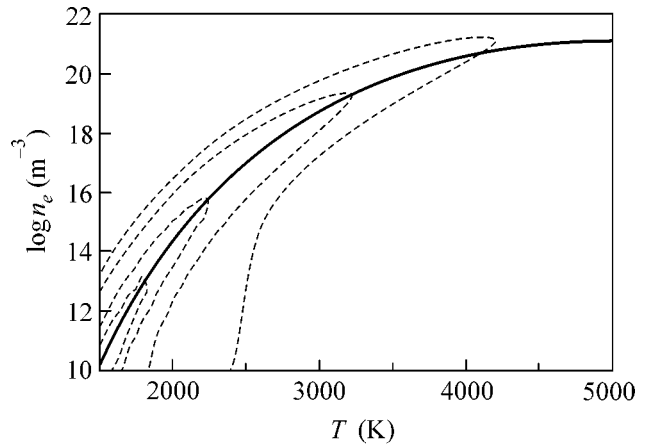


Fig. 4. Plots of the electron concentration vs. temperature for pure carbon-helium plasma  $n_e(T)$  and the envelope plot of the one-stage  $C_{60}$  formation rate.

Figures 2 and 3 make it clear that, for different temperatures, a peak in the  $C_{60}$  formation rate is observed at different electron concentrations. For example, at  $T \sim 2000$  K the peak is observed at  $n_e \sim 10^{14} \text{ m}^{-3}$ ; to  $T \sim 2500$  K,  $n_e \sim 10^{17} \text{ m}^{-3}$  corresponds; and so on.

From the constraint of the self-consistency of the electron concentration and carbon-cluster charges, electron concentration  $n_e(T)$  in carbon-helium plasma was calculated for different temperatures (Fig. 4), that is, in the absence of any other source of electrons or ions other than carbon clusters.

In addition to the plot of self-consistent electron concentration, Fig. 4 shows equal-value lines for the one-stage  $C_{60}$  assembling rate (Fig. 2, surface 1). Figure 4 makes it clear that the peak  $C_{60}$  assembling rate at some temperature corresponds to the electron concentration of pure carbon-helium plasma at this temperature. From this correspondence, the following important inference can be made: the maximal fullerene yield in the arc-plasma discharge is achievable precisely in pure carbon-helium plasma free of any electron donors or acceptors.

The existence of optimal plasma parameters for  $C_{60}$  synthesis can be explained by the strong dependence of the mean carbon-cluster charge on temperature. This dependence is illustrated by Fig. 5.

$$n_e(T) = \sum_m \sum_{q_m=-2}^{+1} n_m(q_m), \quad (12)$$

where  $n_m(q_m)$  is the concentration of carbon clusters  $C_m$  that carry charge  $q_m$ , which is a function of  $n_e$  and  $T$ .

For the temperature and electron concentration that correspond to the maximal  $C_{60}$  assembling rate, the charges on clusters  $C_2$  and  $C_{58}$  are high enough and have opposite signs (for  $T \sim 2000$  K and  $n_e \sim 10^{14} \text{ m}^{-3}$ ,

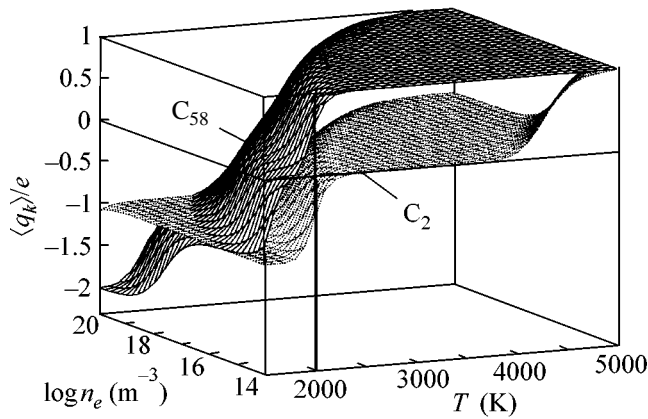


Fig. 5. Charges on clusters  $C_2$  and  $C_{58}$ .

the charges are  $-0.5$  and  $+0.6$ , respectively). As a result, the collision rate of these clusters is several times higher than in adjacent domains, and the  $C_{60}$  assembling rate increases in association.

This work was financially supported by the INTAS grant no. 01-2399, the State Scientific and Engineering Program "Topical Lines of Research in Condensed Matter Physics" (project no. 5-3-00), and the Program "Priority Scientific and Engineering Research in Higher Education Institutions" (project no. 05.01.001).

#### REFERENCES

1. Yu. E. Lozovik and A. M. Popov, *Usp. Fiz. Nauk* **167**, 751 (1997) [*Phys. Usp.* **40**, 717 (1997)].

2. D. V. Afanas'ev, G. A. Dyuzhev, and V. I. Karataev, *Pis'ma Zh. Tekh. Fiz.* **25** (5), 35 (1999) [*Tech. Phys. Lett.* **25**, 182 (1999)].
3. N. I. Alekseev and G. A. Dyuzhev, *Zh. Tekh. Fiz.* **69** (12), 42 (1999) [*Tech. Phys.* **44**, 1435 (1999)].
4. N. A. Vatolin, E. A. Kibanova, and V. A. Polukhin, *Dokl. Akad. Nauk* **356**, 57 (1997).
5. D. M. Cox, K. C. Reichmann, and A. Kaldor, *J. Chem. Phys.* **88**, 1588 (1988).
6. O. A. Nerushev and G. I. Sukhinin, *Zh. Tekh. Fiz.* **67** (2), 41 (1997) [*Tech. Phys.* **42**, 160 (1997)].
7. G. N. Churilov, A. S. Fedorov, and P. V. Novikov, *Carbon* (in press).
8. E. Hernandez, P. Ordejon, and H. Terrones, *Phys. Rev. B* **63**, 193403 (2001).
9. M. Mitchner and C. H. Kruger, Jr., *Partially Ionized Gases* (Wiley, New York, 1973; Mir, Moscow, 1976).
10. L. D. Landau and E. M. Lifshitz, *Course of Theoretical Physics, Vol. 1: Mechanics* (Nauka, Moscow, 1973; Pergamon, New York, 1988).
11. G. N. Churilov, P. V. Novikov, V. E. Taraban'ko, *et al.*, *Carbon* **40**, 891 (2002).
12. P. A. Redhead, *Vacuum* **12**, 203 (1962).
13. G. Kresse and J. Furthmuller, *Comput. Mater. Sci.* **6**, 15 (1996).
14. G. Kresse and J. Furthmuller, *Phys. Rev. B* **54**, 11169 (1996).
15. D. Vanderbilt, *Phys. Rev. B* **41**, 7892 (1990).

Translated by O. Fedorova

# Magnetization-Induced Second Harmonic Generation in Magnetophotonic Microcavities Based on Ferrite Garnets

A. A. Fedyanin<sup>1</sup>, T. Yoshida<sup>2</sup>, K. Nishimura<sup>2</sup>, G. Marowsky<sup>3</sup>,  
M. Inoue<sup>2</sup>, and O. A. Aktsipetrov<sup>1,\*</sup>

<sup>1</sup>*Moscow State University, Vorob'evy gory, Moscow, 119992 Russia*

\* *e-mail: aktsip@shg.ru*

<sup>2</sup>*Toyohashi University of Technology, 441-8580 Toyohashi, Japan*

<sup>3</sup>*Laser-Laboratorium Göttingen, D-37077 Göttingen, Germany*

Received September 25, 2002

Magnetization-induced second harmonic generation was observed in magnetophotonic microcavities consisting of a ferromagnetic yttrium–iron garnet layer surrounded by nonmagnetic photonic crystals (Bragg reflectors). At resonance between the fundamental radiation and the microcavity mode in the geometry of polar magneto-optical Kerr effect, the polarization rotation for the second harmonic was found to be  $(18.5 \pm 0.5)^\circ/\mu\text{m}$  for the fundamental radiation with a wavelength of 825 nm. © 2002 MAIK “Nauka/Interperiodica”.

PACS numbers: 42.65.Ky; 42.70.Qs; 75.75.+a

Magnetization-induced second harmonic generation (MSHG) is one of the fundamental phenomena in nonlinear magneto-optics. It is associated with the involvement of the spin subsystem and the spin–orbit interaction in the formation of the electronic quadratic nonlinear optical response of magnets [1]. This phenomenon was used to develop an efficient method of studying magnetic surfaces and thin films [2]. The sensitivity of this method is caused by the symmetry selection rule for MSHG in the bulk of centrosymmetric media; many important magnetic materials belong to such media. Magnetization-induced changes in the parameters of SH radiation such as its amplitude (intensity), polarization, and phase in typical experimental situations prove to be several orders of magnitude larger than in the magneto-optical Kerr effect and the Faraday effect. Since the first observation of MSHG in ferrite garnet films [3] and its theoretical prediction in [4], the magnetization-induced SH was extensively studied at metal surfaces and thin films [5–8], as well as in thin films of magnetic insulators, primarily, of yttrium–iron garnets [9, 10]. In last years, much attention has been given to studying MSHG in magnetic nanoparticles [2, 11, 12].

The methods developed in the last years for manufacturing structures with an artificial photonic band gap {photonic crystals and microcavities (MC) [13]} made it possible to study nonlinear optical phenomena which are associated with the specificity of light propagation in such microstructures [14]. For example, in the case of MC, the spatial localization of resonant electromag-

netic radiation in the vicinity of microcavity layer strengthens the generation of optical harmonics, as was recently observed experimentally for the second and third harmonics in microcavities based on porous silicon [15, 16]. Of special interest is the study of nonlinear optical effects in magnetic microstructures with photonic band gap because of the expected enhancement of their magnetization-induced response. However, methods of growing such objects were developed only recently [17, 18].

In this work, the enhancement of MSHG was studied experimentally in magnetic microcavities based on photonic crystals. A high quality of the nonmagnetic Bragg reflectors grown from silicon oxide and tantalum oxide layers causes strong localization of electromagnetic field in a ferromagnetic yttrium–iron garnet MC layer and enhances the gain in MSHG, which manifests itself in a many-fold amplification of the rotation of SH polarization.

Magnetophotonic MC samples were composed of a half-wave 190-nm-thick bismuth-doped polycrystalline yttrium–iron garnet (Bi:YIG) layer surrounded by two Bragg reflectors consisting of five pairs of alternating quarter-wave  $\text{SiO}_2$  and  $\text{Ta}_2\text{O}_5$  layers 135 and 95 nm in thickness, respectively. The expected spectral position of the microcavity mode in the grown MC was about 850 nm at the normal incidence, and the center of the photonic band gap and its width were about 780 and 200 nm, respectively. When manufacturing MC,  $\text{SiO}_2/\text{Ta}_2\text{O}_5$  photonic crystal was first grown on a fused silica substrate by magnetron sputtering. Then a

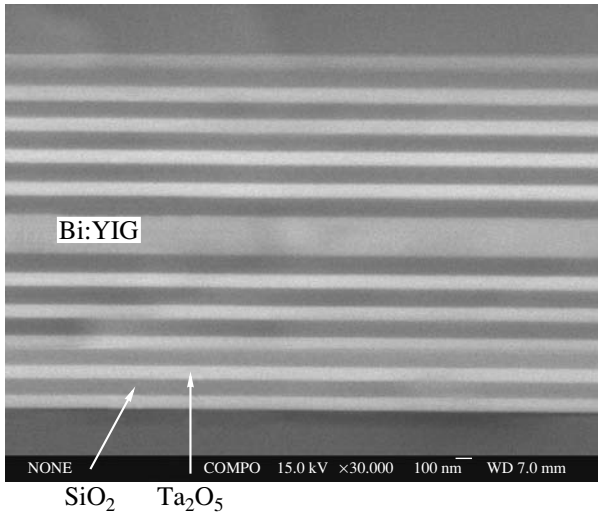


**Fig. 1.** Electron microscope image of the magnetophotonic microcavity cleavage.

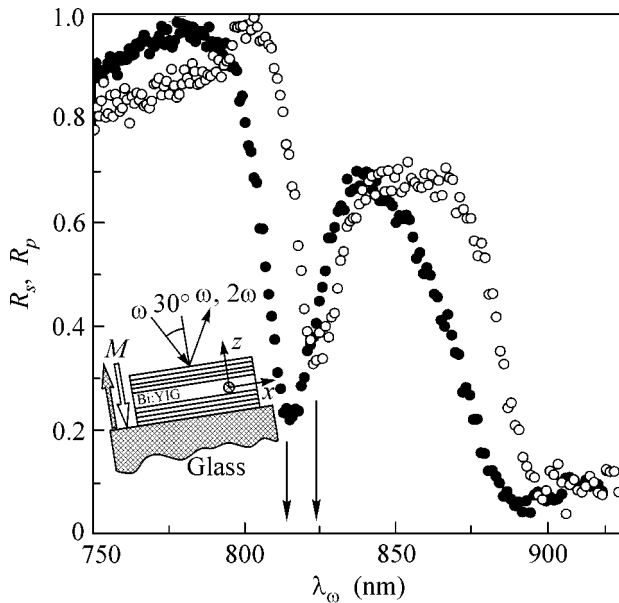


**Fig. 2.** Linear reflection coefficients measured for the  $s$ - and  $p$ -polarized fundamental waves (light and dark circles, respectively) at an angle of incidence of  $30^\circ$ . Arrows indicate spectral positions of the MC mode for these polarizations. Inset: scheme of experimental geometry, applied magnetic field, and the MC frame of reference.

Bi:YIG film was deposited. After annealing at a temperature of  $725^\circ\text{C}$  for 10 min, a polycrystalline ferromagnetic garnet layer was formed. At the final stage, the capping photonic crystal was deposited on the MC garnet layer. The structure of the grown magnetophotonic MC is seen in its electron microscope image

(Fig. 1). It demonstrates a high homogeneity of the layers constituting MC and well-defined interfaces between the layers.

Experiments on MSHG spectroscopy were performed using linearly polarized radiation from an optical parametric oscillator with a pulse duration of about 4 ns and a pulse energy of 5 mJ. The fundamental radiation wavelength was tuned in the range from 750 to 950 nm. The polarization of fundamental radiation was varied by a Fresnel rhomb and monitored by a Glan prism. The polarization of the reflected SH radiation was monitored by another Glan prism. The saturating magnetic field on the order of 2 kOe was applied in the geometry of polar magneto-optical Kerr effect using a permanent magnet made from NdFeB. The SH radiation was separated by a set of glass BG39 filters and detected by a photomultiplier. The angle of incidence of the fundamental radiation on the sample was  $30^\circ$ .

The spectra of the coefficients  $R_s$  and  $R_p$  of linear reflection from a magnetophotonic MC for the  $s$ - and  $p$ -polarized radiation in the vicinity of the MC mode are shown in Fig. 2. For wavelengths shorter than 900 nm, both spectra demonstrate high reflectance corresponding to the photonic band gap. A dip in the reflection spectrum at  $\lambda_\omega \approx 823$  nm and  $\lambda_\omega \approx 813$  nm for the  $s$  and  $p$  polarization, respectively, indicates the spectral position of the MC mode for the chosen polarization. The fundamental radiation with these wavelengths efficiently penetrates into the MC, where it is localized in the vicinity of MC layer because of a multiple-beam interference. The spectral splitting of the mode is likely caused by the anisotropy of dielectric constant of the Bi:YIG layer, because the  $p$ -polarized fundamental radiation, contrary to the  $s$ -polarized radiation, is a superposition of the tangential and normal electromagnetic field components.

Figure 3 presents the intensity of the  $p$ -polarized SH radiation generated by the fundamental radiation polarized at an angle of  $45^\circ$  to the  $s$ - and  $p$ -polarized waves. The spectrum shows two distinct peaks at  $\lambda_\omega \approx 862$  nm and  $\lambda_\omega \approx 810$  nm, which are close to the positions of the MC mode for the fundamental  $s$  and  $p$  components. This resonant SH enhancement is caused by the alternate localization of the fundamental  $s$  and  $p$  components inside the MC layer. Negligible SH intensities at the fundamental wavelengths near the edge of photonic bandgap, where the phase-matching conditions are fulfilled for the SH generation in photonic crystal mirrors, indicate that Bragg reflectors do not make contribution to the observed SH radiation signal. To within the experimental accuracy, the intensity of  $s$ -polarized SH radiation in the absence of an external magnetic field was zero for any polarization of fundamental radiation.

Figure 3 also demonstrates the optical rotation (upon changing the direction of the applied magnetic field)  $\theta_{2\omega}$  of the SH radiation generated by the  $p$ -polarized fundamental radiation. The spectral range of  $\theta_{2\omega}$  is limited by a decrease in the SH intensity, because the

fundamental radiation and the MC mode are then off resonance. At the fundamental wavelength  $\lambda_\omega \approx 795$  nm corresponding to the short-wavelength edge of the MC mode for the  $p$ -polarized wave, the rotation angle of SH wave polarization is about  $2.8^\circ$ . The tuning of the fundamental wavelength to the long-wavelength edge of the mode results in a monotonic increase in  $\theta_{2\omega}$  to  $\sim 7.0^\circ$ . This corresponds to the Kerr rotation of  $\theta_{2\omega}/2 = 18.5^\circ/\mu\text{m}$  for  $\lambda_\omega = 825$  nm.

The magnetization-induced rotation of SH wave polarization is caused by the appearance of magnetic components in the quadratic susceptibility of the ferrite garnet layer, resulting in the generation of  $s$ -polarized SH component and its enhancement due to the localization of fundamental radiation in the MC layer. Another mechanism of the rotation of SH wave polarization amounts to the Kerr rotation of the fundamental wave polarization and its enhancement due to the resonance with the MC mode. The multiple-beam interference of the resonant fundamental radiation inside the ferromagnetic MC layer brings about additive increase in the magnetization-induced rotation of fundamental wave polarization and appearance of the  $s$ -polarized component in the initially  $p$ -polarized fundamental field.

In the description of MSHG from the magnetophotonic MC, it is assumed that the polycrystalline ferrite garnet MC layer with in-plane isotropy is the only source of the dipole SH radiation. The nature of quadratic nonlinearity of ferrite garnet can be associated with the inhomogeneous deformations arising in the direction normal to the layer while annealing. Let us denote by  $z$  the normal coordinate to the plane of MC layer and by  $xz$  the plane of incidence. Then the set of nonzero components of quadratic susceptibility of the garnet layer is written as

$$\chi_{zzz}^{(2)}, \chi_{xzx}^{(2)} = \chi_{yzy}^{(2)}, \quad \chi_{zxx}^{(2)} = \chi_{zyy}^{(2)}. \quad (1)$$

In the absence of magnetic field, the SH radiation generated by the  $p$ -polarized fundamental field with the amplitude  $E_p^\omega = \{E_x^\omega, 0, E_z^\omega\} \equiv E_p^\omega \{F_x^\omega, 0, F_z^\omega\}$  in a film with in-plane isotropy is strictly  $p$ -polarized due to the symmetry properties of the quadratic susceptibility tensor. The SH wave amplitude  $E_p^{2\omega} = \{E_x^{2\omega}, 0, E_z^{2\omega}\} \equiv E_p^{2\omega} \{F_x^{2\omega}, 0, F_z^{2\omega}\}$  is given by

$$E_p^{2\omega} = G(E_p^\omega)^2 (F_z^{2\omega} (F_x^\omega)^2 \chi_{zxx}^{(2)} + F_x^{2\omega} F_x^\omega F_z^\omega \chi_{xzx}^{(2)} + F_z^{2\omega} (F_z^\omega)^2 \chi_{zzz}^{(2)}), \quad (2)$$

where  $G$  is the proportionality coefficient equivalent to the Green's function for a multilayer medium. It accounts for the result of integration over the MC layer and the geometric factors. In the polar geometry, the applied magnetic field induces  $s$ -polarized SH field, which is generated by the magnetic component  $\chi_{yxz}^{(2),M}$

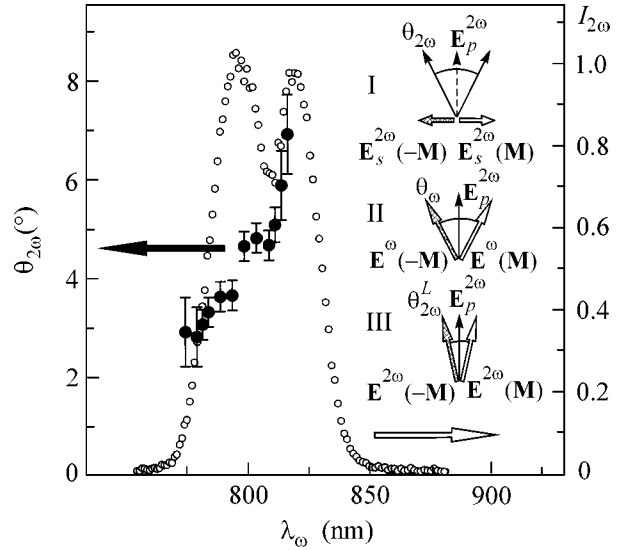


**Fig. 3.** Dark circles are for the angle  $\theta_{2\omega}$  of magnetization-induced, polarization rotation measured for the SH wave generated by the  $p$ -polarized fundamental wave upon changing the direction of the saturating magnetic field. Light circles are for the intensity  $I_{2\omega}$  of the  $p$ -polarized SH wave generated by the fundamental radiation with a mixed polarization (in arbitrary units). Insets: schematically illustrated mechanisms of magnetization-induced rotation of the SH wave. (I) Generation of magnetization-induced  $s$ -polarized SH field  $E_s^{2\omega}$  caused by the magnetic component  $\chi_{yxz}^{(2),M}$  of quadratic susceptibility; (II) Kerr rotation  $E_p^\omega$  of the fundamental wave polarization; and (III) Kerr rotation  $E_p^{2\omega}$  of the SH wave polarization plane.

of quadratic susceptibility. This component is nonzero for the isotropic layer in the geometry of polar Kerr effect [19]. Additionally, the fundamental wave undergoes Kerr rotation inside the MC layer, so that fundamental fields of both ( $s$  and  $p$ ) polarizations coexist inside it. Because of this, the  $s$ -polarized SH field can be generated by the nonmagnetic component  $\chi_{yzy}^{(2)}$  of quadratic susceptibility. Finally, the polarization rotation for the initially  $p$ -polarized SH field can be due to the linear magneto-optical Kerr effect at the SH frequency. Therefore, in the presence of magnetic field, the amplitude of  $s$ -polarized SH wave of purely magnetization-induced nature is given by

$$E_s^{2\omega}(M) = G(E_p^\omega)^2 (F_x^\omega F_z^\omega \chi_{yxz}^{(2),M} + F_z^\omega \chi_{yzy}^{(2)} \sin(\theta_\omega/2)) + E_p^{2\omega} \sin(\theta_{2\omega}^L/2), \quad (3)$$

where  $\theta_\omega$  and  $\theta_{2\omega}^L$  are the angles of rotation (due to a change in the magnetic-field direction) caused by the magneto-optical Kerr effect for the fundamental and SH radiations and  $M$  is the normal component of the mag-

netization vector of the ferrite garnet MC layer. The weak magnetic-field dependence of the  $G$  and  $F$  coefficients is ignored in Eq. (3). The intensity of the total SH field is determined by the superposition of the  $p$ - and  $s$ -polarized SH waves:

$$I_{2\omega}(\theta) = \left| E_p^{2\omega} \exp(i\phi) \cos\theta + E_s^{2\omega}(M) \sin\theta \right|^2, \quad (4)$$

where  $\theta$  is the analyzer-axis rotation angle measured from the  $p$ -polarization direction and  $\phi$  is the phase shift between the SH  $p$  and  $s$  components, which are, generally, complex quantities. The experimental polarization diagrams demonstrate that the SH wave is linearly polarized, so that one can set  $\phi = 0$  with a good accuracy. Then the polarization rotation upon changing the direction of magnetic field can be written for the SH wave as

$$\begin{aligned} \tan\theta_{2\omega} &\equiv 2E_s^{2\omega}/E_p^{2\omega} \\ &= 2 \frac{F_x^\omega \chi_{yxz}^{(2),M} + \chi_{zyz}^{(2)} \sin(\theta_\omega/2)}{F_z^{2\omega} (F_x^\omega)^2 (F_z^\omega)^{-1} \chi_{zxx}^{(2)} + F_x^{2\omega} F_x^\omega \chi_{xzx}^{(2)} + F_z^{2\omega} F_z^\omega \chi_{zzz}^{(2)} + 2 \sin(\theta_{2\omega}^L/2)}, \end{aligned} \quad (5)$$

where the second-order magnetization-induced contribution to  $E_p^{2\omega}$  is ignored. Assume that the components of nonmagnetic quadratic susceptibility are of the same order and that the quantities in the numerator are real. Then, for small Kerr rotation angles  $\theta_{2\omega}$ ,  $\theta_\omega$ , and  $\theta_{2\omega}^L$  and small angles of incidence on the MC layer ( $F_z^{2\omega}$ ,  $F_z^\omega \rightarrow 0$  and  $F_x^{2\omega}$ ,  $F_x^\omega \rightarrow 1$ ), the following estimate is obtained for  $\theta_{2\omega}$ :

$$\theta_{2\omega} \sim \frac{\chi_{yxz}^{(2),M}}{\chi_{xzx}^{(2)}} + \theta_\omega/2 + \theta_{2\omega}^L. \quad (6)$$

The spectral dependence of the first term in Eq. (6) can be ignored, because the fundamental wavelength-tuning range is small enough for the noticeable spectral dependence to appear in the quadratic susceptibility components. The quantity  $\theta_{2\omega}^L$  can also be assumed to be constant, because no resonance features are observed at the SH wavelength in the linear reflection spectrum of the magnetophotonic MC. For this reason, the spectral dependence  $\theta_{2\omega}(\lambda_\omega)$  is completely due to the Kerr rotation of fundamental radiation occurring at resonance with the MC mode. The maximum of magnetization-induced rotation of SH polarization corresponds to the largest spectral overlap between the modes for the  $s$ - and  $p$ -polarized fundamental waves. For this reason,  $\theta_{2\omega}$  increases monotonically upon tuning the fundamental wavelength from the  $p$ -mode maximum to the overlap of the  $p$  and  $s$  MC modes. At the short-wavelength edge of the  $\theta_{2\omega}(\lambda_\omega)$  spectrum, where

the propagation of the  $s$ -polarized fundamental wave is forbidden in the MC, one has  $\theta_\omega = 0$ , and the nonzero  $\theta_{2\omega}$  values are caused by the generation of  $s$ -polarized magnetization-induced SH by the magnetic component  $\chi_{yxz}^{(2),M}$  of the quadratic susceptibility and by the linear Kerr rotation of SH wave polarization. Independent experimental measurements give  $\theta_{2\omega}^L \sim 1^\circ$ . Hence, the experimental  $\theta_{2\omega}$  values at the edges of the spectral range can be used to estimate the ratio  $\chi_{yxz}^{(2),M}/\chi_{xzx}^{(2)} \sim 0.04$  of the magnetic and nonmagnetic components of quadratic susceptibility and the characteristic Kerr rotation angle  $\theta_\omega/2 \approx 22.0^\circ/\mu\text{m}$  ( $\lambda_\omega \approx 825$  nm) for the fundamental wave in the ferrite-garnet MC layer. Taking into account that our model is rather crude, the estimate obtained for  $\chi_{yxz}^{(2),M}/\chi_{xzx}^{(2)}$  can be considered as being in good agreement with the estimate 0.1 made in [12] for ferrite garnet nanoparticles. The  $\theta_\omega$  values are approximately 50 times larger those obtained for ferrite garnet films at the same wavelengths.

In summary, the magnetization-induced second harmonic generation has been investigated in the magnetophotonic bandgap microstructures—microcavities based on bismuth-doped yttrium iron garnet. At resonance with the MC mode, the spatial localization of an electromagnetic field inside the ferromagnetic MC enhances magnetization-induced second harmonic. Spectroscopic study of MSHG near the MC mode in the geometry of polar magneto-optical Kerr effect has demonstrated a giant amplification, up to  $18.5^\circ/\mu\text{m}$ , of the rotation of SH wave polarization for the resonant fundamental radiation at the wavelength  $\lambda_\omega \approx 825$  nm.

This work was supported by the Russian Foundation for Basic Research (project nos. 01-02-16746, 01-02-17524, 01-02-04018, 00-02-16253).

## REFERENCES

1. K. N. Bennemann, *J. Magn. Magn. Mater.* **200**, 679 (1999).
2. O. A. Aktsipetrov, *Colloids Surf., A* **202**, 165 (2002).
3. O. A. Aktsipetrov, O. V. Braginskii, and D. A. Esikov, *Kvantovaya Élektron. (Moscow)* **17**, 320 (1990).
4. N. N. Akhmediev, S. B. Borisov, A. K. Zvezdin, *et al.*, *Fiz. Tverd. Tela (Leningrad)* **27**, 1075 (1985) [*Sov. Phys. Solid State* **27**, 650 (1985)].
5. J. Reif, J. C. Zink, C.-M. Schneider, and J. Kirshner, *Phys. Rev. Lett.* **67**, 2878 (1991).
6. J. Hohlfield, E. Matthias, R. Knorren, and K. H. Bennemann, *Phys. Rev. Lett.* **78**, 4861 (1997).
7. Q. Y. Jin, H. Regensburger, R. Vollmer, and J. Kirschner, *Phys. Rev. Lett.* **80**, 4056 (1998).
8. U. Conrad, J. Güdde, V. Jänhke, and E. Matthias, *Phys. Rev. B* **63**, 144417 (2001).
9. O. A. Aktsipetrov, V. A. Aleshkevich, A. V. Melnikov, *et al.*, *J. Magn. Magn. Mater.* **165**, 421 (1997).

10. V. V. Pavlov, R. V. Pisarev, A. Kirilyuk, and Th. Rasing, *Phys. Rev. Lett.* **78**, 2004 (1997).
11. T. V. Murzina, E. A. Ganshina, S. V. Guschin, *et al.*, *Appl. Phys. Lett.* **73**, 3769 (1998).
12. T. V. Murzina, A. A. Nikulin, O. A. Aktsipetrov, *et al.*, *Appl. Phys. Lett.* **79**, 1309 (2001).
13. J. D. Joannopoulos, R. D. Meade, and J. N. Winn, *Photonic Crystals: Molding the Flow of Light* (Princeton Univ. Press, Princeton, 1995).
14. K. Sakoda, *Optical Properties of Photonic Crystals* (Springer-Verlag, Berlin, 2001).
15. T. V. Dolgova, A. I. Maïdykovskii, M. G. Martem'yanov, *et al.*, *Pis'ma Zh. Éksp. Teor. Fiz.* **73**, 8 (2001) [*JETP Lett.* **73**, 6 (2001)].
16. T. V. Dolgova, A. I. Maïdykovskii, M. G. Martem'yanov, *et al.*, *Pis'ma Zh. Éksp. Teor. Fiz.* **75**, 17 (2002) [*JETP Lett.* **75**, 15 (2002)].
17. M. Inoue, K. Arai, T. Fujii, and M. Abe, *J. Appl. Phys.* **83**, 6768 (1998).
18. M. Inoue, K. Arai, T. Fujii, and M. Abe, *J. Appl. Phys.* **85**, 5768 (1999).
19. R.-P. Pan, H. D. Wei, and Y. R. Shen, *Phys. Rev. B* **39**, 1229 (1989).

*Translated by V. Sakun*

# Transition from Non-Fermi Liquid Behavior to Landau–Fermi Liquid Behavior Induced by Magnetic Fields<sup>¶</sup>

Yu. G. Pogorelov<sup>1</sup> and V. R. Shaginyan<sup>2</sup>

<sup>1</sup> Departamento de Física, Universidade do Porto, 4150 Porto, Portugal

<sup>2</sup> Petersburg Nuclear Physics Institute, Russian Academy of Sciences, Gatchina, 188300 Russia

e-mail: vrshag@thd.pnpi.spb.ru

Received September 23, 2002

We show that a strongly correlated Fermi system with a fermion condensate which exhibits strong deviations from Landau–Fermi liquid behavior is driven into the Landau–Fermi liquid by applying a small magnetic field  $B$  at temperature  $T = 0$ . This field-induced Landau–Fermi liquid behavior provides constancy of the Kadowaki–Woods ratio. A re-entrance into the strongly correlated regime is observed if the magnetic field  $B$  decreases to zero; the effective mass  $M^*$  then diverges as  $M^* \propto 1/\sqrt{B}$ . At finite temperatures, the strongly correlated regime is restored at some temperature  $T^* \propto \sqrt{B}$ . This behavior is of a general form and takes place in both three-dimensional and two-dimensional strongly correlated systems. We demonstrate that the observed  $1/\sqrt{B}$  divergence of the effective mass and other specific features of heavy-fermion metals are accounted for by our consideration. © 2002 MAIK “Nauka/Interperiodica”.

PACS numbers: 71.10.Hf; 71.27.+a

Recently, a peculiar critical point was observed in heavy-fermion metal  $\text{YbRh}_2\text{Si}_2$  at low temperatures  $T$  [1]. This critical point is driven by the magnetic field  $B$ , which suppresses the antiferromagnetic order when it reaches the critical value  $B = B_{c0}$ , while the effective mass  $M^*$  diverges as  $M^* \propto 1/\sqrt{B - B_{c0}}$  [1]. The study of the magnetic field dependence of the coefficients  $A$ ,  $\gamma_0$ , and  $\chi_0$  in the resistivity  $\rho(T) = \rho_0 + \Delta\rho$ , with  $\Delta\rho = A(B)T^2$ , specific heat  $C/T = \gamma_0(B)$ , and magnetic  $ac$  susceptibility, has revealed that  $\text{YbRh}_2\text{Si}_2$  behaves as a true Landau–Fermi liquid (LFL) for  $B > B_{c0}$ , and the well-known Kadowaki–Woods ratio  $A/\gamma_0$  [2] is preserved [1]. In contrast, for  $B = 0$ ,  $\text{YbRh}_2\text{Si}_2$  demonstrates a non-Fermi liquid (NFL) behavior, and the resistivity follows a quasilinear temperature dependence  $\Delta\rho \sim T$  down to 80 mK, at which antiferromagnetic (AF) order takes place. At lower temperatures, the resistivity in the AF-ordered state is described by  $\Delta\rho \sim T^2$ . A similar picture is observed in heavy-fermion compounds  $\text{CeMIn}_5$  ( $M = \text{Ir, Co, and Rh}$ ), where the electronic specific heat  $C$  shows more pronounced metallic behavior at sufficiently high magnetic fields [3]. These observations are consistent with the de Haas van Alphen (dHvA) studies of  $\text{CeIrIn}_5$ , which find that the effective mass decreases with increasing  $B$  [3, 4].

It is pertinent to note that heavy fermion metals are more likely three dimensional (3D) than two dimensional (2D). The origin of the NFL behavior observed

in heavy fermion metals is still a subject of controversy [5]. Moreover, the observed constancy of the Kadowaki–Woods ratio when  $B \rightarrow B_{c0}$  [1] leads to the failure of the standard model of heavy-fermion metals, when the mass renormalization is supposed to come from the exchange by soft magnetic fluctuations in a 2D spin fluid [6]. As a result, we are left with even more complicated and challenging problems in the physics of strongly correlated electrons.

In this letter, we study the nature of the critical behavior, assuming that the fermion condensation phase transition (FCQPT) [7] plays the role of the critical point. Analyzing the appearance of the fermion condensate (FC) which occurs beyond the point of FCQPT in an electron Fermi liquid and induces the NFL behavior, we show that the liquid is driven, by applying a weak magnetic field, back into a specific LFL state with effective mass  $M^* \propto 1/\sqrt{B}$ . The LFL behavior induced by rather low magnetic fields provides constancy of the Kadowaki–Woods ratio. But the strongly correlated regime is restored when the magnetic field  $B$  decreases to zero, while the effective mass  $M^*$  diverges as  $M^* \propto 1/\sqrt{B}$ . Also, the strongly correlated regime is restored at some finite temperature  $T^*(B) \propto \sqrt{B}$ . Such a behavior is of a general form and takes place in both three-dimensional and two-dimensional strongly correlated systems. We demonstrate that the observed crossover from NFL to LFL in certain heavy-fermion metals is accounted for by our consideration.

<sup>¶</sup>This article was submitted by the authors in English.

For the reader's convenience, we first outline the NFL behavior of Fermi systems with FC and the main properties of FCQPT using, as an example, a two-dimensional electron liquid in the superconducting state induced by FCQPT [7, 8]. At  $T = 0$ , the ground-state energy  $E_{gs}[\kappa(\mathbf{p}), n(\mathbf{p})]$  is a functional of the superconducting order parameter  $\kappa(\mathbf{p})$  and of the quasiparticle occupation function  $n(\mathbf{p})$  and is determined by the known equation of the weak-coupling theory of superconductivity (see, e.g., [9])

$$E_{gs} = E[n(\mathbf{p})] + \int \lambda_0 V(\mathbf{p}_1, \mathbf{p}_2) \kappa(\mathbf{p}_1) \kappa^*(\mathbf{p}_2) \frac{d\mathbf{p}_1 d\mathbf{p}_2}{(2\pi)^4}. \quad (1)$$

Here,  $E[n(\mathbf{p})]$  is the ground-state energy of normal Fermi liquid,  $n(\mathbf{p}) = v^2(\mathbf{p})$ , and  $\kappa(\mathbf{p}) = v(\mathbf{p}) \sqrt{1 - v^2(\mathbf{p})}$ . It is assumed that the pairing interaction  $\lambda_0 V(\mathbf{p}_1, \mathbf{p}_2)$  is weak. Minimizing  $E_{gs}$  with respect to  $\kappa(\mathbf{p})$ , we obtain the equation connecting the single-particle energy  $\varepsilon(\mathbf{p})$  to the superconducting gap  $\Delta(\mathbf{p})$ :

$$\varepsilon(\mathbf{p}) - \mu = \Delta(\mathbf{p}) \frac{1 - 2v^2(\mathbf{p})}{2\kappa(\mathbf{p})}, \quad (2)$$

including the chemical potential  $\mu$ . Here, the single-particle energy  $\varepsilon(\mathbf{p})$  is determined by the Landau equation [10]

$$\varepsilon(\mathbf{p}) = \frac{\delta E[n(\mathbf{p})]}{\delta n(\mathbf{p})}, \quad (3)$$

while the equation for the superconducting gap  $\Delta(\mathbf{p})$  takes the form

$$\Delta(\mathbf{p}) = -\lambda_0 \int V(\mathbf{p}, \mathbf{p}_1) \kappa(\mathbf{p}_1) \frac{d\mathbf{p}_1}{4\pi^2}. \quad (4)$$

If  $\lambda_0 \rightarrow 0$ , then the maximum value of the superconducting gap  $\Delta_1 \rightarrow 0$ , and Eq. (2) reduces to that proposed in [11]:

$$\varepsilon(\mathbf{p}) - \mu = 0, \text{ if } \kappa(p) \neq 0 \text{ (} 0 < n(p) < 1 \text{)} \quad (5)$$

for  $p \in L_{FC}$ :  $p_i \leq p \leq p_f$ .

At  $T = 0$ , Eq. (5) defines a new state of Fermi liquid with FC such that the modulus of the order parameter  $|\kappa(\mathbf{p})|$  has finite values in the FC range of momenta  $L_{FC}$ :  $p_i \leq p \leq p_f$ , while the superconducting gap can be infinitely small,  $\Delta_1 \rightarrow 0$ , in this range [7, 11, 12]. Such a state can be considered as superconducting, with an infinitely small value of  $\Delta_1$ , so that the entropy of this state is zero. This state, created by the quantum phase transition, disappears at  $T > 0$ . The FCQPT can be considered as a "pure" quantum phase transition, because it cannot take place at finite temperatures. Generally, this quantum critical point should not represent the termination at  $T > 0$  of a line of continuous transitions. However, it corresponds to a certain critical value of

density  $x = x_{FC}$  (the critical point of FCQPT) which is determined also by Eq. (5). Notice that, at finite temperatures, the FCQPT continues to have a strong impact on the system properties up to a certain temperature  $T_f$  above which FC effects become insignificant [7, 13]. FCQPT does not violate rotational or translational symmetry of the order parameter  $\kappa(\mathbf{p})$ . It follows from Eq. (5) that the quasiparticle system "splits" into two quasiparticle subsystems: one in the  $L_{FC}$  range, occupied by the quasiparticles with enhanced effective mass  $M_{FC}^* \propto 1/\Delta_1$ , and another with LFL effective mass  $M_L^*$  at  $p < p_i$ . If  $\lambda_0 \neq 0$ , then  $\Delta_1$  becomes finite, and the finite value of the effective mass  $M_{FC}^*$  in  $L_{FC}$  can be obtained from Eq. (2) as [7, 8]

$$M_{FC}^* \approx p_F \frac{p_f - p_i}{2\Delta_1}, \quad (6)$$

while the effective mass  $M_L^*$  is only weakly disturbed. Here,  $p_F$  is the Fermi momentum. It follows from Eq. (6) that the quasiparticle dispersion can be presented by two straight lines characterized by the effective masses  $M_{FC}^*$  and  $M_L^*$ , respectively. These lines intersect near the electron binding energy  $E_0$ , which defines an intrinsic energy scale of the system

$$E_0 = \varepsilon(\mathbf{p}_f) - \varepsilon(\mathbf{p}_i) \approx \frac{(p_f - p_i)p_F}{M_{FC}^*} \approx 2\Delta_1. \quad (7)$$

Let us assume that FC has just taken place, that is,  $p_i \rightarrow p_F \leftarrow p_f$ , the deviation  $\delta n(p)$  from LFL occupation function is small (though finite), and  $\lambda_0 \rightarrow 0$ . Expanding the functional  $E[n(p)]$  in Eq. (3) in a Taylor series with respect to  $\delta n(p)$  and retaining the leading terms, we have

$$\Delta E = \sum_{\sigma_1} \int \varepsilon_0(\mathbf{p}_1, \sigma_1) \delta n(\mathbf{p}_1, \sigma_1) \frac{d\mathbf{p}_1}{(2\pi)^2} + \sum_{\sigma_1 \sigma_2} \int F_L(\mathbf{p}_1, \mathbf{p}_2, \sigma_1, \sigma_2) \delta n(\mathbf{p}_1, \sigma_1) \delta n(\mathbf{p}_2, \sigma_2) \frac{d\mathbf{p}_1 d\mathbf{p}_2}{(2\pi)^4}, \quad (8)$$

where  $F_L(\mathbf{p}_1, \mathbf{p}_2, \sigma_1, \sigma_2) = \delta^2 E / \delta n(\mathbf{p}_1, \sigma_1) \delta n(\mathbf{p}_2, \sigma_2)$  is the Landau interaction and  $\sigma$  denotes the spin states. Varying both sides of Eq. (8) with respect to the functions  $\delta n(p)$  and taking into account Eq. (5), one obtains the FC equation

$$\mu = \varepsilon(\mathbf{p}, \sigma) = \varepsilon_0(\mathbf{p}, \sigma) + \sum_{\sigma_1} \int F_L(\mathbf{p}, \mathbf{p}_1, \sigma, \sigma_1) \delta n(\mathbf{p}_1, \sigma_1) \frac{d\mathbf{p}_1}{(2\pi)^2}; \quad (9)$$

$p_i \leq p \leq p_f \in L_{FC}$ .

Equation (9) acquires nontrivial solutions at the density  $x = x_{\text{FC}}$  if the Landau amplitude  $F_L$  (depending on density) is positive and sufficiently large, so that the potential energy integral on the right-hand side of Eq. (9) prevails over the kinetic energy  $\varepsilon_0(\mathbf{p})$  [11]. Note that in case of heavy fermion metals, this condition can be easily satisfied because of the huge effective mass. It is also seen from Eq. (9) that the FC quasiparticles form a collective state, since their energies are defined by the macroscopic number of quasiparticles within  $L_{\text{FC}}$  and vice versa. The shape of their spectrum is not affected by the Landau interaction, which, generally speaking, depends on the system properties, including the collective states, impurities, etc. The only thing defined by the interaction is the width  $p_i - p_f$  of  $L_{\text{FC}}$  (provided it exists). Thus, we can conclude that the spectra related to FC are of universal form.

At temperatures  $T \geq T_c$ , when  $\Delta_1$  disappears, Eq. (6) for the effective mass  $M_{\text{FC}}^*$  is replaced by [7, 8]

$$M_{\text{FC}}^* \approx p_{\text{F}} \frac{p_f - p_i}{4T}. \quad (10)$$

The energy scale separating the slowly dispersing low-energy part, defined by the effective mass  $M_{\text{FC}}^*$ , from the faster dispersing relatively high-energy part, defined by the effective mass  $M_L^*$ , can be estimated as

$E_0 \approx p_{\text{F}}(p_f - p_i)/M_{\text{FC}}^*$  [7, 8], so for the case of Eq. (10) it is

$$E_0 \approx 4T. \quad (11)$$

It follows from Eq. (10) that  $M_{\text{FC}}^*$  depends on the temperature, and the width  $\gamma$  of the single-particle excitations results in  $\gamma \sim T$ , leading to a linear temperature dependence  $\Delta\rho \sim T$  [13]. This contrasts with the well-known LFL relations  $\gamma \sim T^2$  and  $\Delta\rho \sim T^2$ .

Now we consider the behavior of an electronic system with FC in magnetic fields, supposing the coupling constant  $\lambda_0 \neq 0$  to be infinitely small. As we have seen above, at  $T = 0$ , the superconducting order parameter  $\kappa(\mathbf{p})$  is finite in the FC range, while the maximum value of the superconducting gap  $\Delta_1 \propto \lambda_0$  is infinitely small. Therefore, any small magnetic field  $B \neq 0$  will destroy the coherence of  $\kappa(\mathbf{p})$  and thus FC itself. Also, the existence of FC cannot be compatible with the evident Zeeman splitting of quasiparticle energy bands  $\varepsilon(\mathbf{p}, \sigma) = \varepsilon(\mathbf{p}) - \sigma\mu_{\text{eff}}B$  (see below for  $\mu_{\text{eff}}$ ). To define the type of FC restructuring, simple energy considerations are invoked. On the one hand, the energy gain  $\Delta E_B$  due to the magnetic field  $B$  is  $\Delta E_B \propto B^2$  and tends to zero with  $B \rightarrow 0$ . On the other hand, occupying the finite range  $L_{\text{FS}}$  in the momentum space, FC delivers a finite gain in the ground state energy [11]. Thus, a new state replacing FC should be very close in its ground-state energy to the former state. Such a state is given by the multi-

connected Fermi sphere, where the smooth quasiparticle distribution function  $n(\mathbf{p})$  in the  $L_{\text{FC}}$  range is replaced by a multiconnected distribution  $v(\mathbf{p})$  [14]

$$v(\mathbf{p}) = \sum_{k=1}^n \theta(p - p_{2k-1})(p_{2k} - p), \quad (12)$$

where the parameters  $p_i \leq p_1 < p_2 < \dots < p_{2n} \leq p_f$  are adjusted to obey the normalization conditions

$$\int_{p_{2k}}^{p_{2k+3}} v(\mathbf{p}) \frac{d\mathbf{p}}{(2\pi)^3} = \int_{p_{2k}}^{p_{2k+3}} n(\mathbf{p}) \frac{d\mathbf{p}}{(2\pi)^3}. \quad (13)$$

For the sake of definiteness, we consider the most interesting case of a 3D system, while the consideration of a 2D system goes along the same line. We note that the idea of a multiconnected Fermi sphere, with production of new, interior segments of the Fermi surface, has been considered already [15, 16]. Let us assume that the thickness of each interior block is approximately the same,  $p_{2k+1} - p_{2k} \approx \delta p$ , and  $p$  is defined by  $B$ . Then, the single-particle energy in the region  $L_{\text{FC}}$  can be fitted by

$$\varepsilon(\mathbf{p}) - \mu \sim \mu \frac{\delta p}{p_{\text{F}}} \left[ \sin\left(\frac{p}{\delta p}\right) + b(p) \right]. \quad (14)$$

The blocks are formed, since all the single-particle states around the minimum values of the fast sine function are occupied, and those around its maximum values are empty, the average occupation being controlled by a slow function  $b(\mathbf{p}) \approx \cos[\pi n(\mathbf{p})]$ . It is seen from Eq. (14) that the effective mass  $m^*$  at each internal Fermi surface is on the order of the bare mass  $m_0$ ,  $m^* \sim m_0$ . Upon replacing  $n(\mathbf{p})$  in Eq. (8) by  $v(\mathbf{p})$ , defined by Eqs. (12) and (13), and taking into account Simpson's rule, we find that the minimum loss in the ground-state energy due to the formation of blocks is about  $(\delta p)^4$ . This result can be understood if one bears in mind that the continuous FC function  $n(\mathbf{p})$  delivers the minimum value to the energy functional, Eq. (8), while the approximation  $v(\mathbf{p})$  by steps of size  $\delta p$  produces the minimum error on the order of  $(\delta p)^4$ . On the other hand, this loss must be compensated by the energy gain due to the magnetic field. Thus, we arrive at

$$\delta p \propto \sqrt{B}. \quad (15)$$

With account taken of the Zeeman splitting in the dispersion law, Eq. (14), each of the blocks is polarized, since its outer areas are occupied only by spin-up quasiparticles. The width of these areas in the momentum space  $\delta p_0$  is given by

$$\frac{p_{\text{F}} \delta p_0}{m^*} \sim B \mu_{\text{eff}}, \quad (16)$$

where  $\mu_{\text{eff}} \sim \mu_B$  is the effective moment. We can consider such a polarization without perturbing the previous estimates, since it is seen from Eq. (15) that

$dp_0/dp \ll 1$ . The total polarization  $\Delta P$  is obtained by multiplying  $\delta p_0$  by the number  $N$  of the blocks, which is proportional to  $1/\delta p$ ,  $N \sim (p_f - p_i)/\delta p$ . Taking into account Eq. (15), we obtain

$$\Delta P \sim m^* \frac{p_f - p_i}{\delta p} B \mu_{\text{eff}} \propto \sqrt{B}, \quad (17)$$

and thus it prevails over  $\sim B$  contribution from the LFL part. On the other hand, this quantity can be expressed as

$$\Delta P \propto M^* B, \quad (18)$$

where  $M^*$  is the ‘‘average’’ effective mass related to the finite density of states at the Fermi level,

$$M^* \sim N m^* \propto \frac{1}{\delta p}. \quad (19)$$

We can also conclude that  $M^*$  defines the specific heat. Otherwise, Eq. (15) can be examined starting from a different point surmising that a multiconnected Fermi sphere can be approximated by a single block. Let us put  $\lambda_0 = 0$ . Then, the energy gain due to the magnetic field  $\Delta E_B \sim B^2 M^*$ . The energy loss  $\Delta E_{\text{FC}}$  because of the restructuring of the FC state can be estimated by using the Landau formula, which directly follows from Eqs. (8) and (9)

$$\Delta E_{\text{FC}} = \int (\epsilon(\mathbf{p}) - \mu) \delta n(\mathbf{p}) \frac{d\mathbf{p}^3}{(2\pi)^3}. \quad (20)$$

As we have seen above, the region occupied by variation  $\delta n(\mathbf{p})$  has the length  $\delta p$ , while  $(\epsilon(\mathbf{p}) - \mu) \sim (p - p_F) p_F / M^*$ . As a result, we have  $\Delta E_{\text{FC}} = \delta p^2 / M^*$ . Upon equating  $\Delta E_B$  and  $\Delta E_{\text{FC}}$  and taking into account Eq. (19), we arrive at the following equation:

$$\frac{\delta p^2}{M^*} \propto \delta p^3 \propto \frac{B^2}{\delta p}, \quad (21)$$

which coincides with Eq. (15).

It follows from Eqs. (17) and (18) that the effective mass  $M^*$  diverges as

$$M^* \propto \frac{1}{\sqrt{B}}. \quad (22)$$

Equation (22) shows that, by applying a magnetic field  $B$ , the system can be driven back into LFL, with the effective mass  $M^*(B)$  dependent on the magnetic field. It was demonstrated that the constancy of the Kadowaki–Woods ratio is obeyed by systems in the strongly correlated regime when the effective mass is sufficiently large [17]. Therefore, we are led to the conclusion that, by applying magnetic fields, the system is driven back into LFL, where the constancy of the Kadowaki–Woods ratio is obeyed. Since the resistivity  $\Delta \rho \propto (M^*)^2$  [17], we obtain from Eq. (22)

$$\Delta \rho \propto \frac{1}{B}. \quad (23)$$

At finite temperatures, the system persists to be LFL, but there is a temperature  $T^*(B)$  at which the polarized state is destroyed. To calculate the function  $T^*(B)$ , we observe that the effective mass  $M^*$  characterizing the single-particle spectrum cannot be changed at  $T^*(B)$ . In other words, at the crossover point, we have to compare the effective mass defined by  $T^*$ , Eq. (10), and that defined by the magnetic field  $B$

$$\frac{1}{M^*} \propto T^* \propto \sqrt{B}. \quad (24)$$

As a result, we obtain

$$T^*(B) \propto \sqrt{B}. \quad (25)$$

At temperatures  $T \geq T^*$ , the system comes back into the state with  $M^*$  defined by Eq. (10), and we observe the NFL behavior. It follows from Eq. (25) that a heavy fermion system at some temperature  $T$  can be driven back into LFL by applying strong enough magnetic field  $B \geq B_{\text{cr}} \propto (T^*)^2$ . We can also conclude that, at finite temperature  $T$ , the effective mass of a heavy-fermion system is relatively field-independent at magnetic fields  $B \leq B_{\text{cr}}$  and shows a more pronounced metallic behavior at  $B \geq B_{\text{cr}}$  since the effective mass is decreased; see Eq. (22). The same behavior of the effective mass can be observed in the dHvA measurements. We note that our consideration is valid up to temperatures  $T \ll T_f$ .

Now we are in position to consider the nature of the field-induced quantum critical point in  $\text{YbRh}_2\text{Si}_2$ . The properties of this AF heavy-fermion metal with the ordering Neél temperature,  $T_N = 70$  mK were recently investigated in [1, 18]. In the AF state, this metal shows LFL behavior. As soon as the weak AF order is suppressed either by a tiny volume expansion or by temperature, pronounced deviations from LFL behavior are observed. The experimental facts show that the spin density wave picture fails when dealing with the obtained data [1, 6, 18]. We assume that the electron density in  $\text{YbRh}_2\text{Si}_2$  is close to the critical value  $(x_{\text{FC}} - x)/x_{\text{FC}} \ll 1$  [19], so that this system can be easily driven across FCQPT. Then, in the AF state, the effective mass is given by Eq. (22), and the electron system of  $\text{YbRh}_2\text{Si}_2$  possesses LFL behavior. When the AF state is suppressed at  $T > T_N$ , the system comes back into NFL. By tuning  $T_N \rightarrow 0$  at a critical field  $B = B_{c0}$ , the itinerant AF order is suppressed and replaced by spin fluctuations [18]. Thus, we can expect absence of any long-ranged magnetic order in this state, and the situation corresponds to a paramagnetic system with strong correlation in the field  $B = 0$ . As a result, the FC state is restored, and we can observe NFL behavior at any temperatures in accordance with experimental facts [1]. As soon as an excess magnetic field  $B > B_{c0}$  is applied, the system is driven back into LFL. To describe the behav-

ior of the effective mass, we can use Eq. (22), replacing  $B$  with  $B - B_{c0}$

$$M^* \propto \frac{1}{\sqrt{B - B_{c0}}}. \quad (26)$$

Equation (26) demonstrates the  $1/\sqrt{B - B_{c0}}$  divergence of the effective mass, and therefore the coefficients  $\gamma_0(B)$  and  $\chi_0(B)$  should have the same behavior. Meanwhile, the coefficient  $A(B)$  diverges as  $1/(B - B_{c0})$ , being proportional to  $(M^*)^2$  [17] and thus preserving the Kadowaki–Woods ratio, in agreement with experimental findings [1]. To construct the  $T - B$  phase diagram for  $\text{YbRh}_2\text{Si}_2$ , we use the same replacement  $B \rightarrow B - B_{c0}$  in Eq. (25)

$$T^*(B) \propto \sqrt{B - B_{c0}}. \quad (27)$$

The phase diagram given by Eq. (27) is in good qualitative agreement with the experimental data [1]. We recall that our consideration is valid at temperatures  $T \ll T_f$ . The experimental phase diagram shows that the behavior  $T^* \propto \sqrt{B - B_{c0}}$  is observed up to 150 mK [1] and allows us to estimate the magnitude of  $T_f$ , which can reach at least 1 K in this system.

To conclude, we have demonstrated that a new type of the quantum critical point observed in heavy-fermion metal  $\text{YbRh}_2\text{Si}_2$  can be identified as FCQPT.

This work was supported in part by the Russian Foundation for Basic Research, project no. 01-02-17189.

## REFERENCES

1. P. Gegenwart, J. Custers, C. Geibel, *et al.*, Phys. Rev. Lett. **89**, 056402 (2002); P. Gegenwart, J. Custers, T. Tayama, *et al.*, cond-mat/0207570.
2. K. Kadowaki and S. B. Woods, Solid State Commun. **58**, 507 (1986).
3. J. S. Kim, J. Alwood, G. R. Stewart, *et al.*, Phys. Rev. B **64**, 134524 (2001).
4. Y. Haga, Y. Inada, H. Harima, *et al.*, Phys. Rev. B **63**, 060503 (2001).
5. P. Coleman, C. Pepin, Qimiao Si, and R. Ramazashvili, J. Phys.: Condens. Matter **13**, R723 (2001).
6. P. Coleman, cond-mat/0206003.
7. M. Ya. Amusia and V. R. Shaginyan, Pis'ma Zh. Éksp. Teor. Fiz. **73**, 268 (2001) [JETP Lett. **73**, 232 (2001)]; S. A. Artamonov and V. R. Shaginyan, Zh. Éksp. Teor. Fiz. **119**, 331 (2001) [JETP **92**, 287 (2001)]; M. Ya. Amusia and V. R. Shaginyan, Phys. Rev. B **63**, 224507 (2001).
8. M. Ya. Amusia, S. A. Artamonov, and V. R. Shaginyan, Pis'ma Zh. Éksp. Teor. Fiz. **74**, 435 (2001) [JETP Lett. **74**, 396 (2001)].
9. D. R. Tilley and J. Tilley, *Superfluidity and Superconductivity* (Hilger, Bristol, 1975).
10. L. D. Landau, Zh. Éksp. Teor. Fiz. **30**, 1058 (1956) [Sov. Phys. JETP **3**, 920 (1956)].
11. V. A. Khodel and V. R. Shaginyan, Pis'ma Zh. Éksp. Teor. Fiz. **51**, 488 (1990) [JETP Lett. **51**, 553 (1990)]; V. A. Khodel, V. R. Shaginyan, and V. V. Khodel, Phys. Rep. **249**, 1 (1994).
12. G. E. Volovik, Pis'ma Zh. Éksp. Teor. Fiz. **53**, 208 (1991) [JETP Lett. **53**, 222 (1991)].
13. J. A. Dukelsky, V. A. Khodel, P. Schuck, and V. R. Shaginyan, Z. Phys. B **102**, 245 (1997).
14. S. A. Artamonov, V. R. Shaginyan, and Yu. G. Pogorelov, Pis'ma Zh. Éksp. Teor. Fiz. **68**, 893 (1998) [JETP Lett. **68**, 942 (1998)].
15. M. de Llano and J. P. Vary, Phys. Rev. C **19**, 1083 (1979); M. de Llano, A. Plastino, and J. G. Zabolitsky, Phys. Rev. C **20**, 2418 (1979).
16. M. V. Zverev and M. Baldo, cond-mat/9807324.
17. V. A. Khodel and P. Schuck, Z. Phys. B **104**, 505 (1997).
18. K. Ishida, K. Okamoto, Y. Kawasaki, *et al.*, Phys. Rev. Lett. **89**, 107202 (2002).
19. V. R. Shaginyan, cond-mat/0208568.

# Quantum Transport in Lattices of Coupled Electronic Billiards

Z. D. Kvon

*Institute of Semiconductor Physics, Siberian Division, Russian Academy of Sciences, Novosibirsk, 630090 Russia*

Received September 16, 2002

A new system with dynamic chaos—2D lattice of single Sinai billiards coupled through quantum dots—is studied experimentally. Localization in such a system was found to be substantially suppressed, because the characteristic size of the billiard for  $g \leq 1$  ( $g$  is conductance measured in  $e_2/h$  units) is the localization length rather than the de Broglie wavelength of an electron, as in the usual 2D electron system. Lattice ballistic effects (commensurate peaks in the magnetoresistance) for  $g \ll 1$ , as well as extremely large magnetoresistance caused by the interference in chaotic electron trajectories, were found. Thus, this system is shown to be characterized by simultaneous existence of effects that are inherent in order (commensurate peaks of magnetoresistance), disorder (percolation charge transport), and chaos (weak localization in chaotic electron trajectories). © 2002 MAIK “Nauka/Interperiodica”.

PACS numbers: 73.21.La; 73.23.Ad; 05.45.Mt

Investigations of classical and quantum transport in systems with dynamic chaos began ten years ago and are of great and topical interest in condensed-state physics. This interest is stimulated primarily by advances in semiconductor technology that provided various experimental realizations of these systems and, therefore, brought dynamic chaos physics beyond the scope of pure theory. Experiments made it possible to test and refine numerous theoretical predictions and pose new problems for theory.

Various kinds of these systems have been studied to date. In particular, electron billiards based on a 2D electron gas with high mobility in AlGaAs/GaAs heterojunction are examined most extensively. They can be divided into two groups. The first group involves single regular or chaotic Bunimovich and Sinai billiards, which are, in fact, quantum dots with a large number of electrons [1–5]. The second group involves macroscopic 2D (lattices of antidots) [6–10] and 1D Sinai billiards [11]. These billiards exhibited a number of interesting phenomena associated with both classical and quantum chaotic dynamics of electrons such as the formation of dynamically stable outgoing electron trajectories [10], mesoscopic conductance fluctuations [1, 12], and chaotic weak localization [2], which are due to the interference between chaotic electron trajectories.

This study is devoted to a new kind of electron billiards—the lattice of electron billiards coupled through quantum dots, which is described in [13]. On the one hand, this lattice exhibits the properties of a single Sinai billiard. On the other hand, it is a macroscopic system, where these billiards form a regular lattice. This system is unique, because it simultaneously exhibits phenomena associated with order (commensurate peaks of

magnetoresistance), disorder (percolation charge transport), and chaos (weak localization in chaotic electron trajectories).

**1. How can a lattice of coupled electron billiards be realized?** In the experiments, the original system was a 2D gas in an AlGaAs heterojunction with a lattice of antidots. The 2D-gas parameters are as follows: the 2D electron density  $N_s = (2-3) \times 10^{11} \text{ cm}^{-2}$ , mobility  $\mu = (3-8) \times 10^5 \text{ cm}^2/\text{V s}$ , and mean free path  $l_p = (2-8) \mu\text{m}$ . Two types of lattices were manufactured: a square with period  $d = 0.6$  and  $0.7 \mu\text{m}$  and hexagonal with  $d = 0.6 \mu\text{m}$ . The lithographic size of antidots was equal to  $0.2 \mu\text{m}$  in all cases. An important feature of the samples under consideration is the presence of a metallic Ni/Au or TiAu gate deposited on the upper part of the structure. This gate was used to control the width of the depletion layer around antidots and thereby their actual size and distance between their boundaries. This adjustment was used to change the regime of a 2D electron gas with usual lattice of antidotes (scatterers) to the regime of a lattice of coupled electron billiards, where antidots are reflecting walls of Sinai billiards. In the first regime,  $(\mathbf{d} - \mathbf{a}) > \mathbf{a}$ , where  $\mathbf{a}$  is the size of an antidot and  $\mathbf{d}$  is the distance between the centers of neighboring antidots. In the second regime,  $\mathbf{d} \approx \mathbf{a}$ , and  $(\mathbf{d} - \mathbf{a}) \ll \mathbf{a}$ ; i.e., this is a lattice of close-packed antidots. Figure 1 illustrates these cases. If  $(\mathbf{d} - \mathbf{a}) \sim \lambda$  ( $\lambda$  is the de Broglie wavelength of an electron), we have a lattice of Sinai billiards coupled through quantum dots. This case will be considered below.

**2. Commensurate magnetoresistance peaks.** Figure 2 shows typical magnetotransport measurement results for square lattices in the magnetic-field range from  $-0.1$  to  $2 \text{ T}$  and temperature range  $60 \text{ mK}-1.2 \text{ K}$

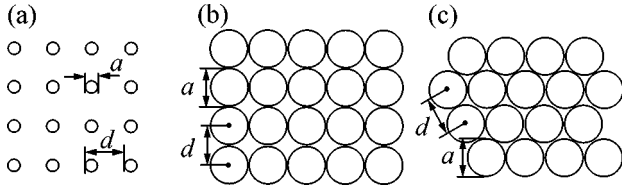


**Fig. 1.** Lattices of antidots for (a)  $(d - a) > a$  (square), (b)  $d \approx a$  (square), and (c)  $d \approx a$  (hexagonal).

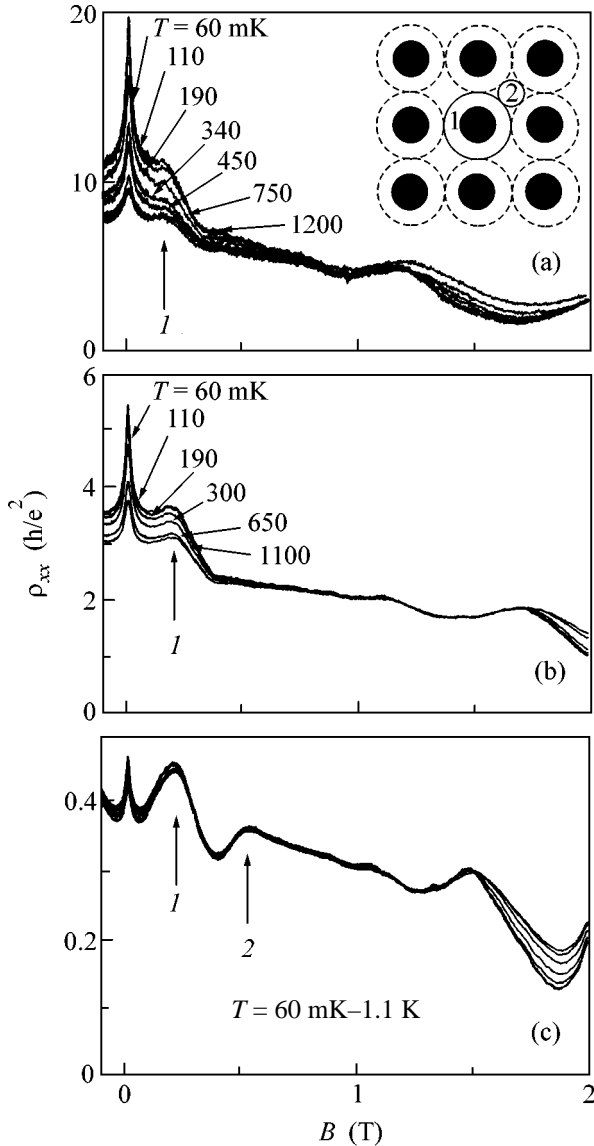


**Fig. 2.** Magnetic-field dependences of  $\rho_{xx}$  in temperature range  $T = 60 \text{ mK} - 1.2 \text{ K}$  (AG219 sample) for (a)  $\rho_{xx}(0) \gg 1$ , (b)  $\rho_{xx}(0) > 1$ , and (c)  $\rho_{xx}(0) < 1$ .

for three gate voltages corresponding to the lattice resistance per square  $\rho_{xx} < h/e^2$ ,  $\rho_{xx} > h/e^2$ , and  $\rho_{xx} \gg h/e^2$ . The  $\rho_{xx}(B)$  dependences are characterized by three magnetic-field ranges: weak magnetic fields from 0 to 0.05 T, moderate magnetic fields from 0.1 to 0.5 T, and strong magnetic fields  $B > 1$  T. In this section, we analyze only the ranges of moderate and strong magnetic fields. The range of weak fields, where considerable negative magnetoresistance (NMR) is observed, will be examined elsewhere. In moderate fields, so-called commensurate magnetoresistance peaks indicated by arrows in Fig. 2 are observed. Peak 1 corresponds to the condition  $2R_c = d$  ( $R_c$  is the cyclotron radius). It is observed in all lattices of antidots, and is associated with the formation of localized trajectories around one antidot in this case (lattice of close-packed antidots). As is seen, it does not disappear even for  $\rho_{xx} \gg h/e^2$ . The second commensurate peak marked as 2 is observed in the system state with the lowest resistance. This peak corresponds to the condition  $2R_c = (\sqrt{2} - 1)d$ . It is associated with the formation of a localized trajectory between antidots, and was observed in [13]. The trajectories whose formation is responsible for the magnetoresistance peaks under discussion are shown in the insert in Fig. 2. Their positions provide definite conclusion about the relation between  $d$  and  $a$ . In particular,  $d \approx a$  and  $(d - a) \ll a$  for lines in Fig. 2c. Indeed, the ratio of magnetic fields  $B_1$  to  $B_2$  (positions of the first and second peaks, respectively) must be equal to  $B_1/B_2 = \sqrt{2} - 1$  in this case, which is close to  $B_1/B_2 = 0.39$  observed in Fig. 2.

Shubnikov–de Haas oscillations are observed for fields exceeding 1 T. They, as well as peak 1, do not disappear even for  $\rho_{xx} \gg e^2/h$ . The above experimental data indicate that the properties of the system in question are very unusual compared to an unmodulated 2D electron system. As is known, as the latter system changes its state from  $\rho_{xx} < h/e^2$  to  $\rho_{xx} > h/e^2$ , both ballistic effects (manifested as commensurate peaks in the system in hand) and Shubnikov–de Haas oscillations are impossible, because the system undergoes transition to a dielectric state.

**3. Lattice conductance. Dependence on the gate voltage and temperature.** Figure 3a shows the typical gate-voltage-dependence of the lattice conductance  $g$  (measured in  $e^2/h$  units) for temperature  $T = 60 \text{ mK}$ . The solid line is the function  $g = 28.6(V_g - V_g^c)^t$ , where  $V_g$  is the gate voltage,  $V_g^c$  is the cutoff voltage, and  $t = 1.26$ . This dependence is similar to the percolation dependence in the well-known problem of transport in sites of square lattice [14], if the number of sites is proportional to the gate voltage  $r \approx V_g$ . Then,  $g \approx (r - r_c)^t$ , where  $r_c$  is the critical number of sites. The critical exponent  $t$  for this problem is well known and lies in the range  $t = 1 - 1.5$  [14]. Figure 3a demonstrates that exper-

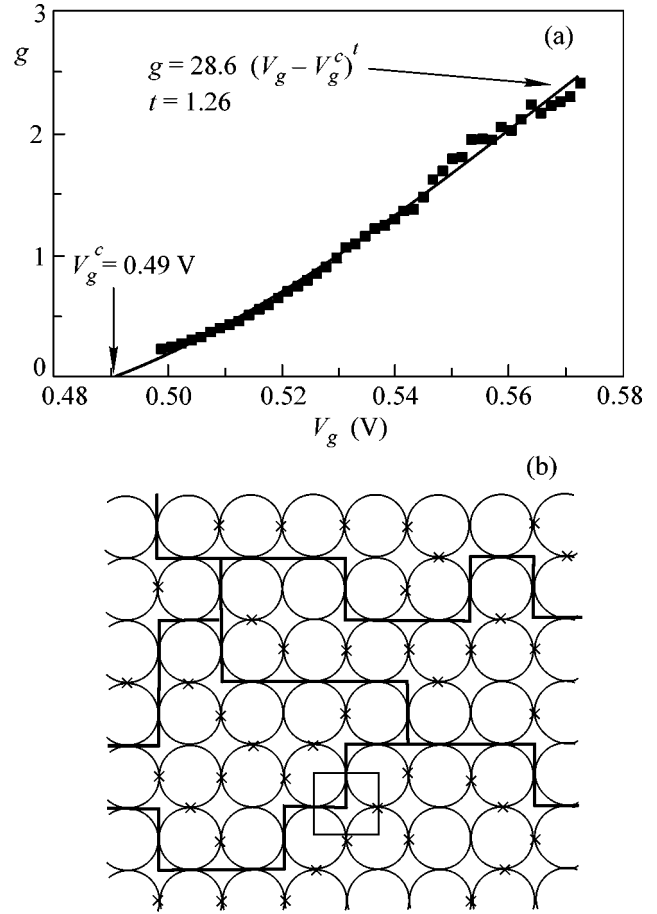
imental data are quite satisfactorily described in the problem of sites, where saddle points connecting individual billiards can serve as sites. The reason is as follows. The fluctuation potential is shielded most efficiently at these points because of a low density of charge carriers. Then, the fluctuations of this potential can strongly affect the passage of an electron by alternately creating a barrier and transmitting one or two electron modes. The above property of saddle points makes it possible to suggest that they may serve as square-lattice sites, whose average number is controlled by the gate voltage, thereby changing the number of transport paths through the lattice. Figure 3b illustrates the above discussion.

Figure 4 shows the temperature dependence of conductance  $g$  for two samples with different mobilities  $\mu =$  (a)  $7 \times 10^5$  and (b)  $3 \times 10^5$   $\text{cm}^2/\text{V s}$  of the original 2D electron gas. The conductances are measured when the system changes  $g > 1$  to  $g \ll 1$ . We first analyze Fig. 4a. Conductance depends only slightly on temperature when  $g > 1$ . At first glance, this behavior is natural, because 2D systems under these conditions usually exhibit a logarithmic decrease in  $g$ , which is attributed to weak localization. Since there is no effect associated with spin relaxation in this system and interaction is weak, the logarithmic correction to conductance is given by the expression [15]

$$\Delta g = -(1/\pi)\ln(T/T_0), \quad (1)$$

which is shown by the dashed line in Fig. 4. As is seen, even logarithmic dependence is noticeably stronger than experimental dependence. Thus, localization effects in the system in question are weaker than those in other 2D and quasi-2D systems. Measurements for  $g < 1$  corroborate the above conclusion. It is seen that, as  $g$  decreases, temperature dependence is enhanced but remains weak even for  $g \ll 1$ . As a whole, all dependences in Fig. 4 are well approximated by the power-law function  $g(T) \sim T^\alpha$  with  $\alpha < 1$ , in particular,  $\alpha = 0.1\text{--}0.27$  and  $0.3\text{--}0.66$  for the original 2D-gas samples with higher and lower mobilities, respectively. Therefore, the enhancement of the initial disorder leads to a sharper drop in conductance with decreasing temperature. The above behavior of 2D lattice of Sinai billiards differs considerably from that observed in all studied 2D electron systems with unmodulated potential beginning with Si MOP transistors [16] and ending with AlGaAs/GaAs heterojunctions [17]. All these systems exhibit different behaviors of conductance (from logarithmic decrease to anomalous increase [18]) for  $g > 1$ . At the same time, they are in the strong localization region characterized by exponential decrease in  $g$  with decreasing temperature below 1 K. Nothing of this kind is observed in the system under investigation: as is seen in Fig. 4, conductance for  $g \ll 1$  decreases with decreasing temperature even more slowly than  $g \sim T$ .

**4. Negative magnetoresistance. Weak localization in chaotic electron trajectories.** Now, we analyze neg-



**Fig. 3.** (a) Gate-voltage dependence of the conductance  $g$  (points) measured for the AG219 sample and (line) calculation, and (b) percolation transport paths in the square lattice.

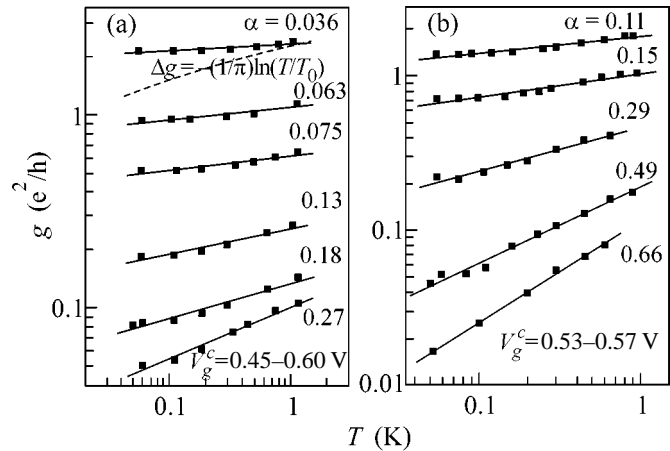


**Fig. 4.** Temperature dependence of  $g$  for samples (a) AG219 with  $d = 0.6$   $\mu\text{m}$  and higher mobility and (b) AG35 with  $d = 0.7$   $\mu\text{m}$  and lower mobility.

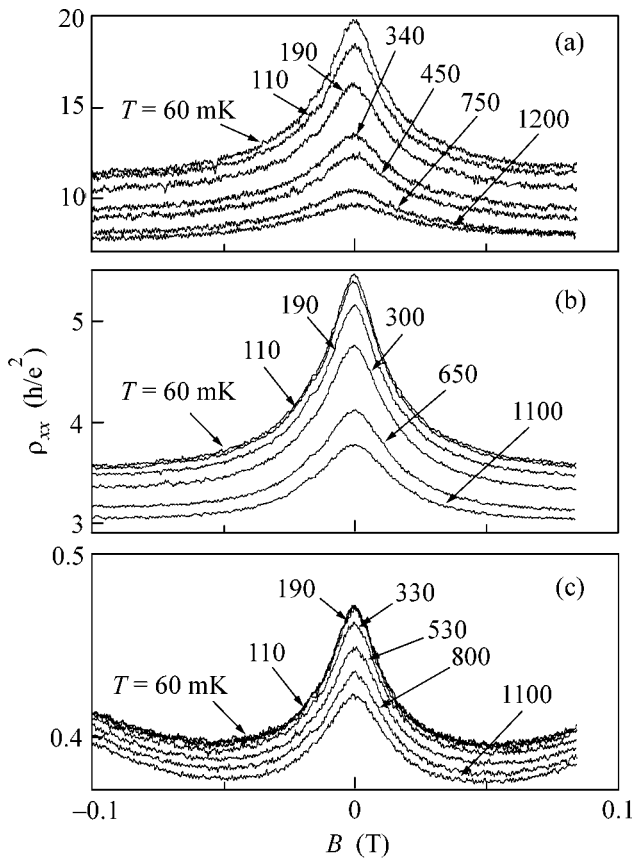


**Fig. 5.** Magnetic-field dependence of the magnetoresistance of the AG219 sample with  $d = 0.6 \mu\text{m}$  for various  $g$  and temperatures.

ative magnetoresistance observed for weak magnetic fields (Fig. 5). The behavior of this negative magnetoresistance for  $g > 1$  can be attributed to the weak localization effects in open electron billiards, which are caused by the interference between chaotic electron trajectories within one billiard. Similar magnetoresistance was observed in [2], where the ensemble of singular billiards of the circus type (a regular billiard) and stadium type (a chaotic billiard) with two open channels was studied. All billiards were separated from each other by a macroscopic 2D electron gas region whose resistance was much lower than the resistance of one billiard. The ensemble was used to average the mesoscopic fluctuations of conductance. According to the theory developed for negative magnetoresistance in a single billiard in [19], negative magnetoresistance for a chaotic billiard (all the Sinai billiards are chaotic) must be described by the expression

$$\Delta\rho_{xx}(B) = -\Delta\rho_{xx}^0/[1 + (B/B_0)^2], \quad (2)$$

where  $B_0 = \Phi_0/2S$  ( $\Phi_0 = hc/e$  is the magnetic flux quantum and  $S$  is the billiard area); i.e., it is given by the Lorentzian whose half-width is determined by the quantization of the flux through the billiard area. Figure 6a

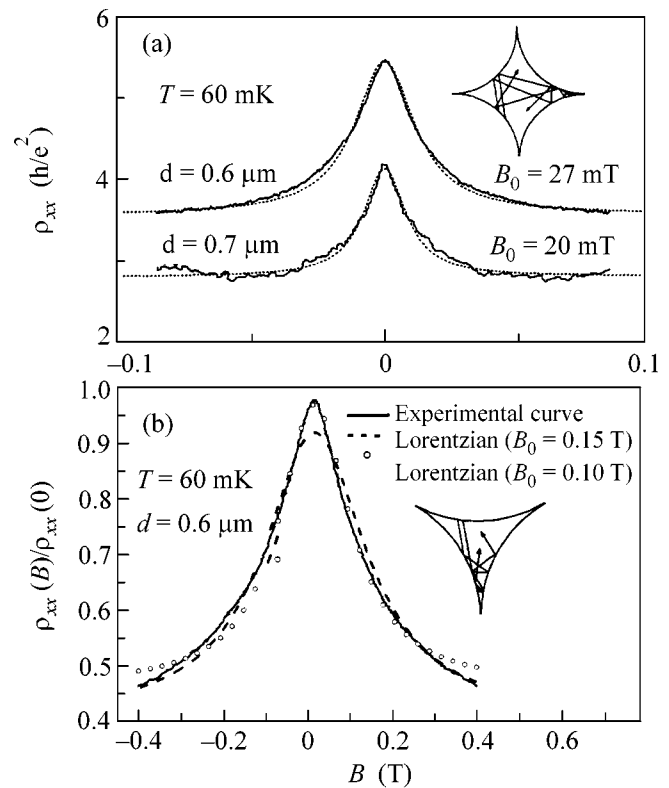


**Fig. 6.** Negative magnetoresistance measured and calculated for (a) square lattices with various periods and (b) hexagonal lattice. The inserts show single billiards forming the square and hexagonal lattices and electron trajectories. The suppression of these trajectories by magnetic field is responsible for negative magnetoresistance.

shows experimental curves  $\Delta\rho_{xx}(B)$  obtained for the square lattices with two periods of 0.6 and 0.7  $\mu\text{m}$ , as well as the results calculated by Eq. (2). It is seen that experimental data are well approximated by Eq. (2), where the area  $S = d^2(1 - \pi/4)$  of a single billiard of our square lattice is substituted. It is of interest that, since a hexagonal lattice corresponds to the maximum close packing, the billiard area for the square lattice is considerably (by a factor of 5.2) larger than for the triangle lattice [for which  $S = d^2(\sqrt{3}/4 - \pi/8)$ ] with the same lattice period. Therefore, the experimental negative magnetoresistance curve shown in Fig. 6b for the hexagonal lattice must be considerably wider than for the square lattice. Figure 6b shows also the fitting curves. It is clearly seen that the half-width of the curve  $\Delta g(B)$  for the triangle lattice considerably exceeds the half-width of the curves in Fig. 6a. We emphasize that Eq. (2) is strictly valid only when  $g > 1$  and  $\Delta g \ll g$ , which are the conditions realized in the experiment carried out in [2]. As is seen in Fig. 6, Eq. (2) in our case well approximates the observed negative magnetoresistance for  $g < 1$  as well. In this case,  $\Delta g$  is comparable to  $\bar{g}$ . Therefore, we arrived at the unexpected results. Mag-

netic-field dependences of negative magnetoresistance are virtually the same for  $g > 1$  and  $g \ll 1$ . However, its magnitude for  $g \ll 1$  is much higher and is comparable with the total conductance for zero magnetic field. Therefore, interference in chaotic trajectories inside a billiard for the lattice of coupled Sinai billiards changes the resistance of the entire system much more considerably than for a single billiard, where the same interference changes the conductance of the system only by several percent [2, 19].

**Discussion. The lattice of coupled electron billiards is a system with suppressed localization.** The above results provide the following conclusions. First, the gate-voltage dependence testifies to a percolation lattice. Second, commensurate magnetoresistance peaks indicate that this lattice has, nevertheless, the properties of a periodic system over the entire range of conductances under investigation, i.e., even for  $g \ll 1$ . These peaks, as well as Shubnikov–de Haas oscillations, corroborate that single billiards forming lattice are coupled through quantum dots in the saddle points of the lattice rather than through tunneling barriers, because the Fermi energy must exceed the barrier height in both cases. Thus, the percolation pattern of charge transport is as follows. For high conductance ( $g > 1$ ), all sites, which are saddle points, are open, and the conductance of the lattice is approximately equal to the conductance of one site  $g_{sp} = 2ne^2/h$ , where  $n$  is the number of modes passing through it. As the gate voltage decreases, the number of open sites decreases, and transport occurs only through individual quasi-one-dimensional percolation paths, which is manifested in the dependence  $g \sim (r - r_c)^t$ . The results presented in Section 3 indicate that the temperature dependence of this conductance is very weak even for  $g \ll 1$ , in contrast to the ordinary 2D systems. The weakness of this dependence cannot be explained by the percolation transport, because the formation of quasi-one-dimensional paths must enhance the localization effects and, therefore, temperature dependence. As far as I know, the linear, rather than exponential, temperature dependence for  $g \ll 1$  was observed only in the experiment reported in [20], where thin  $\text{In}_2\text{O}_3$  films were examined. This system was analyzed theoretically by Imry *et al.* [21], who proposed a model implying that metallic granules with high conductance,  $g \gg 1$ , are coupled with each other through tunneling barriers so that the conductance of a macroscopic system of granules is low,  $g \ll 1$ . The conductance of this system was shown to depend linearly on temperature over a wide temperature range due to inelastic electron–electron scattering. However, this linear dependence must go over to the exponential dependence for  $T \ll e^2/C$  ( $C$  is the capacity of a granule). Our results are inconsistent with the prediction made in [21]. First, our experiment reveals temperature dependence noticeably weaker than linear. Second, estimates indicate that the Coulomb energy is equal to  $e^2/C \approx 15\text{--}25$  K in our case, and,

thereby, exponential temperature dependence must be observed in the temperature range 0.05–1 K under investigation. It is easy to understand this inconsistency, because billiards of our system are separated by quantum dots rather than by tunneling barriers. For this reason, the model proposed in [21] does not explain the temperature dependence of conductance obtained in our experiment and must be developed for the case, where billiards are connected by ballistic rather than tunneling electrons, the more so as the behavior of the system in magnetic field is also anomalous. As is seen in Fig. 2, for magnetic fields exceeding the field corresponding to the commensurate peak, conductance is temperature-independent, remaining much higher than  $h/e^2$ . As is well known [17], an ordinary 2D system under these conditions undergoes the insulator–Hall liquid–insulator transition. To explain all these anomalies, it is necessary to develop a consistent theory of quantum transport in a 2D lattice of coupled Sinai billiards, which is a difficult problem. Below, only a qualitative concept, rather than consistent quantitative description of all observed effects, will be presented.

The localization length  $\xi$  in a homogeneous 2D system is approximately estimated by the expression [15]

$$\xi \approx l_p \exp(\pi/2) k_F l_p, \quad (3)$$

which discriminates weak,  $k_F l_p \gg 1$ , and strong,  $k_F l_p \approx 1$ , localization regimes. Since  $g = k_F l_p$  in the 2D case, conductance is that measurable characteristic of the system which indicates the transition from one mode to another. It follows from Eq. (3) that  $\xi \approx 1/k_F$  in the strong localization mode. In this case, the characteristic energy corresponding to the transition to the exponential temperature dependence for  $g \leq 1$  is equal to  $E_c \approx \hbar^2 k_F^2 / m^* \approx E_F = 15\text{--}30$  K. It is reasonable to assume that  $\xi \approx L$ , where  $L$  is the characteristic size of a billiard. Therefore, the characteristic energy is easily estimated as  $E_c \approx E_F/N$ , where  $N$  is the number of electrons in the billiard and is easily determined in terms of the known area of the billiard. For the square lattice with period  $d = 0.6$  and  $0.7$   $\mu\text{m}$ ,  $N = 80\text{--}120$  and  $110\text{--}160$ , respectively. Therefore, the exponential temperature dependence of  $g$  for the system in question must begin with temperatures  $T < 0.1$  K; i.e., the characteristic temperature must strongly decrease. This circumstance can explain, at least qualitatively, the absence of exponential localization in the system under investigation and is corroborated by the results obtained in [22], where short-period lattices ( $d = 0.2$  and  $0.3$   $\mu\text{m}$ ) were examined. The above argumentation is applicable if the phase-coherence time  $\tau_\phi$  exceeds the electron lifetime in the billiard  $\tau_{\text{esc}}$ . All the available experimental and theoretical estimates give  $\tau_\phi = 10^{-10}\text{--}10^{-9}$  s for single billiards at  $T < 1$  K [23]. Formula  $\tau_{\text{esc}} \approx (S/W)v_F$  [24] ( $W$  is the width of the neck and  $v_F$  is the Fermi velocity) yields  $\tau_{\text{esc}} \approx 10^{-11}$  s; i.e., the above condition is satisfied.

Thus, the conductance of the lattice of coupled electron billiards is not described by the standard 2D localization, and  $g$  is not a qualitative characteristic of the system, in contrast to homogeneous 2D electron systems. The localization length and conductance of such a system is determined by the lattice period and classical percolation transport, respectively. Owing to both indicated features, the 2D lattice of Sinai billiards coupled through quantum dots can exhibit metallic and ballistic (commensurate magnetoresistance peaks and weak localization in chaotic trajectories, as well as Shubnikov–de Haas oscillations) properties even for  $g \ll 1$ . Their full description is an interesting problem for the theory of quantum interference effects in systems, where the disorder effect, along with the interference of chaotic electron trajectories, must be taken into account. In particular, only this theory will be capable of explaining extremely high negative magnetoresistance in the lattice. The results clearly demonstrate that conductance, even being macroscopically homogeneous, cannot be a universal characteristic of any 2D electron system. For this reason, scaling argumentation must be carefully applied to localization in actual 2D electron systems, where regions with a large number of electrons can be formed with high probability.

I am grateful to M.V. Budantsev and A.G. Pogosov for common work and V.I. Fal'ko for stimulating discussion. This work was supported by the Russian Foundation for Basic Research, project no. 99-02-16756.

#### REFERENCES

1. C. M. Marcus, A. J. Rimberg, R. M. Westervelt, *et al.*, Phys. Rev. Lett. **69**, 506 (1992).
2. A. M. Chang, H. U. Baranger, L. N. Pfeifer, and K. W. West, Phys. Rev. Lett. **73**, 2111 (1994).
3. A. M. Chang, H. U. Baranger, L. N. Pfeifer, *et al.*, Phys. Rev. Lett. **76**, 1695 (1996).
4. J. A. Folk, S. R. Patel, S. F. Godjin, *et al.*, Phys. Rev. Lett. **76**, 1699 (1996).
5. R. P. Taylor, R. Newbury, A. S. Sachrajda, *et al.*, Phys. Rev. Lett. **78**, 1952 (1997).
6. K. Ensslin and P. M. Petroff, Phys. Rev. B **41**, 12307 (1990).
7. D. Weiss, M. L. Roukes, A. Mesching, *et al.*, Phys. Rev. Lett. **66**, 2790 (1991).
8. G. M. Gusev, V. T. Dolgoplov, Z. D. Kvon, *et al.*, Pis'ma Zh. Éksp. Teor. Fiz. **54**, 369 (1991) [JETP Lett. **54**, 364 (1991)].
9. A. Lorke, J. P. Kotthaus, and K. Ploog, Phys. Rev. B **44**, 3447 (1991).
10. E. M. Baskin, G. M. Gusev, Z. D. Kvon, *et al.*, Pis'ma Zh. Éksp. Teor. Fiz. **55**, 649 (1992) [JETP Lett. **55**, 678 (1992)].
11. M. V. Budantsev, Z. D. Kvon, A. G. Pogosov, *et al.*, Surf. Sci. **361/362**, 739 (1996).
12. M. V. Budantsev, Z. D. Kvon, A. G. Pogosov, *et al.*, Pis'ma Zh. Éksp. Teor. Fiz. **59**, 614 (1994) [JETP Lett. **59**, 645 (1994)].
13. M. V. Budantsev, Z. D. Kvon, A. G. Pogosov, *et al.*, Physica B (Amsterdam) **260**, 363 (1998); M. V. Budantsev, Z. D. Kvon, A. G. Pogosov, and J. C. Portal, Usp. Fiz. Nauk, Suppl. **171**, 20 (2001).
14. B. I. Shklovskii and A. L. Efros, *Electronic Properties of Doped Semiconductors* (Nauka, Moscow, 1979; Springer-Verlag, New York, 1984).
15. P. A. Lee and T. V. Ramakrishnan, Rev. Mod. Phys. **57**, 287 (1985).
16. T. Ando, A. Fowler, and F. Stern, Rev. Mod. Phys. **54**, 437 (1982).
17. H. W. Jiang, C. E. Jonson, K. L. Wang, and S. T. Hannas, Phys. Rev. Lett. **71**, 1439 (1993); T. Wang, K. P. Clark, G. F. Spencer, *et al.*, Phys. Rev. Lett. **72**, 709 (1994); R. J. F. Hughes, J. T. Nicholls, J. E. F. Frost, *et al.*, J. Phys.: Condens. Matter **6**, 4763 (1994); D. Shahar, D. Tsui, and J. E. Cunningham, Phys. Rev. B **52**, R14372 (1995).
18. E. Abrahams, S. Kravchenko, and M. P. Sarachik, Rev. Mod. Phys. **73**, 251 (2001).
19. H. U. Baranger, R. A. Jalabert, and A. D. Stone, Phys. Rev. Lett. **70**, 3876 (1993).
20. Z. Ovadyahu and Y. Imry, J. Phys. C **18**, L19 (1985).
21. Y. Imry, A. Stern, and U. Sivan, Europhys. Lett. **39**, 6239 (1997).
22. G. Lutjering, D. Weiss, R. Tank, *et al.*, Surf. Sci. **361/362**, 925 (1996); F. Nihey, M. Kastner, and K. Nakamura, Phys. Rev. B **55**, 4085 (1997).
23. J. Bird, J. Phys: Condens. Matter **11**, R413 (1999).
24. I. L. Aleiner and A. I. Larkin, Phys. Rev. B **54**, 14423 (1996).

*Translated by R. Tyapaev*